Conceptual design of windplanes

Filippo Trevisi

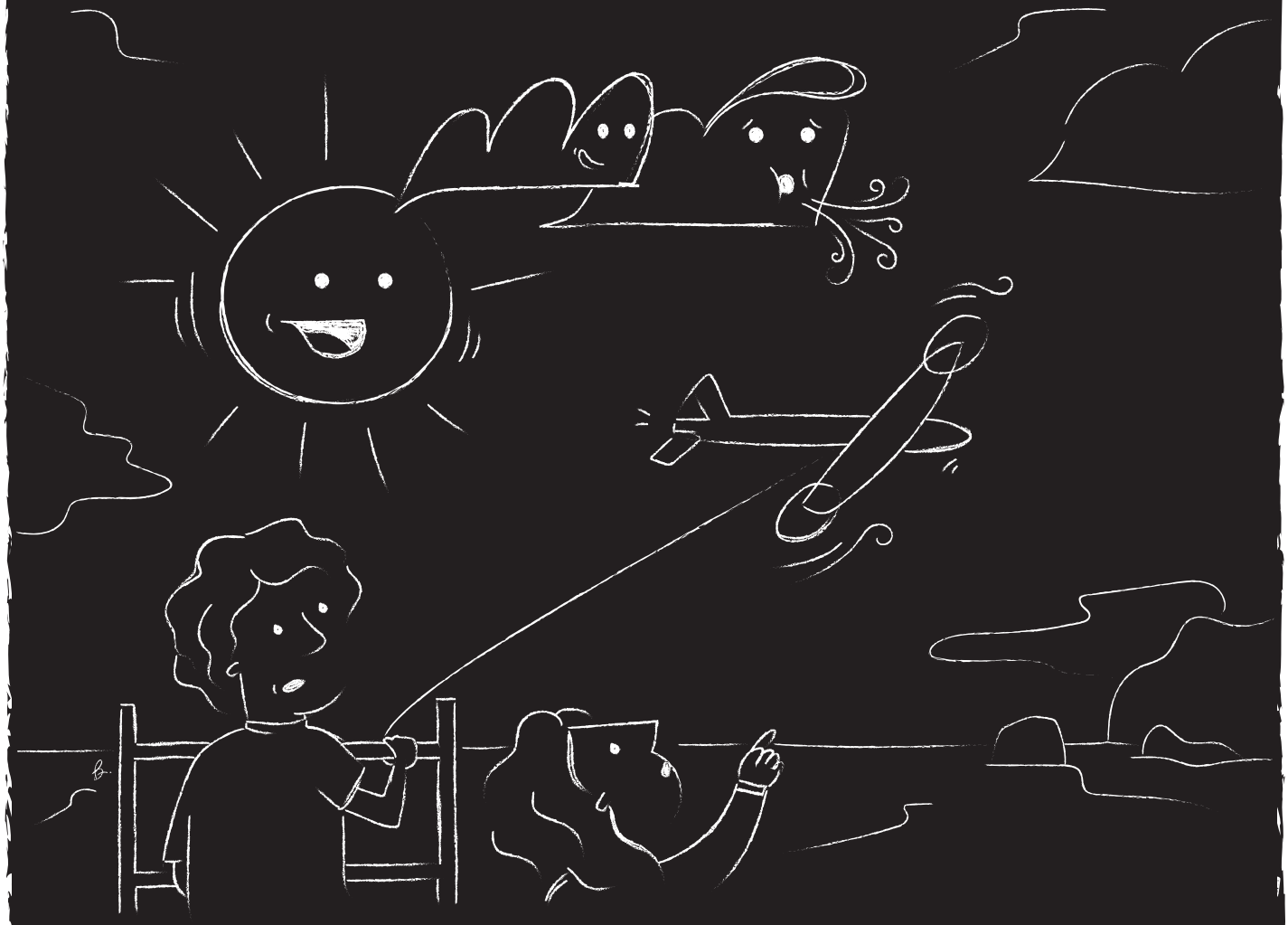

GIVEN A WINGSPAN, WHICH DESIGN MAXIMIZES POWER?

CAN WINDPLANES FLY STABLE ORBITS?

POLITECNICO
MILANO 1863

POLITECNICO DI MILANO
DEPARTMENT OF AEROSPACE SCIENCE AND TECHNOLOGY
DOCTORAL PROGRAMME IN AEROSPACE ENGINEERING

CONCEPTUAL DESIGN OF WINDPLANES

Doctoral Dissertation of:
Filippo Trevisi

Supervisors:
Prof. Alessandro Croce
Prof. Carlo E. D. Riboldi

February 2024 – XXXVI cycle

When you face a new problem,
study the fundamental physics and solve it by yourself.
After you got to your solution, look at the literature.
If you find the same, then you deeply understood the problem.
If you don't find it, then you made a discovery.

Mac

Prefazione e ringraziamenti

"Sennò potremmo buttarci sui kite". Ero perplesso, ma Mike continuò: "Potrebbe sembrarti strano, ma si può generare energia dal vento anche con degli aquiloni" e mi spiegò i concetti principali. Effettivamente sembrava una follia. Aggiunse: "Dovremmo parlarne con Mac". Michael McWilliam e Mac Gaunaa mi hanno trasmesso la cosa più importante di tutte, per la quale sarò per sempre grato: cosa significa essere un ricercatore.

Era l'inizio del 2019. Mi diedero "Crosswind Kite Power", il paper di Loyd (1980) che aveva gettato le basi del settore che ora chiamiamo "Airborne Wind Energy". Così iniziò il mio viaggio. Che visione grandiosa: energia eolica volante. Mi misi rapidamente al passo con il settore, studiando lo stato dell'arte e le aziende già attive. La mia tesi di laurea magistrale fu l'antipasto della tesi che state leggendo, con modelli semplificati, ottimizzazione e analisi di sensitività. Roland Schmehl fu il mio esaminatore e negli anni successivi diventò il mio editore, il mio revisore, il mio supervisor e infine un mio collega. Grazie Roland per essere un pilastro per Airborne Wind Energy.

Vivevo a Copenaghen e il mio coinquilino era Fabio Spagnolo, che aveva il mio stesso background accademico. Amavamo perderci in deliri a proposito dei nostri studi e, chiacchierando, concordammo sull'importanza di modellare i kite come un sistema lineare per studiarne la stabilità. Ma rispetto a che condizione di volo? Non lo sapevamo.

In quell'autunno andai con Mac alla conferenza sull'Airborne Wind Energy a Glasgow, scoprendo ed immergendomi in una comunità di sognatori. Makani, l'azienda finanziata da Google sui kite, mostrò i risultati dei loro test in mare su piattaforma galleggiante: da non crederci. Poi, Lorenzo Fagiano tenne una plenaria che mi impressionò e andai a incontrarlo e conoscerlo.

Dopo la tesi, iniziai a lavorare come assistente di ricerca al DTU di Copenaghen, imparando l'arte del progettare turbine eoliche dai padri stessi dell'energia del vento. Con Mac e Mike cercavamo finanziamenti per la ricerca sui kite senza trovarli e, parallelamente, ci preparavamo per la conferenza TORQUE. Io iniziai a studiare la fisica del cavo con una formulazione matematica inutilmente complessa e trovai una sorpresa. Trascurando la gravità, il problema diventa assialsimmetrico ed esiste una traiettoria circolare che massimizza la potenza. Se le forze centrifughe sono bilanciate

dalla componente radiale della forza del cavo, allora la portanza viene utilizzata solo per la generazione di energia. Detta in breve: $\sin\Phi\tan\Phi = M$. Boom. Avevo trovato l'orbita che stavo cercando per studiare la stabilità del volo. Nel frattempo, Mac mise ordine nel problema aerodinamico dei kite con un semplice messaggio: la teoria del momento non funzionava, bisognava usare la teoria dei vortici.

All'improvviso, intanto, Makani chiuse. "Google non ce l'ha fatta, starai coi piedi per terra ora?" mi dicevano. Perchè si erano fermati? Avevano trovato problemi ingegneristici o fisici? Queste domande furono uno stimolo in più per me. Il finanziamento per il mio dottorato sui kite non arrivava, così mi ricordai di Lorenzo e gli mandai un messaggio. Mi consigliò di candidarmi al Dipartimento di Aerospaziale a Milano e di parlare con Alessandro Croce e Carlo Riboldi, esperti in meccanica del volo e energia eolica. In Italia, c'erano alcune borse di dottorato generiche e avrei potuto proporre al dipartimento il mio progetto di ricerca. Lo feci e ottenni la posizione. Mi misi $\sin\Phi\tan\Phi = M$ in tasca e tornai in Italia.

Fin dal primo giorno di dottorato, il mio studio si concentrò sulla stabilità del volo in quella traiettoria circolare. Volevo capirla a fondo. Derivai tutto in modo analitico in 40 pagine di matematica pesante - poveri revisori. Il cavo à attaccato un po' più a poppa rispetto al centro di massa, il timone spinge verso l'esterno ed eccoci qua: stabilità! Era un ottimo punto di partenza. Ma quanto era teorico? Quanto era lontano dalla realtà? E se avessi reintrodotto la gravità?

Nell'autunno 2021 Gregorio Pasquinelli iniziò la sua tesi di laurea con noi. Sviluppò un modello dinamico semplificato dei kite che volano in traiettorie circolari, perfetto per comprendere l'effetto della gravità sulla potenza. In quel momento ero a Delft, per il mio periodo all'estero, e condividevo l'ufficio con Iván Castro, che veniva dalla UC3M di Madrid. Gregorio provò la presentazione della tesi con noi ed Iván, ascoltandolo, ebbe un'intuizione: "Perchè non usi il metodo del bilanciamento delle armoniche per integrare la dinamica?". Ci accese: un'idea semplice ed elegante, come tutte le migliori. Partendo da quello spunto, migliorammo il modello e guardammo le armoniche della traiettoria. Lo scambio di energia potenziale gravitazionale lungo la traiettoria, funzione della massa e del raggio di curvatura, riduce la potenza. Per questo effetto, sono preferibili i kite che riducono il raggio di curvatura. Tuttavia per un raggio di curvatura più piccolo, l'area spazzata è inferiore e quindi meno energia eolica è disponibile. Come modellare la diminuzione dell'energia del vento dovuta al minor raggio di curvatura? Mac lo aveva indicato: teoria dei vortici.

Con la testa che frullava con queste nuove idee, prima andai alla conferenza TORQUE a Delft e poi ospitammo la Conferenza sull'Airborne Wind Energy a Milano nell'estate 2022. Grazie a Lorenzo Fagiano e Alessandro Croce per aver organizzato un evento del genere. Mamma mia, quanto sono felice della nostra comunità eolica! Anime affamate che scambiano idee con un obiettivo comune: capire come meglio raccogliere energia eolica dalla natura.

Il problema aerodinamico dei ventoplani, ho iniziato a chiamarli così, è estremamente affascinante, avendo caratteristiche sia degli aeroplani che delle turbine eoliche. Ho ideato un modello semplificato per capire quanto il vento sia rallentato dal ventoplano stesso. Se il raggio di curvatura è più piccolo, allora il vento viene fermato di più. Ho incluso questo effetto nelle equazioni di potenza e ho definito un nuovo coefficiente di potenza. Questo coefficiente mostra quanta potenza il ventoplano raccoglie per una

data apertura alare. Allo stesso modo, il coefficiente di potenza per le turbine eoliche mostra quanta potenza la turbina raccoglie per una data apertura delle pale. Questo ha aperto una comprensione completamente nuova: l'allungamento alare ottimale è finito, i profili aerodinamici ottimali massimizzano l'efficienza e la massa ottimale è anch'essa finita.

Gli ultimi mesi li ho trascorsi a dare una cornice a tutte queste idee. Sono stati estremamente intensi, ma anche estremamente luminosi. Ho una profonda sensazione di soddisfazione per questo incredibile viaggio. E ora voglio volare più lontano: sento che questo è solo l'inizio.

Ringrazio profondamente il mio supervisor Alessandro Croce per aver intrapreso questa emozionante sfida con me. Grazie al gruppo Poli-Wind, Carlo Riboldi, Stefano Cacciola, Mariana Montenegro e Kutay Yilmazlar per il grande sostegno. Kutay, meriti un dottorato in floating wind con menzione su airborne wind. Grazie alle persone che hanno condiviso con me idee e visioni al Dipartimento di Scienze e Tecnologie Aerospaziali e al Politecnico di Milano. Grazie ai miei studenti per il loro contributo a questa tesi e ai futuri lavori. Grazie a tutti i miei amici nella comunità dell'energia eolica a Copenhagen, Delft, Monaco e in tutto il nostro pianeta. Grazie a Rishikesh Joshi per aver intrapreso lo sviluppo del modello economico con me, uno sforzo cruciale per il settore. Grazie ad Airborne Wind Europe per promuovere airborne wind energy con questo entusiasmo.

Grazie a tutti gli amici che mi hanno sostenuto in questi cinque anni. Grazie a Ilaria Barcella per questa copertina così pura. Grazie agli miei amici di una vita per esserci: la mia crescita professionale non ci sarebbe senza la mia crescita personale. Grazie alla mia famiglia per avermi insegnato a seguire i miei sogni, anche quando volano.

A Sahel e Océane
Per le generazione future

Preface and acknowledgments

"Otherwise, we could look into kites". I was puzzled, Mike continued: "It might sound crazy, but you can harvest wind power with kites" and he explained the main concepts. It was definitely crazy. He added: "We should talk with Mac". Michael McWilliam and Mac Gaunaa showed me the most important thing, for which I will always be grateful: what being a researcher means.

It was the starting of 2019. They gave me "Crosswind Kite Power", the paper by Loyd (1980) which kicked off the sector that we now call "Airborne Wind Energy" and my journey started. What a great vision! Wind energy going airborne! I quickly got to speed with the field, studying the state-of-the-art and looking at the companies. My master thesis was the teaser of my Ph.D. thesis, with simplified models, optimization and sensitivity analyses. Roland Schmehl was my examiner, and in the following years has been my editor, reviewer, supervisor, colleague. Thank you Roland for being a pillar for Airborne Wind Energy.

I was living in Copenhagen and my flatmate was Fabio Spagnolo, with my same academic background. In one of our endless conversations about our studies, we agreed on the importance of modeling the kite as a linear system to study its stability. But, about which reference flight condition? We did not know.

That autumn, I attended with Mac the Airborne Wind Energy Conference in Glasgow, finding a community of dreamers. Makani, the company funded by Google, showed the results of their astonishing test floating offshore. Lorenzo Fagiano gave an impressive plenary talk, and I went to meet him.

After the thesis, I started working as a research assistant at DTU in Copenhagen, learning the art of designing wind turbines from the fathers of wind energy. How much I learned that year! With Mac and Mike, we were -unsuccessfully - looking for funding to research on airborne wind and, as side projects, we did some studies for the TORQUE conference. I started looking into the tether physics with an unnecessarily complicated mathematical formulation and I found a surprise. By neglecting gravity, the problem becomes axial symmetric and there exists one circular trajectory that maximizes power. If centrifugal forces are balanced by the radial component of the tether force, then lift is only used for power generation! Simply: $\sin\Phi\tan\Phi = M$. Wow! I found the orbit I was looking for to study the flight stability! In the meantime, Mac made order in

the aerodynamic problem of kites with a simple message: momentum theory does not work here, we should use vortex theory.

Suddenly, Makani was shut down. "Google did not make it, will you stay on the ground now?" Why did they stop? That was an extra motivation for my research. The funding for my PhD on airborne wind was still not coming, so I remembered about Lorenzo and texted him. He told me to apply to the Aerospace Department and to talk with Alessandro Croce and Carlo Riboldi, experts in flight dynamics and wind energy. In Italy, there are some general PhD scholarships and I could apply with my own PhD project. I got the position, I took $\sin\Phi\tan\Phi = M$ in my pocket and I moved back to Italy.

From the very first day of the PhD, I looked at the flight stability about that circular trajectory. I wanted to understand it deeply and I derived everything analytically in 40 pages of heavy math, poor reviewers. The tether is attached a bit aft than the center of mass, the vertical tail pushes outward and there you are! Stable designs! That was a great starting point. But how far is this from reality? What if we put gravity back?

In the fall 2021, Gregorio Pasquinelli started his master's thesis with us. He developed a simplified dynamical model of the kite flying circular trajectories, perfect for the understanding of the effect of gravity on power. At the time of his thesis defense, I was in Delft, doing my external stay, and I shared the office with Iván Castro, doing his external stay from UC3M Madrid. Gregorio rehearsed the thesis presentation with us. "Why don't you use the harmonic balance method to integrate the dynamics?" and Iván introduced the method to us. Oh, what a simple and elegant idea! We improved the model and looked at the harmonics of the trajectory. The exchange of gravitational potential energy over the loop, function of mass and turning radius, reduces the power output. For this effect, the designs reducing the turning radius are preferable. Wait.. For a smaller turning radius, the swept area is lower, and then less wind power is available. How to model the decrease in available wind power due to the smaller turning radius? Mac pointed it out: vortex methods.

With these thoughts in mind, I went to the TORQUE Conference in Delft and we hosted the Airborne Wind Energy Conference in Milan in the summer 2022. Thanks to Lorenzo Fagiano and Alessandro Croce for organizing such an event. Oh, how much I enjoy our (airborne) wind community! Many friends sharing ideas with a unique goal: to understand how to better collect wind energy from nature to power our civilization sustainably.

The aerodynamic problem of windplanes, I started calling them in this way, is extremely fascinating, having features of both airplanes and wind turbines. I came out with a simplified model to find how much the wind is slowed down by the windplane. If the turning radius is smaller, then the wind is stopped more! I then included this effect in the power equations, and I defined a novel power coefficient. This coefficient shows how much power the windplane harvests per wing span. Similarly, the power coefficient for conventional turbines shows how much power the wind turbine harvests per blade span. This opened up a completely new understanding: the optimal aspect ratio is finite, the optimal airfoils are maximizing the C_L/C_D and the optimal mass is also finite.

The last few months spent on giving a framework to all these thoughts have been extremely intense, but also extremely bright. I have a deep feeling of satisfaction for this

journey, shaken by the willingness to fly further: I know that this is just the beginning.

I deeply acknowledge my supervisor Alessandro Croce for undertaking this challenge with me. Thanks to the Poli-Wind group Carlo Riboldi, Stefano Cacciola, Mariana Montenegro, and Kutay Yilmazlar for all the support. Kutay, you deserve a Ph.D. in floating wind with a mention on airborne wind. Thanks to the people who shared with me ideas and visions in the Department of Aerospace Science and Technology and in the Politecnico di Milano. Thanks to my students for their contributions to this thesis and to future works. Thanks to all my good friends in the wind energy community in Copenhagen, Delft, Munich, and all around our planet. Thanks to Rishikesh Joshi for undertaking the development of the reference economic model with me, a crucial effort for the field. Thanks to Airborne Wind Europe for doing such a great job in promoting the development and deployment of airborne wind energy.

Thanks to all the friends who supported me in these five years. Thanks to Ilaria Barcella for this neat cover. Thanks to my lifelong friends for traveling with me: my professional growth would not be there without my personal growth. Thanks to my family for teaching me to follow my dreams, even when they fly.

To Sahel and Océane
For future generations

Abstract

Windplanes can be understood as an evolution of conventional wind turbines. In this thesis, the conceptual design of windplanes is investigated by addressing two main research questions.

The first research question is "Given a wingspan, which design maximizes power?". The windplane is idealized as a point mass flying circular trajectories. If gravity is removed from the model, the dynamic problem is axial symmetric and the solution is steady. The generated power can be expressed in non-dimensional form by normalizing it with the wind power passing through a disk with radius the wingspan. Since the reference area is taken to be a function of just the wingspan, looking for the design which maximizes this power coefficient addresses the first main research question. The optimal designs have a finite aspect ratio and operate at the maximum lift-to-drag ratio of the airfoil. Airfoils maximizing the lift-to-drag ratio are then optimal for windplanes. If gravity is included in the model, the gravitational potential energy is being exchanged with the kinetic energy, the aerodynamic energy and the electric energy over one revolution. Since this exchange comes with an associated efficiency, the plane mass and the related trajectory are designed to reduce the potential energy fluctuating over the loop. Reducing the potential energy means reducing the turning radius and the mass. However, for decreasing turning radii, the available wind power decreases because the windplane sweeps a lower area. For these two conflicting reasons, the optimal mass is finite. Depending on the independent variables, extremely light designs might then not be required. High power coefficients can be obtained even at low wind speeds.

The second research question is "Can windplanes fly stable orbits?". The windplane is modeled as a rigid-body with an aerodynamic model analytically linearized about non-linear operating points and subject to gravity. The nonlinear equations of motion are solved with a harmonic balance method to look for periodic solutions. If the gravity is removed from the model, the problem has a steady solution. The windplane is trimmed in the circular crosswind trajectory which maximizes the swept area. The vertical stabilizer pushes outwards, to compensate for the yaw moment induced by the centrifugal force. If the gravity is included in the model, the simplest control strategy is to trim the horizontal stabilizer, the vertical stabilizer and the turbine thrust coefficient to constant values, to actuate the ailerons cyclically and to control the vertical stabi-

lizer in closed loop. The cyclic control of the ailerons rolls the plane and redirects the lift to compensate gravity and to stay airborne. The vertical stabilizer is controlled in closed loop to increase directional stability and damp the precession mode. A moderate reduction in power coefficient between the steady case and the dynamic case with this simple control is found at low wind speed. A complete stability analysis is carried out, showing that the pendulum mode is lightly damped and the precession mode needs feed-back control.

The development of a reference economic model for airborne wind energy has been initiated and will be concluded in the near future.

Keywords: windplanes; airborne wind energy; conceptual design; optimization; flight stability

Contents

CHAPTER 1

Introduction

"The era of global boiling has arrived" A. Guterres, UN secretary general, July 2023. We, humans, must stop warming up our planet. To keep warming the climate is unbearable for the planet Earth, which is kindly hosting us, and for the future generations of humans, which will not have time left to act. Renewables are playing a fundamental role in decarbonizing the human civilization and any candidate innovation in this sector must be tried out as soon as possible. The role of academia is to explore these innovations and to educate students to drive the "global boiling era" into the "green era".

Renewable energy should generate the 68 % of the total generated energy by 2030 to meet the 1.5 °C target, from the share of 28 % of 2021. Of this generated power, approximately one third should come from wind energy (IRENA and GRA (2023)). Conventional wind energy is quickly ramping up the production. However, the technology can reach the installation targets for 2030 only with public support and after some of the research grand challenges are solved (Veers et al. (2022)). Will conventional wind energy alone satisfy the need for wind power in the following decades? A report from the International Energy Agency (IEA (2021)) shows that almost half of the reduction in carbon emission in 2050 should come from technologies that are currently at the demonstration or prototype phase.

Which role will airborne wind energy play in the innovation-hungry green era?

1.1 Airborne wind energy

Airborne Wind Energy (AWE) refers to the field of wind energy in which tethered airborne systems are used to harvest wind power at high altitudes. Airborne Wind Energy Systems (AWESs) are typically classified based on their flight operations, which can

be crosswind or tether-aligned. Crosswind AWESs make use of wings flying perpendicular to the wind direction. Electric power is generated with onboard wind turbines and transferred to the ground through the tether (Fly-Gen), generated on the ground by a pulling the tether and unwinding a generator (Ground-Gen) or generated on the ground by converting the torque transmitted by a network of wings (Rotational). The main change between the three different concepts in the crosswind family is how electric power is produced, while the aerodynamic problem is similar. A further distinction is on the wings mass. The dynamics of extremely light wings, such as soft kites or biplanes, might be really different from that of heavier rigid wings.

To investigate the crosswind physics, the simplest concept to be modeled should be considered first. In my opinion, the simplest concept from a modeling point of view is a rigid wing Fly-Gen. Ground-Gen systems operate in cycles of reel-out and reel-in, where the two phases have really different operating points. Rotational systems have many wings and many tethers. Fly-Gen systems instead operate continuously in production phase and are characterized by one main wing and one tether. Moreover, if the gravity is neglected and the mass is large enough, Fly-Gen systems fly circular steady trajectories. This is an interesting starting point for investigating the crosswind physics. This thesis focuses then on crosswind Fly-Gen AWESs, and we we will refer to them as *windplanes*, or shortly *planes*.

Loyd (1980) first derived the power equations of crosswind AWES and his paper is commonly considered as the starting of AWE. The scientific research took almost 30 years to ramp up, with most of the research studies carried out after 2010. Among the many scientific contributions in a variety of journals, the two Springer books - collections of articles- (Ahrens et al. (2013); Schmehl (2018)) and the MDPI special issue (Hackl and Schmehl (2023)) show well the progresses in the field over the last decade. For a better overview of the different concepts and players, please follow the industry association Airborne Wind Europe (2023b), which is doing a great job in promoting Airborne Wind Energy in the world. They are managing the IEA Wind TPC Task 48 on Airborne Wind Energy (Airborne Wind Europe (2023a)), which started in 2021 and creates strong community that works together to develop airborne wind energy. Moreover, they co-organize the bi-annual Airborne Wind Energy Conferences. The previous edition was held in Milan, Italy and the next will be in Madrid, Spain in April 2024.

1.2 From conventional wind turbines to windplanes

Windplanes can be understood as an evolution of conventional wind turbines. Referring to Fig. 1.1, we go through the conceptual steps that bring from a conventional upwind turbine (a) to a windplane (e) to identify some characteristics helpful for the physical understanding of the technology.

(a) **Wind turbine**
Some conceptual characteristics of conventional horizontal axis wind turbines are

1 The aerodynamic thrust slows down the wind by producing a distributed aerodynamic induction over the rotor disk.

2 The aerodynamic thrust generates flapwise bending moments at the blade root, transmitted to the nacelle.

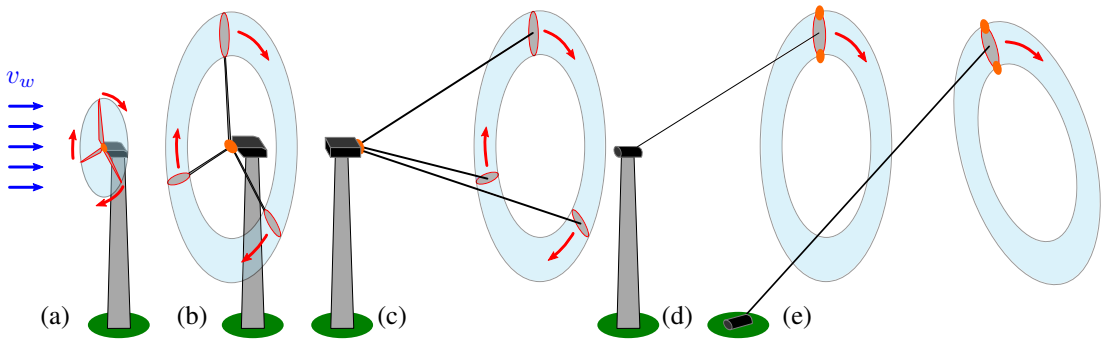

Figure 1.1: *Evolution from a conventional wind turbine to a windplane. (a) Conventional horizontal axis turbine; (b) wind turbine with lifting bodies moved outwards; (c) wind turbine with lifting bodies moved outwards and load alignment; (d) windplane mounted on a tower; (e) windplane.*

3 The aerodynamic torque, generated by the tangential aerodynamic component of lift and drag at each blade section, is equal to the generator torque, necessary to produce electric power.

4 The aerodynamic torque is transmitted to the generator via edgewise bending moments.

5 The rotor center of mass does not move.

6 The aerodynamic thrust generates bending moments at the tower root, discharged at the ground.

(b) **Wind turbine with lifting bodies moved outwards**
The lifting bodies (blades) are moved outwards so that the aerodynamic power is just produced over an annulus. A supporting structure to transmit flapwise and edgewise bending moments is still needed.

Point (a).1 is modified to

1 The aerodynamic thrust slows down the wind by producing a concentrated aerodynamic induction over an annulus.

(c) **Wind turbine with lifting bodies moved outwards and load alignment**
The lifting bodies are moved downwind such that the sum of centrifugal forces, acting radially, and aerodynamic thrust, acting axially, is aligned with the supporting structure direction.

Point (a).2 is modified to

2 No flawise bending moment is transmitted to the nacelle.

(d) **Windplane mounted on a tower**
The generator can be moved from the nacelle to the lifting body (wing), using small wind turbines.

Point (a).3, (a).4 and (a).5 are modified to

3 The tangential aerodynamic component of lift and drag is equal to the wind turbines thrust, necessary to produce electric power.

4 No edgewise bending moment is transmitted to the ground station.

5 The wing center of mass moves vertically, so that there is an exchange of potential energy over one revolution.

Since no edgewise nor flapwise bending moments are transmitted to the nacelle, the corresponding supporting structure is converted to a tensile structure (i.e. a tether).

(e) **Windplane**
As the tether can be used to reach higher altitudes, the tower is removed.

Point (a).6 is modified to

6 The aerodynamic thrust is discharged at the ground via tensile force in the tether.

This thesis investigates the design of a windplane mounted on a tower (d), as this configuration allows an easier understanding of the physics. Moreover, we expect the design of the final configuration (e) to be similar to the design of configuration (d).

After having understood the physics behind configuration (d), the methodologies developed in this thesis can be applied to configuration (e) and other AWE topologies (Ground-Gen AWESs and rotational).

1.3 Thesis outline

In this thesis, no knowledge of airborne wind energy is assumed in the derivations and analyses. To make the main text easier to read, the state of the art and some open questions are discussed at the end of each chapter.

This thesis is organized in two parts, which are to be read sequentially.

In Part I, the windplane is modeled as a point mass and simplified models of the key physical aspects are derived. The main research question addressed in the first part is: "**Given a wingspan, which design maximizes power?**" This Part is divided into three Chapters

Chap. 2: In this chapter, we write the point mass equations of motion in a cylindrical coordinate system. By neglecting gravity, we find a steady-state equation of motion and an idealized power equation. This power equation is a function of geometrical and aerodynamic quantities of the windplane and control inputs. We finally define a power coefficient by normalizing the generated power with the wind power passing through a disk with radius equal to the windplane wing span. This power coefficient definition allows us to compare windplanes for a given wing span.

Chap. 3: In this chapter, we characterize the windplane parasite aerodynamic drag and the aerodynamic induction to populate the power equation derived in Chap. 2. The aerodynamic drag is composed of mainly two terms: the airfoil drag and the equivalent tether drag.

Chap. 4: In this chapter, we look for a solution of the equations of motion, including gravity and periodic control inputs. We formulate an optimal control problem (OCP), where the optimizer modifies the control variables to maximize the mean power. Later, the OCP is upgraded to an optimal design problem, where the optimizer

modifies the control variables and the design variables to maximize the mean power. The optimal windplane designs are then analyzed.

Before moving to Part II, the reader should make sure that the key concepts of Part I are well understood.

In Part II, the windplane is modeled as a rigid body and the design framework *T-GliDe* (Tethered Gliding systems Design) is introduced. The main research question addressed in the second part is: "**Can windplanes fly stable orbits?**" This part is divided into four Chapters

Chap. 5: In this chapter, the nonlinear equations of motion of the windplane modeled as a rigid body are derived.

Chap. 6: In this chapter, the aerodynamics of the windplane is analytically linearized about given nonlinear operating points.

Chap. 7: In this chapter, the design framework T-GliDe (Tethered Gliding systems Design) is introduced. T-GliDe solves the nonlinear equations of motion with an harmonic balance method. The results of an optimal control problem are analyzed.

Chap. 8: In this chapter, the nonlinear equations of motion are linearized about a representative point. The windplane eigendynamics of the linearized problem is studied.

In Chap. 9, the methodology used in the development of a reference economic model for airborne wind energy is presented.

Finally, in Chap. 10 the main conclusions of the thesis are summarized and a nomenclature is given in Chap. 11

Part I

Point mass

Given a wingspan, which design maximizes power?

CHAPTER 2

Equations of motion

In this chapter, we model the windplane as a point mass and we write its equations of motion in a cylindrical reference frame. We look for a steady-state solution by removing gravity from the external forces and we use the resulting relations to derive a power equation. Finally, we define a power coefficient, which will be used throughout all this thesis.

2.1 Coordinate systems

We start by introducing the three coordinate systems we use to write the equations of motion.

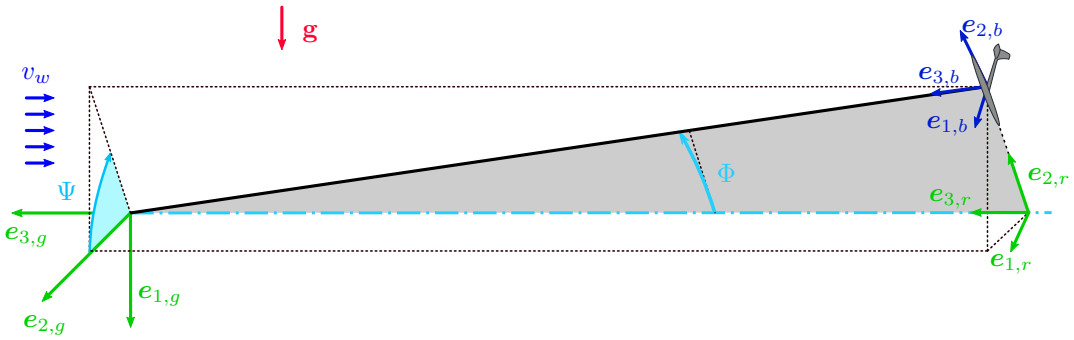

Figure 2.1: *Ground coordinate system $\mathcal{F}_G$, Rotating coordinate system $\mathcal{F}_R$ and Body coordinate system $\mathcal{F}_B$.*

Referring to Fig. 2.1, the ground coordinate system $\mathcal{F}_G$ is inertial and fixed at the

tether attachment at the ground station. Its versor $\boldsymbol{e}_{1,g}$ points to the ground and $\boldsymbol{e}_{3,g}$ upwind. A second coordinate system $\mathcal{F}_R$ (Rotating) is defined such that it moves with an angular velocity $\dot{\Psi}$ around $\boldsymbol{e}_{3,g}$ and $\boldsymbol{e}_{2,r}$ points to the tether attachment at the windplane. When $\Psi = 0$, $\mathcal{F}_G$ and $\mathcal{F}_R$ are parallel. The third coordinate system $\mathcal{F}_B$ (Body) is attached to the the windplane and it is centered at the tether attachment, denoted with T. The rotational matrices between these reference systems, which are not necessary here, are derived in Sect. 5.1. The position of $\mathcal{F}_B$ with respect to $\mathcal{F}_G$, expressed in $\mathcal{F}_R$ is

$$\boldsymbol{X}_{G\to T}^{R} = L_{te} \begin{bmatrix} 0 \\ \sin\Phi \\ -\cos\Phi \end{bmatrix} = \begin{bmatrix} 0 \\ r \\ -z \end{bmatrix}, \tag{2.1}$$

where L_{te} is the tether length and Φ is called the opening angle.

2.2 Equations of motion

We now write the equations of motion of the windplane, modeled as a point mass, in $\mathcal{F}_R$. The external forces acting on the windplane are the aerodynamic force $\boldsymbol{F}_a$, the tensile force $\boldsymbol{T}$ acting on the tether and the gravitational force $m\boldsymbol{g}$.

The aerodynamic force $\boldsymbol{F}_a$ in $\mathcal{F}_R$ is

$$\boldsymbol{F}_a = \begin{bmatrix} F_{a,1} \\ F_{a,2} \\ F_{a,3} \end{bmatrix}. \tag{2.2}$$

The tether tensile force $\boldsymbol{T}$ acting on the point mass is expressed as function of its axial component T as

$$\boldsymbol{T} = T \begin{bmatrix} 0 \\ -\tan\Phi \\ 1 \end{bmatrix}. \tag{2.3}$$

The gravitational force $m\boldsymbol{g}$ is

$$m\boldsymbol{g} = mg \begin{bmatrix} \cos\Psi \\ -\sin\Psi \\ 0 \end{bmatrix}, \tag{2.4}$$

where m is the windplane mass and g is the gravitational acceleration.

The equations of motion then read

$$\begin{cases} m\dot{u} + 2m\dot{r}u = F_{a,1} + mg\cos\Psi \\ m\ddot{r} - m\frac{u^2}{r} = F_{a,2} - T\tan\Phi - mg\sin\Psi \\ m\ddot{z} = F_{a,3} + T \end{cases} \tag{2.5}$$

where u is the tangential velocity, $2m\dot{r}u$ is the Coriolis force and $m\frac{u^2}{r}$ the centrifugal force.

2.3 Steady-state

We look for a steady-state solution of the equations of motion in (2.5) by removing the periodic input given by gravity. In absence of gravity, the steady equations of motion are

$$\begin{cases} F_{a,1} = 0 \\ m\frac{u^2}{R_0} = T\tan\Phi - F_{a,2} \\ T = -F_{a,3} \end{cases} \tag{2.6}$$

where R_0 is the trajectory radius in steady-state.

We need now to characterize the aerodynamic force. In this chapter, we assume the wing span direction $\boldsymbol{e}_{2,b}$ to be aligned with $\boldsymbol{e}_{2,r}$. In this condition, the projected crosswind area is maximized, such that the windplane "catches as much wind as possible". Moreover, the aerodynamic lift is exclusively used for power generation and, consequently, the aerodynamic forces do not have any radial component $F_{a,2} = 0$.

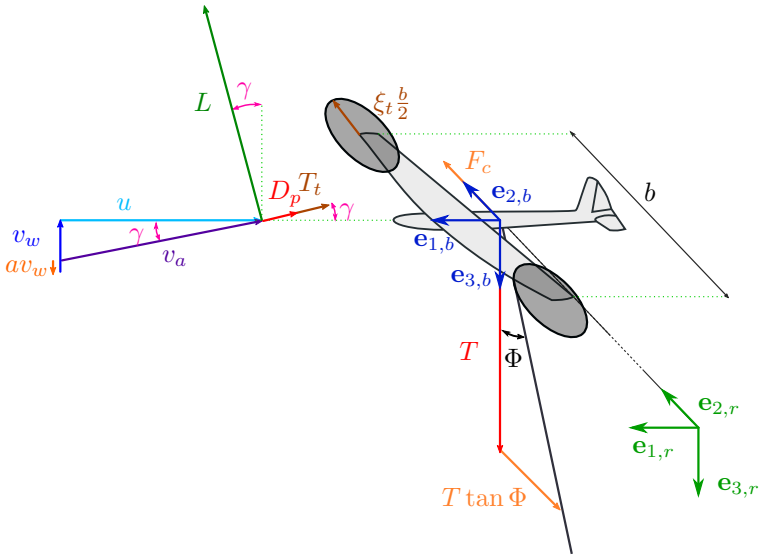

Figure 2.2: *Velocity triangle and forces acting on a windplane in steady-state.*

Referring to Fig. 2.2, the aerodynamic lift L and the parasite drag D_p are, by definition, perpendicular and parallel to the apparent velocity v_a, respectively. The onboard wind turbines thrust T_t is assumed to be parallel to the drag. The induced velocities are av_w, where a is the aerodynamic induction. The aerodynamic force can then be written as

$$\boldsymbol{F}^a = \begin{bmatrix} L\sin\gamma - (D_p + T_t)\cos\gamma \\ 0 \\ L\cos\gamma + (D_p + T_t)\sin\gamma \end{bmatrix}, \tag{2.7}$$

where the inflow angle γ is

$$\tan\gamma = \frac{v_w(1-a)}{u} = \frac{(1-a)}{\lambda}, \tag{2.8}$$

and λ is the wing speed ratio.

The system of equations 2.6 then become

$$\begin{cases} L\sin\gamma - (D_p + T_t)\cos\gamma = 0 \\ m\frac{u^2}{R_0} = T\tan\Phi \\ T = L\cos\gamma + (D_p + T_t)\sin\gamma \end{cases} \tag{2.9}$$

Considering Eq. (2.8), the steady-state equations of motion are re-written as

$$\begin{cases} \lambda = \frac{L}{D_p+T_t}(1-a) \\ \tan\Phi = \frac{mu^2}{TR_0} \\ T = L\cos\gamma\left(1 + \frac{D_p+T_t}{L}\frac{(1-a)}{\lambda}\right) \approx L \end{cases} \tag{2.10}$$

where in the third equation (axial equilibrium), large values of λ are assumed ($\lambda^2 \gg 1$).

2.4 Geometry

In order to further characterize the steady-state equilibrium in Eq. (2.10), we need to define a few geometrical quantities. Referring to Fig. 2.2, we denote the windplane wing span as b. The wing area A is

$$A = \frac{b^2}{AR}, \tag{2.11}$$

where AR is the wing aspect ratio. The onboard wind turbine radius is expressed as function of the wing semi-span as

$$R_t = \xi_t \frac{b}{2}. \tag{2.12}$$

Assuming two turbines, the total rotor area A_t is

$$A_t = 2 \cdot \pi R_t^2 = \frac{\pi \xi_t^2}{2} b^2. \tag{2.13}$$

2.5 Wing speed ratio estimation

The wing speed ratio is found in Eq. (2.10) to be $\lambda = \frac{L}{D_p+T_t}(1-a)$, where L is the lift, a the induction, D_p the parasite drag and T_t turbine thrust.

The aerodynamic lift is

$$L = \frac{1}{2}\rho A C_L v_a^2, \tag{2.14}$$

where C_L is the lift coefficient. The aerodynamic parasite drag is

$$D_p = \frac{1}{2}\rho A C_{D,p} v_a^2, \tag{2.15}$$

where $C_{D,p}$ is the parasite drag coefficient. The thrust force produced by the onboard wind turbines is

$$T_t = \frac{1}{2}\rho A_t C_{T,t} v_a^2, \tag{2.16}$$

where $C_{T,t}$ is the thrust coefficient of the onboard wind turbines.

The wing speed ratio is then

$$\lambda = \frac{\frac{1}{2}\rho A C_L v_a^2}{\frac{1}{2}\rho A (C_{D,p} + \frac{A_t}{A} C_{T,t}) v_a^2}(1-a) = \frac{C_L(1-a)}{C_{D,p} + \frac{\pi}{2} AR \xi_t^2 C_{T,t}}. \tag{2.17}$$

2.6 Power and thrust coefficients

The power equation can be written with respect to the onboard turbines as

$$P = \frac{1}{2}\rho A_t C_{P,t} v_a^3 \approx \frac{1}{2}\rho A_t C_{P,t} \lambda^3 v_w^3, \tag{2.18}$$

where $C_{P,t}$ is the power coefficient of the onboard wind turbines and large values of λ are assumed ($\lambda^2 \gg 1$).

Taking inspiration from conventional wind energy, we define the power coefficient by normalizing the power P with the power of the wind passing through a reference area A_{ref}

$$C_P = \frac{P}{\mathbb{P}} = \frac{P}{\frac{1}{2}\rho A_{\text{ref}} v_w^3}. \tag{2.19}$$

The thrust coefficient is defined as the dot product of the resultant aerodynamic force and the wind speed, normalized with $\mathbb{P}$

$$C_T = \frac{\boldsymbol{F}_a \cdot \boldsymbol{v}_w}{\mathbb{P}} \approx \frac{L}{\frac{1}{2}\rho A_{\text{ref}} v_w^2} \tag{2.20}$$

where $\boldsymbol{v}_w = -v_w \boldsymbol{e}_{3,r}$

We take A_{ref} as the area of a disc with radius equal to the AWES wing span $A_{\text{ref}} = \pi b^2$ (orange area in Fig. 2.3). In this way, A_{ref} is a value defined by the geometry of the system, as for conventional wind turbines, and allows to compare AWESs for a given wing span.

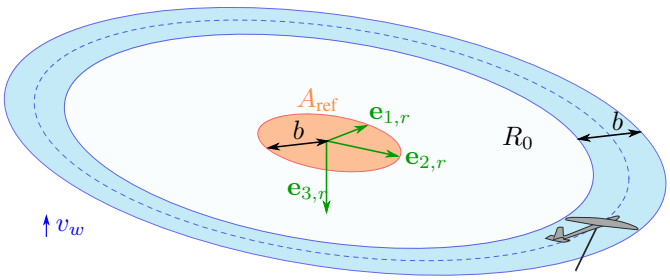

Figure 2.3: *Reference area for the power coefficient evaluation.*

The power coefficient is then

$$C_P = C_{P,t} \frac{\xi_t^2}{2} \lambda^3, \tag{2.21}$$

and the thrust coefficient

$$C_T = \frac{C_L}{\pi AR} \lambda^2. \tag{2.22}$$

2.7 Power balance

The power balance equation is derived by performing the dot-product of the steady-state equation of motion (Eq. 2.9) with the plane velocity, which results in

$$L \sin \gamma u - (D_p + T_t) \cos \gamma u = 0 \tag{2.23}$$

Writing $\tan \gamma = \frac{(1-a)}{\lambda}$ (Eq. 2.8) and inserting the definition of lift L, parasite drag D_p and turbines thrust T_t (Sec. 2.5), the power balance equation become

$$\frac{1}{2}\rho A C_L \lambda^3 v_w^3 \frac{(1-a)}{\lambda} - \frac{1}{2}\rho A C_{D,p} \lambda^3 v_w^3 = \frac{1}{2}\rho A_t C_{T,t} \lambda^3 v_w^3. \tag{2.24}$$

We can now normalize it with $\mathbb{P} = \frac{1}{2}\rho \pi b^2 v_w^3$, similarly to what done for the power and thrust coefficient definition, as

$$\underbrace{\frac{C_L}{\pi AR}\lambda^2}_{C_T}(1-a) - \underbrace{\frac{C_{D,p}}{\pi AR}\lambda^3}_{C_\tau} = \underbrace{\frac{\xi_t^2}{2} C_{T,t}\lambda^3}_{\frac{C_{T,t}}{C_{P,t}}C_P}, \tag{2.25}$$

which in compact form can be written as

$$\underbrace{C_T(1-a) - C_\tau}_{C_a} = \frac{C_{T,t}}{C_{P,t}} C_P. \tag{2.26}$$

The left-hand-side represents the aerodynamic power C_a, where $C_T(1-a)$ is the wind power and C_τ is the power dissipated in parasite drag. The right-hand-side $\frac{C_{T,t}}{C_{P,t}}C_P$ is the onboard turbines thrust power.

Modeling the onboard turbines with momentum theory $\frac{C_{P,t}}{C_{T,t}} = (1-a_t)$, where a_t is the axial induction of the onboard turbines, and neglecting the power dissipated in parasite drag C_τ, we get to

$$\frac{C_P}{C_T} = (1-a)(1-a_t) \approx (1-a-a_t). \tag{2.27}$$

2.8 Discussion

In this chapter, we model the windplane as a point mass and we introduce its equations of motion in a cylindrical reference frame. We first look for a steady-state solution by removing the contribution of gravity from the external forces. We assume that aerodynamic forces are just acting in the tangential and axial direction so that the aerodynamic lift is just used for power generation and not for turning. This reveals key relations between the dynamic and kinematic quantities. We finally derive a power equation and define a power coefficient by normalizing the power with the wind power passing through a disc with radius equal to the plane wing span, allowing us to compare concepts for given wing spans.

The power coefficient is a function of the onboard wind turbines power coefficient $C_{P,t}$, their non-dimensional radius ξ_t and the wing speed ratio λ (Eq. 2.21). The wing

speed ratio λ is a function of the lift C_L and parasite drag $C_{D,p}$ coefficients, the axial induction a, the wing aspect ratio AR, the onboard turbines thrust coefficient $C_{T,t}$ and ξ_t (Eq. 2.17).

To estimate the power coefficient for a given design, we need to understand which parameters are independent variables and which need to be modeled as a function of these variables. The geometrical parameters ξ_t and AR are independent variables as they are fixed for a given design. $C_{T,t}$ and $C_{P,t}$ are typically functions of each other through the turbine axial induction, which is a control variable. C_L is also a control variable, as any feasible lift coefficient can be obtained by pitching the wing. We then need to model the parasite drag coefficient $C_{D,p}$ and the axial induction a as a function of the independent and control variables, to get to a realistic estimation of the power coefficient. This is the topic of Chapter 3.

Once the drag coefficient and the axial induction are modeled, we need to understand how gravity is modifying the solution and quantify its impact on the power coefficient and on the system design. This is the topic of Chapter 4.

2.9 State of the art and open questions

2.9.1 Power equation

The first theoretical power equation of crosswind AWESs is derived by Loyd (1980), for given lift and drag coefficients of the system. In the book *Airborne Wind Energy* (Ahrens et al. (2013)), we find many contributions to the physical understanding of crosswind AWESs. Diehl (2013) introduce the basic concepts and physical foundation of Fly-Gen and Ground Gen AWES. Schmehl et al. (2013); Luchsinger (2013); Argatov and Silvennoinen (2013) develop further the modeling of Ground-Gen AWESs. Vander Lind (2013) presents the modeling of a Fly-Gen AWES, accounting for the onboard wind turbine induction. Later, Trevisi et al. (2020b) unify the modeling of Fly-Gen and Ground-Gen, getting to a unified power equation. The windplane power equation is written as an explicit function of the thrust and power coefficient of the onboard turbines for the first time in this thesis, to the best of the author's knowledge.

2.9.2 Lateral equilibrium

The effect of centrifugal forces on power production is investigated by Luchsinger (2013), assuming they are balanced by a component of lift, obtained by rolling the plane. Trevisi et al. (2020a) write the equations of motion in a cylindrical reference system, finding then that it exists one opening angle Φ that maximizes power production (second equation in (2.10)). The power losses for other opening angles are also quantified. Tucker (2020) investigates optimal flight radii and derives a similar expression to the one presented here for the later equilibrium, with the assumption of small opening angles Φ.

Note that if the lateral equilibrium, as written in the second equation of (2.10), is fulfilled, the radial component of the tether force is used to turn and the aerodynamic lift is just used for power production. This might not be possible for extremely light topologies (e.g. soft kites or bi-planes) as the resulting flight radius would be too small. Therefore, for those topologies, a component of the aerodynamic force needs to be used

to turn and different trajectories than circular might be optimal.

2.9.3 Power coefficient definition

The most commonly used metric in AWE is the power harvesting factor, defined by taking as reference area in Eq. (2.19) the wing area A. This allows us to compare systems for a given wing area. It is defined by Diehl (2013) and used by Schmehl et al. (2013); Vander Lind (2013); Bauer et al. (2018); Tucker (2020) among others. Performing a system design based on the power harvesting factor would answer the question: "Given a wing area, which system design maximizes power?"

The power coefficient as defined in this thesis is introduced by Trevisi et al. (2023b). This enables to compare systems for a given wing span. Performing a system design based on this power coefficient would answer the question: "Given a wing span, which system design maximizes power?" This thesis gives an attempt of answering to the latter question.

CHAPTER 3

Parasite drag and aerodynamic induction

In this chapter, we investigate the main sources of parasite aerodynamic drag and the aerodynamic induction of windplanes. In the first part of this thesis, the drag produced by the stabilizer, the fuselage, and the turbines' nacelles is neglected, so that the windplane parasite drag coefficient can be written as

$$C_{D,p} = C_d + C_{D,te}, \tag{3.1}$$

where C_d is the airfoil drag coefficient and $C_{D,te}$ is the coefficient modeling the equivalent tether drag.

In the following two sections, we characterize these two drag sources. In Sect. 3.3, the aerodynamic induction is modeled. In Sect. 3.4, we summarize the main results that we will use in this thesis.

3.1 Airfoil drag

We model the airfoil drag in an idealized way by writing the drag coefficient C_d as function of the lift coefficient

$$C_d = C_{d,0} + k_d C_L^2, \tag{3.2}$$

where $C_{d,0}$ and k_d are parameters of the selected airfoil at the given Reynolds number.

We assume in this thesis an airfoil *NACA 2412*, for which the airfoil characteristics are well known in the literature and a Reynolds number $R_e = 10^6$. From the airfoil polars, we can estimate the coefficients of Eq. (3.2). In Figures 3.1a and 3.1b the approximated airfoil drag coefficient and the approximated airfoil lift to drag ratio are compared with the airfoil polars obtained with Xfoil. In Table 3.1, the estimated coefficients and the condition at maximum lift to drag ratio are listed.

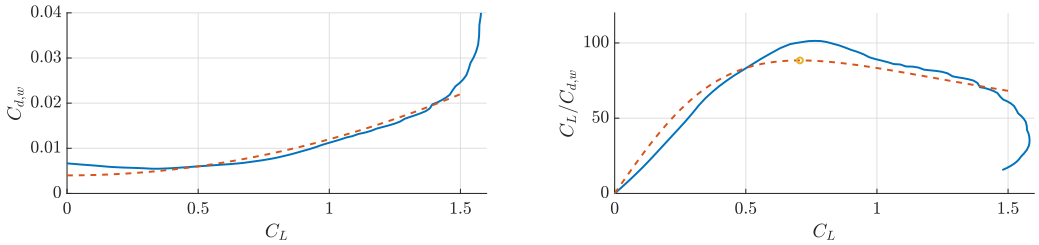

(a) *NACA 2412 drag coefficient at Reynolds number* $Re = 10^6$. *Data from Xfoil (-) and analytical approximation (- -).*

(b) *NACA 2412 lift to drag ratio at Reynolds number* $Re = 10^6$. *Data from Xfoil (-) and analytical approximation (- -).*

Figure 3.1

Table 3.1: *Coefficients for the NACA 2412 drag coefficient estimation (Eq. 3.2) and maximum lift to drag ratio.*

$R_e = 10^6$	$C_{d,0} = 0.004 \quad k_d = 0.008$	$\frac{C_L}{C_d}(C_L = 0.70) = 88$

3.2 Tether drag

The drag acting on the tether is a distributed force over its length. We denote the nondimensional curvilinear coordinate running along the tether length as ξ_{te}, which ranges from 0 to 1. The tether section at the ground station ($\xi_{te} = 0$) is fixed, while the section at the windplane ($\xi_{te} = 1$) moves with the same velocity of the windplane u. The aerodynamic drag experienced by each tether section can be approximated with

$$d(\xi_{te}) = \frac{1}{2}\rho D_{te} C_{d,te} u^2 \left(\frac{\xi_{te}}{L_{te}}\right)^2, \tag{3.3}$$

where D_{te} is the tether diameter section and $C_{d,te}$ is the tether section drag coefficient. The term $u\frac{\xi_{te}}{L_{te}}$ indicates the apparent velocity at each tether section, neglecting the contribution from the wind speed.

The aerodynamic drag generates a moment at the ground station M_{te}

$$M_{te} = \int_0^1 L_{te}\xi_{te} \cdot d(\xi_{te}) d\xi_{te} = \left(\frac{1}{2}\rho D_{te} C_{d,te} u^2\right) L_{te} \int_0^1 \xi_{te}^3 d\xi_{te} = \left(\frac{1}{2}\rho D_{te} C_{d,te} u^2\right) \frac{L_{te}}{4}. \tag{3.4}$$

We look for an equivalent drag force D_{eq}, which can be lumped with windplane. The moment that this equivalent drag generates at the ground station needs to be equal to the one given in Eq. (3.4). The moment generated by the equivalent drag is

$$M_{te} = L_{te} D_{eq} = L_{te}\left(\frac{1}{2}\rho A C_{D,te} u^2\right), \tag{3.5}$$

where $C_{D,te}$ is the equivalent drag coefficient. By setting Eq. (3.4) equal to Eq. (3.5), the equivalent tether drag coefficient is

$$C_{D,te} = C_{d,te}\frac{D_{te} L_{te}}{4A}. \tag{3.6}$$

By defining the tether diameter ratio as

$$d_{te} = \frac{D_{te}}{b/2}, \tag{3.7}$$

and the tether length ratio as

$$l_{te} = \frac{L_{te}}{b/2}, \tag{3.8}$$

the equivalent tether drag coefficient can be expressed as function of non-dimensional quantities as

$$C_{D,te} = \frac{C_{d,te}}{16} d_{te} l_{te} \text{Æ}. \tag{3.9}$$

3.3 Aerodynamic induction

The aerodynamic induction measures how much the wind is slowed down by the windplane. It physically corresponds to the velocity induced by the windplane trailed vortices, which have a helicoidal shape, on the wing itself. The strength of the vortices is determined by the span-wise lift distribution. The velocities induced by the trailed vortices reduce the wind velocity and effectively rotate the apparent velocity, composed of the undisturbed wind velocity and the windplane velocity, by an induced angle. Since the aerodynamic lift is defined to be perpendicular to the local apparent velocity, it is rotated by the induced angle. The component of lift parallel to the undisturbed apparent velocity can be modeled as the induced drag.

In Sect. 3.3.1, we introduce the modeling of the induction produced by a helicoidal vortex filament. The helicoidal vortex filament can be described as a near vortex filament, modeled by the first half revolution of the filament in the rotor plane, and a far vortex filament, modeled by an infinite series of vortex rings. In Sect. 3.3.2, the near wake model and the relative induced drag coefficient are derived. In Sect. 3.3.3, the far wake model, which depends on the radial (known) and axial (unknown) position of the vortex rings and the relative induced drag coefficient are derived. A closure model is finally proposed to find the axial position of the vortex rings.

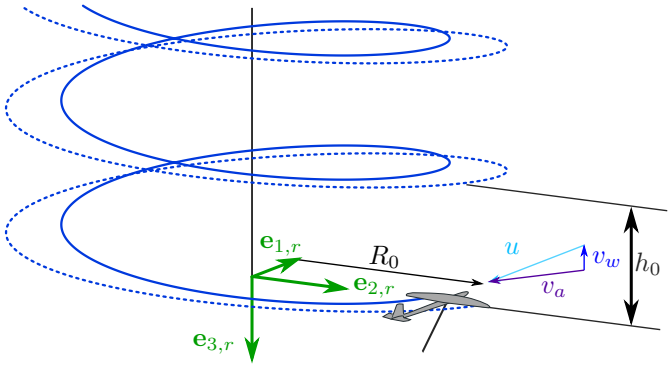

Figure 3.2: *Wake structure of a windplane flying circular trajectories. The solid and dashed lines represent the left and right rolled up trailed vortices respectively.*

3.3.1 Modeling of a helicoidal vortex filament

Referring to Fig. 3.2, we assume that the windplane moves along a circular trajectory with radius R_0 with a constant velocity u. The vortices trailed by the windplane are transported downwind by the wind and have a helicoidal shape. It is assumed no distortion and expansion of the wake. The geometry of the helicoidal vortex filament is shown in Fig. 3.3a.

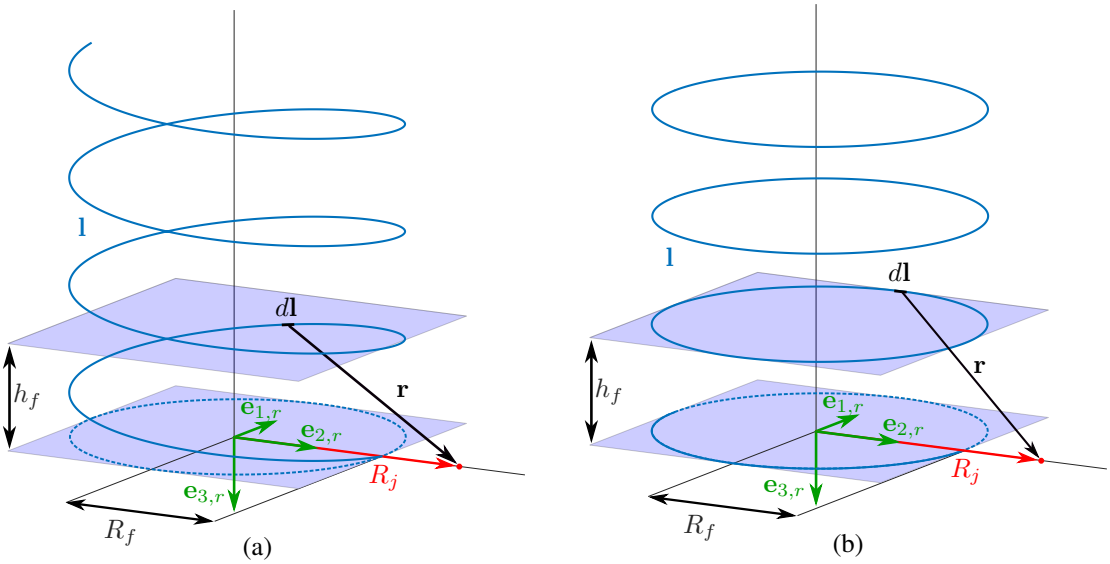

Figure 3.3: ***(a)*** *Helicoidal vortex filament and* ***(b)*** *relative modeling after assumptions.*

The radius of the filament is R_f and the pitch h_f. The filaments are trailed by a lifting line, placed along the direction $\boldsymbol{e}_{2,r}$. The induction is evaluated at a generic point $\boldsymbol{p}_j$ on the lifting line, with radius R_j. With these definitions, the radial difference ΔR between the evaluation point and the filament is

$$\Delta R = R_j - R_f, \tag{3.10}$$

and it is normalized with the evaluation radius as

$$\eta = \frac{\Delta R}{R_j} = 1 - \frac{R_f}{R_j}. \tag{3.11}$$

Note that $\eta = 0$ when $\Delta R = 0$, $\eta = 1$ when $R_j \to +\infty$ and $\eta \to -\infty$ when $R_j \to 0$. The normalized position of the vortex filament with respect to the mid-span turning radius R_0 (see Fig. 3.2) is indicated as

$$\eta_0 = \frac{R_0 - R_f}{R_0} = -\frac{y_f}{R_0}, \tag{3.12}$$

where y_f indicates the position of the vortex filament along the wing span direction. The filament radius R_f can then be expressed as

$$R_f = R_j\,(1 - \eta) = R_0\,(1 - \eta_0)\,. \tag{3.13}$$

Assuming that the helix pitch of any vortex filament h_f trailed by the wing is equal to the helix pitch h_0 of the vortex filament at the wing center, the normalized torsional

parameter λ_0 is the ratio between the projected circumference length $2\pi R_0$ and the helix pitch h_0 of the vortex filament

$$\lambda_0 = \frac{2\pi R_0}{h_0} = \frac{2\pi}{1-\eta_0}\frac{R_f}{h_0}. \tag{3.14}$$

The helix can be modeled as

$$\boldsymbol{l} = \begin{bmatrix} -R_f \sin\theta \\ R_f \cos\theta \\ -h_0 \frac{\theta}{2\pi} \end{bmatrix} = R_f \begin{bmatrix} -\sin\theta \\ \cos\theta \\ -\frac{1}{1-\eta_0}\frac{\theta}{\lambda_0} \end{bmatrix}, \tag{3.15}$$

where $\theta \in [0, \infty[$ is the angular parameter of the helix.

The induced velocities $\boldsymbol{w}_{j,f}$ produced by the filament of vorticity Γ at a point $\boldsymbol{p}_j$ is found using Biot-Savat law

$$\boldsymbol{w}_{j,f} = \frac{\Gamma}{4\pi}\int_0^{+\infty} \frac{d\boldsymbol{l} \times \boldsymbol{r}}{|\boldsymbol{r}|^3}, \tag{3.16}$$

where

$$d\boldsymbol{l} = -R_f \begin{bmatrix} \cos\theta \\ \sin\theta \\ \frac{1}{1-\eta_0}\frac{1}{\lambda_0} \end{bmatrix} d\theta, \tag{3.17}$$

and $\boldsymbol{r} = \boldsymbol{p}_j - \boldsymbol{l}$. We assume that the evaluation point $\boldsymbol{p}_j$ is on the lifting line itself

$$\boldsymbol{p}_j = \begin{bmatrix} 0 \\ R_j \\ 0 \end{bmatrix}, \tag{3.18}$$

so that $\boldsymbol{r}$ is

$$\boldsymbol{r} = \begin{bmatrix} 0 \\ R_j \\ 0 \end{bmatrix} - \begin{bmatrix} -R_f \sin\theta \\ R_f \cos\theta \\ -\frac{R_f}{1-\eta_0}\frac{\theta}{\lambda_0} \end{bmatrix} = \begin{bmatrix} R_f \sin\theta \\ R_j - R_f \cos\theta \\ \frac{R_f}{1-\eta_0}\frac{\theta}{\lambda_0} \end{bmatrix}. \tag{3.19}$$

When looking for the axial induced velocity $w_{j,f} = \boldsymbol{w}_{j,f} \cdot \boldsymbol{e}_3$, the third component of the numerator of Eq. (3.16) becomes

$$\begin{aligned} (d\boldsymbol{l} \times \boldsymbol{r}) \cdot \boldsymbol{e}_3 &= -R_f(R_j \cos\theta - R_f \cos\theta^2 - R_f \sin\theta^2) \\ &= -R_j^2(1-\eta)\left(\cos\theta - (1-\eta)\right) d\theta. \end{aligned} \tag{3.20}$$

The norm of $\boldsymbol{r}$ squared can be expressed as

$$\begin{aligned} |\boldsymbol{r}|^2 =& R_f^2 \sin\theta^2 + (R_j - R_f\cos\theta)^2 + \left(\frac{R_f}{1-\eta_0}\frac{\theta}{\lambda_0}\right)^2 \\ =& \underbrace{R_j^2\left(1 - 2\left(1-\eta\right)\cos\theta + (1-\eta)^2\right)}_{|\boldsymbol{r}_{1,2}|^2} + \left(\frac{R_f}{1-\eta_0}\frac{\theta}{\lambda_0}\right)^2, \end{aligned} \tag{3.21}$$

where a distinction between the distance in the rotor plane $(\boldsymbol{e}_{1,r}, \boldsymbol{e}_{2,r})$ and in the axial direction is made. Note that $|\boldsymbol{r}_{1,2}|$ is a periodic function of θ.

The Biot-Savat law (Eq. 3.16) can be re-written considering (3.21) as

$$w_{j,f} = \frac{\Gamma}{4\pi} \int_0^{+\infty} \frac{(d\boldsymbol{l} \times \boldsymbol{r}) \cdot \boldsymbol{e}_3}{\left(|\boldsymbol{r}_{1,2}|^2 + \left(\frac{R_f}{1-\eta_0} \frac{\theta}{\lambda_0} \right)^2 \right)^{\frac{3}{2}}}. \tag{3.22}$$

By splitting the integration interval as $[0, +\infty[= [0, \pi] \cup [\pi, 3\pi] \cup [3\pi, 5\pi] \cup .. = [0, \pi] \cup \bigcup_{k=1}^{\infty} (2\pi k + [-\pi, +\pi])$, the integral can be re-written as an infinite summation of integrals. By properly re-writing the non-periodic terms, Eq. (3.22) becomes

$$w_{j,f} = \underbrace{\frac{\Gamma}{4\pi} \int_0^{\pi} \frac{(d\boldsymbol{l} \times \boldsymbol{r}) \cdot \boldsymbol{e}_3}{\left(|\boldsymbol{r}_{1,2}|^2 + \left(\frac{R_f}{1-\eta_0} \frac{\theta}{\lambda_0} \right)^2 \right)^{\frac{3}{2}}}}_{\text{near vortex filament}} + \underbrace{\frac{\Gamma}{4\pi} \sum_{k=1}^{\infty} \int_{-\pi}^{\pi} \frac{(d\boldsymbol{l} \times \boldsymbol{r}) \cdot \boldsymbol{e}_3}{\left(|\boldsymbol{r}_{1,2}|^2 + \left(\frac{R_f}{1-\eta_0} \frac{2\pi k + \theta}{\lambda_0} \right)^2 \right)^{\frac{3}{2}}}}_{\text{far vortex filament}}. \tag{3.23}$$

In Eq. 3.23 a distinction between near and far vortex filament is done, noting that the near vortex filament (i.e. the first integral) models the induction produced by the first half revolution of the filament, whereas the far vortices are modeled through the infinite summation of integrals.

The integrals modeling the near and the far vortex filament have terms proportional to θ in the denominator. These terms physically represent the contribution to $|\boldsymbol{r}|$ from the projection of $\boldsymbol{r}$ along $\boldsymbol{e}_{3,r}$ and they have a maximum value at $\theta = \pm\pi$, which is also where the projection of $\boldsymbol{r}$ in the $(\boldsymbol{e}_{1,r}, \boldsymbol{e}_{2,r})$ plane is largest. This suggests that the overall contribution of the terms proportional to θ to the integral should be limited.

By neglecting the terms proportional to θ, the helicoidal vortex filament model of Fig. 3.3a reduces into the model of Fig. 3.3b (i.e. half a vortex ring plus a semi-infinite vortex rings cascade). The axial velocity at point $\boldsymbol{p}_j$, induced by the idealized helicoidal vortex filament, is then approximated as

$$w_{j,f} \approx \frac{\Gamma}{4\pi} \int_0^{\pi} \frac{(d\boldsymbol{l} \times \boldsymbol{r}) \cdot \boldsymbol{e}_3}{|\boldsymbol{r}_{1,2}|^3} + \frac{\Gamma}{4\pi} \sum_{k=1}^{\infty} \int_{-\pi}^{\pi} \frac{(d\boldsymbol{l} \times \boldsymbol{r}) \cdot \boldsymbol{e}_3}{\left(|\boldsymbol{r}_{1,2}|^2 + \left(\frac{R_f}{1-\eta_0} \frac{2\pi k}{\lambda_0} \right)^2 \right)^{\frac{3}{2}}}, \tag{3.24}$$

which in extended form is

$$w_{j,f} \approx -\frac{\Gamma}{4\pi\Delta R} \left[\int_0^{\pi} \frac{\eta\,(1-\eta)\,(\cos\theta - (1-\eta))}{\left(1 - 2\,(1-\eta)\cos\theta + (1-\eta)^2\right)^{\frac{3}{2}}} d\theta + \right.$$
$$\left. + \sum_{k=1}^{\infty} \int_{-\pi}^{\pi} \frac{\eta\,(1-\eta)\,(\cos\theta - (1-\eta))}{\left(1 - 2\,(1-\eta)\cos\theta + (1-\eta)^2 + \left(\frac{1-\eta}{1-\eta_0} \frac{2\pi k}{\lambda_0} \right)^2 \right)^{\frac{3}{2}}} d\theta \right]. \tag{3.25}$$

The integrals involved in Eq. (3.25) have now a closed form solution, which are used to derive a near and a far wake model in the next sections. Recall that this expression

is derived by approximating the helicoidal vortex system of Fig. 3.3a with the vortex rings system of Fig. 3.3b to compute the induction, which is a good idealization when the normalized torsional parameters λ_0 of the helicoidal vortex filament is large.

3.3.2 Near wake model

In Sect. 3.3.1, the axial induced velocity produced by a helical vortex filament is modeled as half a vortex ring plus a semi-infinite vortex ring cascade, as in Fig. 3.3b. In this section, a near wake model is developed based on this idealization. The velocities induced at the windplane by the near vortex filaments trailed by the windplane itself are studied here, so that values of η (Eq. 3.11) are expected, and consequently assumed, to be small.

Velocity induced by the near vortex filament

The axial velocity at point $\boldsymbol{p}_j$ induced by the near vortex filament of intensity $d\Gamma$ is (Eq. 3.25)

$$dw^n_{j,f} = -\frac{d\Gamma}{4\pi\Delta R}\int_0^\pi \frac{\eta\left(1-\eta\right)\left(\cos\theta-\left(1-\eta\right)\right)}{\left(1-2\left(1-\eta\right)\cos\theta+\left(1-\eta\right)^2\right)^{\frac{3}{2}}}d\theta = -\frac{d\Gamma}{4\pi\Delta R}\Upsilon^n\left(\eta\right). \tag{3.26}$$

where the term outside the integral models the induced velocity produced by a semi-infinite straight vortex filament pointing in the $-\boldsymbol{e}_{1,r}$ direction. Υ^n can be then understood as the near vortex filament shape factor and the integral defining it has a close form solution

$$\Upsilon^n\left(\eta\right) = -\frac{\eta}{|\eta|}\left(K\left(\frac{\pi}{2}\middle|m\right)+\frac{\eta}{(\eta-2)}E\left(\frac{\pi}{2}\middle|m\right)\right) \tag{3.27}$$

where $K\left(\frac{\pi}{2}\middle|m\right)$ and $E\left(\frac{\pi}{2}\middle|m\right)$ are the complete elliptic integral of the first and second kind respectively. Eq. (3.27) can be linearized with respect to η, as its values for windplanes are expected to be small. Therefore, Υ^n becomes

$$\Upsilon^n\left(\eta\right) \approx 1-\eta\left(1-\frac{1}{4}\ln(\eta^2)\right) \tag{3.28}$$

Figure 3.4 shows the trend of Υ^n obtained with Eq. (3.27) (solid lines) and with the linearized version (Eq. 3.28) (dashed lines). The near vortex filament shape factor Υ^n can be interpreted as a corrective factor to the straight vortex filament solution due to the filament curvature. The following regions of η can be analyzed:

$\eta \to 1$ is obtained for $R_j >> R_f$ and $\Upsilon^n \to 0$, meaning that no velocities are induced.

$\eta > 0$ is obtained for $R_j > R_f$ and $\Upsilon^n < 1$, meaning that less velocities are induced compared to the straight filament case.

$\eta \to 0$ is obtained for $R_j \approx R_f$ or $(R_j \to \infty, R_f \to \infty)$ and $\Upsilon^n \to 1$, meaning that the filament curvature is negligible and the solution coincides with the straight filament case.

$\eta < 0$ is obtained for $R_j < R_f$ and $\Upsilon^n > 1$, meaning that more velocities are induced compared to the straight filament case.

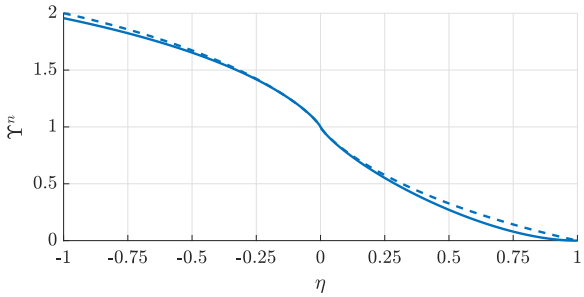

Figure 3.4: *Near vortex filament shape factor Υ^n as function of η for the complete solution (-) and with the linearized version (- -).*

$\eta \to -\infty$ is obtained for $R_j << R_f$, and $\Upsilon^n \to \pi$, as the evaluation point is close to the center of the half circle.

Induced drag coefficient due to the near wake for an elliptic lift distribution

We assume here an elliptic lift distribution, as it produces minimum induced drag in forward flight. We then take the bound vorticity Γ as

$$\Gamma = \Gamma_0 \sqrt{1 - \left(\frac{2y_f}{b}\right)^2}. \tag{3.29}$$

The trailed vorticity, according to Helmholtz' law, is the derivative of the bound vorticity with respect to the wing span coordinate

$$\frac{d\Gamma}{dy_f} = -\frac{4\Gamma_0}{b^2} \frac{y_f}{\sqrt{1 - \left(\frac{2y_f}{b}\right)^2}}. \tag{3.30}$$

The axial induced velocity $w_{j,n}$ on a point $\boldsymbol{p}_j$ along the lifting line due to the near wake is found by integrating the effects of the trailed vorticity along the wing span

$$w_{j,n} = -\frac{1}{4\pi} \int_{-b/2}^{b/2} \frac{(\partial\Gamma/\partial y_f)}{\Delta R} \Upsilon^n \, dy_f = \frac{\Gamma_0}{\pi b^2} \int_{-b/2}^{b/2} \frac{y_f}{\Delta R \sqrt{1 - \left(\frac{2y_f}{b}\right)^2}} \Upsilon^n dy_f. \tag{3.31}$$

By changing the integration variable as $y_f = \frac{b}{2}\cos\theta$ and considering $\Upsilon^n = 1$ [1], the integral has an analytical solution

$$w_n = -\frac{\Gamma_0}{2b}, \tag{3.32}$$

meaning that the induced velocities are constant over the lifting line.

The aerodynamic lift can be found with the Kutta-Joukowski relation

$$L = \rho u \Gamma_0 \int_{-b/2}^{b/2} \sqrt{1 - \left(\frac{2y_f}{b}\right)^2} dy_f = \rho u \Gamma_0 \frac{b}{4}\pi, \tag{3.33}$$

where we assume u to be constant over the wing span [1].

[1] This is a good approximation only when looking at integral quantities and not when analyzing induced velocities along the wing span. See Trevisi et al. (2023a) for more details.

By writing the lift as $L = \frac{1}{2}\rho A C_L u^2$, we solve for Γ_0

$$\Gamma_0 = \frac{2buC_L}{\pi \mathit{AR}}. \tag{3.34}$$

The change in angle of attack $\alpha_{j,n}$ can be written as

$$\alpha_n = \frac{w_n}{u} = \frac{C_L}{\pi \mathit{AR}}, \tag{3.35}$$

The wing drag coefficient can be found by multiplying the lift coefficient with the change in angle of attack $w_{j,n}/u$

$$C_{Di,n} \approx \frac{C_L^2}{\pi \mathit{AR}}. \tag{3.36}$$

We then found that the induced drag due to the near wake of a wing with an elliptical lift distribution is similar to the induced drag of the same wing in forward flight.

Similarly, the axial induction due to the near wake a_n is defined as the ratio between the induced velocity from the the near wake and the incoming wind speed

$$a_n = \frac{w_n}{u}\frac{u}{v_w} = \frac{C_L}{\pi \mathit{AR}}\lambda = \frac{C_T}{\lambda}, \tag{3.37}$$

where the wing speed ratio is $\lambda = \frac{u}{v_w}$ and $C_T = \frac{C_L}{\pi \mathit{AR}}\lambda^2$ (Eq. 2.22).

3.3.3 Far wake model

In Sect. 3.3.1, the axial induced velocity produced by a helical vortex filament is modeled as half a vortex ring plus a semi-infinite vortex ring cascade, as in Fig. 3.3b. In Sect. 3.3.2, a near wake model is built based on this idealization, while in this section a far wake model is developed.

In the far wake, the wake is assumed to be already rolled up into two separate vortices, one for each of the wing tips. The velocities induced by the far wake are assumed to be constant over the wing span, therefore they are evaluated at the wing center $R_j = R_0$. The velocity induced by the cascade of vortex rings of intensity Γ on the wing center is

$$w_f \approx -\frac{\Gamma}{4\pi\Delta R}\sum_{k=1}^{\infty}\underbrace{\int_{-\pi}^{\pi}\frac{\eta_0\left(1-\eta_0\right)\left(\cos\theta-\left(1-\eta_0\right)\right)}{\left(1-2\left(1-\eta_0\right)\cos\theta+\left(1-\eta_0\right)^2+\left(\frac{2\pi k}{\lambda_0}\right)^2\right)^{\frac{3}{2}}}d\theta}_{\Upsilon^f_{z,k}}. \tag{3.38}$$

The integral has a closed form solution, so $\Upsilon^f_{z,k}$ takes the form

$$\Upsilon^f_{z,k}(\eta_0,\lambda_0) = \frac{-2\eta_0}{\left(\eta_0^2+\left(\frac{2\pi k}{\lambda_0}\right)^2\right)^{1/2}}\left(K\left(m\right)+\frac{\eta_0(\eta_0-2)-\left(\frac{2\pi k}{\lambda_0}\right)^2}{(\eta_0-2)^2+\left(\frac{2\pi k}{\lambda_0}\right)^2}E\left(m\right)\right), \tag{3.39}$$

with $m = \frac{4(\eta_0-1)}{\eta_0^2+\left(\frac{2\pi k}{\lambda_0}\right)^2}$

The outer and inner trailed vortexes are assumed to be located at $R_f = R_0 \pm y_v$, such that $\Delta R = \mp y_v$ and $\eta_0 = \mp\eta_v = \mp\frac{y_v}{R_0}$, with an intensity of $\Gamma = \pm\Gamma_0$ respectively. The velocity at the wing center induced by the two vortex ring cascades is

$$w_f \approx \frac{\Gamma_0}{4\pi y_v}\left(\sum_{k=1}^{\infty}\Upsilon^f_{z,k}\left(\eta_0 = -\eta_v, \lambda_0\right) + \sum_{k=1}^{\infty}\Upsilon^f_{z,k}\left(\eta_0 = \eta_v, \lambda_0\right)\right). \tag{3.40}$$

The summations can be solved numerically for different values of λ_0 and η_v and its solution fitted as function of these two parameters. The approximated solution of the summation is

$$\sum_{k=1}^{\infty}\left(\Upsilon^f_{z,k}\left(-\eta_v, \lambda_0\right) + \Upsilon^f_{z,k}\left(\eta_v, \lambda_0\right)\right) \approx \frac{9}{2}\eta_v^{\pi/2}\left(\frac{\lambda_0}{2\pi}\right)^{3/2}. \tag{3.41}$$

Figure 3.5 shows the comparison between the solution obtained numerically and the approximation given in Eq. (3.41).

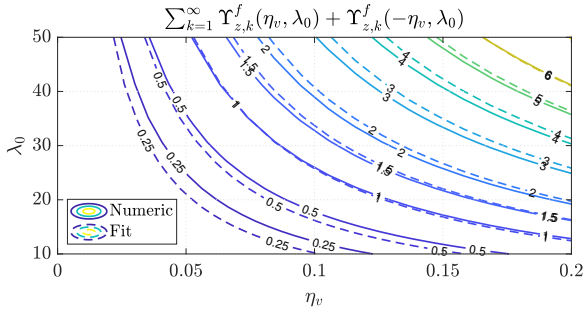

Figure 3.5: *Summation modeling the far wake shape function obtained numerically (-) and fitted function (- -).*

For an elliptical wing, the rolled-up trailed vortices are located approximately at the center of trailed vorticity at $y_v = \frac{\pi}{8}b$ for the outer and inner wing respectively, such that their non-dimensional radial coordinate is $\eta_v = \frac{\pi b}{8R_0} = \frac{\pi}{4}\kappa_0$, where κ_0 is the inverse turning ratio

$$\kappa_0 = \frac{b/2}{R_0}. \tag{3.42}$$

The approximate solution for the induced velocity, using the fitted solution of Eq. (3.41) into Eq. (3.40) and considering $\Gamma_0 = \frac{2buC_L}{\pi\mathcal{AR}}$, is

$$w_f \approx u\frac{C_L}{\pi\mathcal{AR}}\frac{\kappa_0^{\pi/2}}{4\pi}\lambda_0^{3/2}. \tag{3.43}$$

To find the normalized torsional parameter λ_0, we assume that the axial velocity of the vortex filaments is $v_w\left(1 - a_n\right)$, where a_n is the axial induction at the lifting line induced by the near wake (Eq. 3.37). The helix pitch h_0 can be approximated with the distance covered by the vortex filaments moving downwind in the revolution period. The revolution period is the ratio between the circumference length and the windplane tangential velocity $\frac{2\pi R_0}{u}$

$$h_0 = v_w\left(1 - a_n\right)\frac{2\pi R_0}{u} = \frac{2\pi R_0}{\lambda}\left(1 - a_n\right). \tag{3.44}$$

Considering the definition of the normalized torsional parameter $\lambda_0 = \frac{2\pi R_0}{h_0}$ (Eq 3.14), λ_0 can be linked to the the wing speed ratio λ as

$$\lambda_0 = \frac{\lambda}{1-a_n} = \frac{\lambda}{1-\frac{C_L}{\pi \mathcal{AR}}\lambda} = \frac{\lambda^2}{\lambda - C_T}, \tag{3.45}$$

where the axial induction due to the near wake is given in Eq. (3.37) ($a_n = \frac{C_L}{\pi \mathcal{AR}}\lambda = \frac{C_T}{\lambda}$).

This equation links λ_0 (non dimensional torsional parameter of the helicoidal wake) to λ (wing speed ratio) and to either the induced change in angle of attack produced by the near wake $\frac{C_L}{\pi \mathcal{AR}}$ or the thrust coefficient C_T. Substituting the normalized torsional parameter (Eq. 3.45) into Eq. (3.43), the induced velocity due to the far wake is

$$w_f = u\frac{C_L}{\pi \mathcal{AR}}\frac{\kappa_0^{\pi/2}}{4\pi}\frac{\lambda^3}{(\lambda - C_T)^{3/2}}, \tag{3.46}$$

The axial induction due to the far wake a_f can be expressed as a function of the thrust coefficient C_T and the wing speed ratio λ as

$$a_f = \frac{w_f}{v_w} = \frac{C_L}{\pi \mathcal{AR}}\frac{\kappa_0^{\pi/2}}{4\pi}\frac{\lambda^4}{(\lambda - C_T)^{3/2}} = C_T\frac{\kappa_0^{\pi/2}}{4\pi}\frac{\lambda^2}{(\lambda - C_T)^{3/2}}, \tag{3.47}$$

The change in angle of attack due to the far wake can be written as a function of $\frac{C_L}{\pi \mathcal{AR}}$ and λ as

$$\alpha_f = \frac{w_f}{u} = \frac{C_L}{\pi \mathcal{AR}}\frac{\kappa_0^{\pi/2}}{4\pi}\left(\frac{\lambda}{1-\frac{C_L}{\pi \mathcal{AR}}\lambda}\right)^{3/2}, \tag{3.48}$$

where we used the second expression in Eq. (3.45) into Eq. (3.43). In alternative, we can write the change in angle of attack due to the far wake as a function of the thrust coefficient C_T and λ as

$$\alpha_f = \frac{w_f}{u} = \frac{w_f}{v_w}\frac{v_w}{u} = \frac{a_f}{\lambda} = C_T\frac{\kappa_0^{\pi/2}}{4\pi}\frac{\lambda}{(\lambda - C_T)^{3/2}}, \tag{3.49}$$

where a_f is found in Eq. 3.47.

The induced drag coefficient due to the far wake $C_{Di,f}$ can be written as

$$C_{Di,f} = C_L\alpha_f = C_L C_T\frac{\kappa_0^{\pi/2}}{4\pi}\frac{\lambda}{(\lambda - C_T)^{3/2}} = \frac{C_L^2}{\pi \mathcal{AR}}\frac{\kappa_0^{\pi/2}}{4\pi}\left(\frac{\lambda}{1-\frac{C_L}{\pi \mathcal{AR}}\lambda}\right)^{3/2}. \tag{3.50}$$

In Fig. 3.6, two different ways of accounting for the far wake are shown. In Fig. 3.6(a) the effect of the induced velocities is taken into account by including the induction in the velocity triangle, as typically done for wind turbines. If only the induced velocity due the far wake is subtracted to the incoming wind, the induced drag due to near wake should be included in the force balance, as in Fig. 3.6(b).

3.4 Windplane drag coefficient

In this chapter, we characterized the main sources of drag in windplanes. We write the windplane parasite drag coefficient as

$$C_{D,p} = \underbrace{C_{d,0} + k_d C_L^2}_{C_d} + \underbrace{\frac{C_{d,te}}{16} d_{te} l_{te} \mathcal{AR}}_{C_{D,te}} \tag{3.51}$$

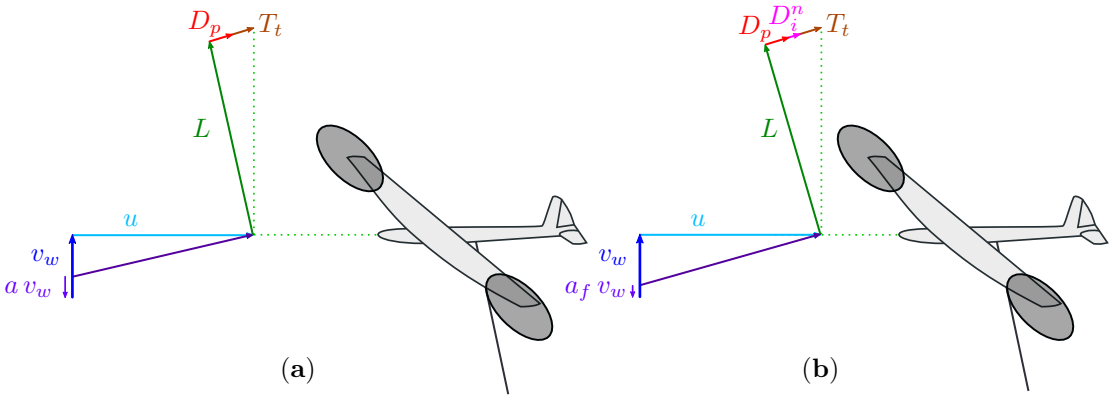

Figure 3.6: *Velocity triangle and force balance if the effect of the induced velocities are taken into account by including the induction in the velocity triangle **(a)** or by reducing the incoming wind with the induction doe to the far wake and including the induced drag due to the near wake in the force balance **(b)**.*

If only the parasite drag coefficient $C_{D,p}$ is included in the drag term (as in Chap. 2), the induction a should be considered in the velocity triangle (Fig. 3.6(a))

$$a = a_n + a_f = \frac{C_T}{\lambda}\left(1 + \frac{\kappa_0^{\pi/2}}{4\pi}\frac{\lambda^3}{(\lambda - C_T)^{3/2}}\right). \tag{3.52}$$

We define the windplane drag coefficient by including the contribution from the near wake as

$$\begin{aligned} C_D &= C_{d,0} + \frac{C_{d,te}}{16} d_{te} l_{te} \mathcal{AR} + k_d C_L^2 + \underbrace{\frac{C_L^2}{\pi \mathcal{AR}}}_{C_{Di}^n} \\ &= \underbrace{C_{d,0} + \frac{C_{d,te}}{16} d_{te} l_{te} \mathcal{AR}}_{C_{D,0}} + \frac{C_L^2}{\pi \mathcal{AR}} \underbrace{(1 + k_d \pi \mathcal{AR})}_{\frac{1}{e}} \end{aligned}, \tag{3.53}$$

where $C_{D,0}$ is the zero-lift drag coefficient of the windplane and the term $\frac{C_L^2}{\pi \mathcal{AR} e}$ is the drag coefficient due to lift, including both induced drag and the part of parasite drag function of lift. The factor e is named the Oswald efficiency (see Sect. 6.7.2 ofAnderson (2017)). The Oswald efficiency (or Oswald factor) typically includes also a contribution from the span-wise efficiency. In this thesis we assumed elliptical wing, which have a unitary span-wise efficiency. If this drag coefficient is used, just the far wake induction a_f should be included in the model (see Fig. 3.6(b))

$$a_f = \frac{\kappa_0^{\pi/2}}{4\pi}\frac{C_T \lambda^2}{(\lambda - C_T)^{3/2}}. \tag{3.54}$$

3.5 Discussion

In this chapter, we characterized the main sources of aerodynamic parasite drag and the aerodynamic induction for windplanes.

We started by approximating the airfoil polars with an analytical expression quadratic on the lift coefficient. When employing this expression in a design framework, we expect the optimizer to design the plane about a specific lift coefficient. By characterizing which design lift coefficient is chosen, we can can understand which type of airfoils are optimal for windplanes. This is investigated in Chap. 4.

We then found an expression for the equivalent tether drag coefficient, as function of the non-dimensional dimensions of the tether, its section drag coefficient and the wing aspect ratio. When employing this expression in a design framework, we expect the optimizer to decrease as much as possible the tether diameter to reduce the equivalent tether drag. The tether section drag coefficient is dependent on the aerodynamic design of the tether.

We finally derived an expression for the velocities induced by the trailed vorticity, which has an helicoidal shape. Under the assumption of steady crosswind operations, the expression for the velocities induced on the lifting line from a helicoidal vortex filament, trailed by a position on the windplane wing, is divided into an expression modeling the near vortex filament and one for the far vortex filament.

The near vortex filament is modeled as the first half rotation of the helicoidal filament, where the axial component of the filament is neglected. The velocity induced by the near vortex filament is expressed in terms of elliptic integrals, and it is linearized to a more intuitive expression. The induced drag coefficient modeling the near wake, built up from the near vortex filaments contributions, is found to be similar to the drag coefficient the same wing would have in forward flight. This suggests that models assuming straight trailed vortex filaments are a good approximation of the near wake only.

The far wake is modeled as two semi-infinite vortex rings cascades with opposite intensity. The related induced velocities depend on the radial position of the rings, which is known, and on the axial distance of the rings, which is unknown. The axial distance of the rings is found by assuming that the vortex filaments move downwind with the velocity of the wind minus the velocity induced by the near wake. The induction due to the far wake is then dependent on the turning radius. When employing this expression in a design framework, we expect the optimizer to increase the turning radius to decrease the induction due to the far wake.

This wake model is validated with the free wake vortex model (Marten et al. (2015)) implemented in Qblade. See Trevisi et al. (2023a) for more details. The main assumptions of this aerodynamic model define its validity range. The model is derived by assuming that the windplane flies steady fully crosswind trajectories with a steady and uniform inflow. The model is then challenged with general trajectories (e.g. with an elevation angle) and with the plane velocity changing over the loop. However, it is reasonable to expect that the plane velocity fluctuations will mainly impact the near wake, while the far wake is manly influenced by average values. The assumption of steady and uniform inflow is also challenged in realistic conditions. Indeed, the windplane will fly in a sheared and turbulent inflow. The wind turbulence will define the wake breakdown and thus influence the wind recovery after the windplane. This effects are relevant when studying the aerodynamic interaction between windplanes. This model can be directly applied to Ground-Gen AWESs (Trevisi et al. (2023a)) and some modifications are required for Rotational AWESs. Rotational AWESs are characterized by multiple wings, thus the aerodynamic interaction among them shall be modeled.

3.6 State of the art and open questions

3.6.1 Tether drag

The effect of tether drag on airborne wind energy is well know in the literature. The formulation presented in this thesis was first derived by Houska and Diehl (2006), used by Fagiano (2009) and Argatov et al. (2009), and later adopted in all low-fidelity works in the field. Trevisi et al. (2020a) develop a more elaborated formulation, resolving the tether displacement, and finding the same final result.

3.6.2 Aerodynamic induction

For wind energy systems, the evaluation of the induced velocities is of extreme importance to properly estimate the power production.

Learning from conventional wind energy, the induced velocities for AWE are estimated in the literature with momentum-based and vortex-based methods. High-fidelity computational fluid dynamics (CFD) methods are typically used to study the wake characteristics and validate lower fidelity models.

Initially, the applicability of momentum methods for AWE was doubted (Loyd (1980); Archer (2013); Costello et al. (2015)), as the definition of swept area is not settled, but by intuition way larger than the windplane wing. Recently, however, momentum methods have been developed for AWE, with De Lellis et al. (2018) and Kheiri et al. (2018, 2019) independently generalizing momentum theory to compute the induced velocity. This is derived by equating the aerodynamic lift of the windplane to the thrust applied to the annulus swept by the wing, with the momentum formulation.

Gaunaa et al. (2020) point out that using momentum theory to evaluate the induction of an windplane, which is described by 3D polars, is not physically consistent. Momentum theory is indeed used in wind turbine aerodynamics to compute the local velocity triangle of the airfoil (2D polars) in the wind turbine blade. If the windplane is described by 3D polars (i.e. the drag coefficient is including the induced drag coefficient that the windplane would have in a forward flight) in the momentum formulation, then a part of the wake would be counted twice. If, instead, momentum theory is used to evaluate the velocity triangle of an airfoil (2D polars) in the windplane wing, then a root and a tip correction would be needed to take into account that the rotor is not a disc built up of an infinite number of wings, but one single wing. The root and tip corrections for windplanes would however differ largely from conventional wind turbines corrections, as these are developed for blades extending almost to the rotation axis, and need a re-work. Gaunaa et al. (2020) then build a vortex-based engineering model, which is physically consistent and it is tuned with CFD simulations. Based on these considerations, Trevisi et al. (2023a) (Please see the corrigendum at `https://doi.org/10.5194/wes-8-999-2023-corrigendum`) find an induced drag coefficient of the windplane with vortex methods. The derivation by Trevisi et al. (2023a) is more general than the one presented here, as that formulation allows the evaluation of the induction in the neighborhood of the lifting line (and not strictly on the lifting line). The model is validated with the the lifting line free vortex wake method (Marten et al. (2015)) implemented in QBlade. Another vortex method, based on the vortex tube model, is developed by Leuthold et al. (2019) for an AWE

system composed of more wings flying in the same annulus to compute the induction at the windplanes middle-span. This model takes as inputs the system thrust coefficient, relative radius and reel-out factor.

As the field counts a limited number of prototypes with limited number of flying hours, the benchmark of engineering models is typically done with higher fidelity codes, instead of experiments. For aerodynamic models, CFD studies then represent the reference. Haas and Meyers (2017) describe the wake characteristics for a given aircraft in Fly-Gen and Ground-Gen circular path with a LES setup. Aerodynamic forces, applied with an actuator line technique, are computed to impose an induction of $1/3$ at the kite location. Haas et al. (2019b) further develop the same LES framework by including an optimal control problem for Ground-Gen AWES in non-turbulent and turbulent sheared inflow conditions. Mehr et al. (2020) investigate the aerodynamic interaction of the onboard wind turbines with the main wing in a crosswind circular maneuver with a viscous vortex particle method. The main wing wake is however removed one span downstream from the trailing edge, not resolving the helicoidal wake. Branlard et al. (2022) extend the AeroDyn module of OpenFAST through the open source lifting line vortex code OLAF to support arbitrary collections of wings, rotors and towers. Complex geometries, such as windplanes, can then be handled by OLAF.

There are a number of open research questions related to the aerodynamic induction modeling. We list some here

- The windplane with ground station at the ground level (configuration (e), Fig. 1.1) operates with an elevation angle. How is the aerodynamic induction influenced by the elevation angle?
- Are the onboard wind turbines influencing the aerodynamic wake structure?
- Are elliptic wings minimizing the induced drag for windplanes?

CHAPTER 4

Windplane conceptual design

In this chapter, we look for a periodic approximate solution of the equations of motion. The periodicity is driven by the gravity and the periodic control inputs. We formulate an optimal control problem, where the optimizer modifies the control variables to maximize the mean power. We then upgrade it to an optimal design problem, where the optimizer modifies the control variables and the design variables to maximize the mean power. Finally, we analyze the optimal designs and their optimal control.

4.1 Equations of motion

We recall the equations of motion in the cylindrical reference frame given in Eq. (2.5)

$$\begin{cases} m\dot{u} + 2m\dot{r}u = F_{a,1} + mg\cos\Psi \\ m\ddot{r} - m\frac{u^2}{r} = F_{a,2} - T\tan\Phi - mg\sin\Psi \\ m\ddot{z} = F_{a,3} + T \end{cases}$$

where $\boldsymbol{F}_a$ is the aerodynamic force and T is the axial component of the tensile force acting on the tether (Eq. 2.3). In this chapter, we assume a circular trajectory, so that r and z are constant and the motion is allowed only in the tangential direction.

The equations of motion thus become one differential equation (the tangential equation of motion) and two algebraic equations (radial and axial equilibria)

$$\begin{cases} m\dot{u} = F_{a,1} + mg\cos\Psi \\ m\frac{u^2}{R_0} = T\tan\Phi + mg\sin\Psi - F_{a,2} \\ T = -F_{a,3} \end{cases} \tag{4.1}$$

Similar to what assumed in the Chapter 2, we model the aerodynamic forces as

$$\boldsymbol{F}_a = \begin{bmatrix} L\sin\gamma - (D_p + T_t)\cos\gamma \\ (L\cos\gamma + (D_p + T_t)\sin\gamma)\phi \\ -(L\cos\gamma + (D_p + T_t)\sin\gamma) \end{bmatrix} \approx \begin{bmatrix} \frac{L}{\lambda}(1-a) - (D_p + T_t) \\ \phi L \\ -L \end{bmatrix}, \tag{4.2}$$

where ϕ is named the roll angle. The equations of motion then are

$$\begin{cases} m\dot{u} = \frac{L}{\lambda}(1-a) - (D_p + T_t) + mg\cos\Psi \\ m\frac{u^2}{R_0} = T\tan\Phi + mg\sin\Psi - \phi L \\ T = L \end{cases} \tag{4.3}$$

By substituting the third equation into the second, we find an algebraic equation for the roll angle ϕ

$$\phi = \tan\Phi - \frac{m}{L}\frac{u^2}{R_0} + \frac{mg}{L}\sin\Psi. \tag{4.4}$$

This equation defines the roll angle necessary to keep the windplane in the circular trajectory.

We now insert the lift force definition $L \approx \frac{1}{2}\rho C_L \frac{b^2}{AR}u^2$ into the expression for the opening angle Φ that we found for the steady-state (Eq. 2.10)

$$\tan\Phi = \frac{m}{L}\frac{u^2}{R_0} = \frac{m}{\frac{1}{2}\rho A C_L R_0}, \tag{4.5}$$

finding that the opening angle Φ does not depend on the tangential velocity because both the centrifugal forces and aerodynamic forces scale with the tangential velocity squared. By expressing the turning radius as $R_0 = L_{te}\sin\Phi$ (Eq. 2.1), we find an equation for the opening angle Φ

$$\sin\Phi\tan\Phi = M = \frac{m}{\frac{1}{2}\rho A C_L L_{te}} = 4\frac{\mu AR}{C_L l_{te}}, \tag{4.6}$$

where μ is the non-dimensional mass

$$\mu = \frac{m}{\rho b^3}, \tag{4.7}$$

and $l_{te} = \frac{L_{te}}{b/2}$ (Eq. 3.8). Eq. (4.6) can be expressed to explicit Φ as

$$\Phi = \arccos\left(-\frac{M}{2} + \frac{\sqrt{M^2+4}}{2}\right). \tag{4.8}$$

Substituting the expression of the steady-state opening angle (Eq. 4.5) into Eq. (4.4), we find that the roll angle is just used to compensate the radial component of gravity

$$\phi = \frac{mg}{L}\sin\Psi, \tag{4.9}$$

so that lift is not used to turn, but just to stay airborne. A graphical representation of the radial force balance is given in Fig. 4.1.

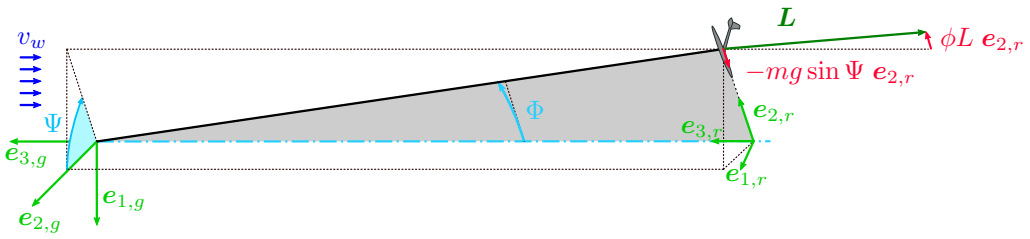

Figure 4.1: *Radial force balance.*

4.2 Periodic solution of the tangential equation of motion

The equation of motion along the tangential direction (first equation in 4.3) can be written as

$$m\dot{u} = \underbrace{\frac{1}{2}\rho A C_L u v_w (1-a)}_{\text{propulsive lift}} - \underbrace{\frac{1}{2}\rho A C_{D,p} u^2}_{\text{parasite drag}} - \underbrace{\frac{1}{2}\rho A_t C_{T,t} u^2}_{\text{turbines thrust}} + \underbrace{mg\cos\Psi}_{\text{gravity}}. \tag{4.10}$$

We model the induction as (Eq. (3.52))

$$a = a_n + a_f = \frac{C_L}{\pi AR}\lambda + \frac{\kappa_0^{\pi/2}}{4\pi}\frac{\hat{C}_T\hat{\lambda}^2}{(\hat{\lambda}-\hat{C}_T)^{3/2}}, \tag{4.11}$$

where the induction due to the far wake is assumed to be function of the mean quantities over the loop. Indeed, the model of the aerodynamic induction in Chap. 3 is derived assuming a constant tangential velocity and we expect the far wake to be mostly influenced by average values over the loop.

The tangential equation of motion (Eq. 4.10) can also be written as (see Fig. 3.6)

$$m\dot{u} = \underbrace{\frac{1}{2}\rho A C_L u v_w (1-a_f)}_{\text{propulsive lift}} - \underbrace{\frac{1}{2}\rho A (C_{D,p} + C_{Di}^n) u^2}_{\text{drag}} - \underbrace{\frac{1}{2}\rho A_t C_{T,t} u^2}_{\text{turbines thrust}} + \underbrace{mg\cos\Psi}_{\text{gravity}}. \tag{4.12}$$

Normalizing the equation of motion in Eq. (4.12) with $\frac{\mathbb{P}}{v_w} = \frac{1}{2}\rho\pi b^2 v_w^2$, similarly to what done for the thrust coefficient definition (Eq. 2.20), and expressing the onboard wind turbines area as $A_t = \frac{\pi\xi_t^2}{2}b^2$ (Eq. 2.13), the non-dimensional tangential equation of motion h_τ is

$$h_\tau(t) = \frac{C_L}{\pi AR}\lambda(1-a_f) - \frac{C_D}{\pi AR}\lambda^2 - \frac{\xi_t^2}{2}C_{T,t}\lambda^2 + \frac{2}{\pi}\mu\frac{bg}{v_w^2}\cos\Psi - \frac{2}{\pi}\mu\frac{b}{v_w}\dot{\lambda} = 0. \tag{4.13}$$

where $C_D = C_{D,p} + C_{Di}^n$ (Eq. (3.53)).

Since the dynamic problem is periodic, we look for a periodic solution of $h_\tau(t)$. We therefore expand $h_\tau(t)$ as a Fourier series of the azimuth position $\Psi(t)$

$$h_\tau(t) = \tilde{h}_\tau + \sum_{k=1}^{\infty} H_{\tau,s,k}\sin(k\Psi(t)) + H_{\tau,c}\cos(k\Psi(t)) = 0. \tag{4.14}$$

where the coefficients are

$$\begin{aligned}
\tilde{h}_\tau &= \tfrac{1}{2\pi}\int_0^{2\pi} h_\tau(\Psi)d\Psi = 0 \\
H_{\tau,s,k} &= \tfrac{1}{\pi}\int_0^{2\pi} h_\tau(\Psi)\sin(k\Psi)\,d\Psi = 0 \quad \text{for } k \geq 1 \\
H_{\tau,c,k} &= \tfrac{1}{\pi}\int_0^{2\pi} h_\tau(\Psi)\cos(k\Psi)\,d\Psi = 0 \quad \text{for } k \geq 1,
\end{aligned} \tag{4.15}$$

For the tangential equation of motion to be fulfilled $h_\tau(t) = 0$, all its Fourier coefficients have to be null.

We can now expand also the wing speed ratio as a Fourier series

$$\begin{aligned}
\lambda(\Psi(t)) = \tilde{\lambda} + \sum_{k=1}^{\infty} \Lambda_{s,k}\sin(k\Psi(t)) + \Lambda_{c,k}\cos(k\Psi(t)) \\
\tilde{\lambda}\left(1 + \sum_{k=1}^{\infty} \tilde{\Lambda}_{s,k}\sin(k\Psi(t)) + \tilde{\Lambda}_{c,k}\cos(k\Psi(t))\right),
\end{aligned} \tag{4.16}$$

where the coefficients $\mathbf{\Lambda} = [\tilde{\lambda}, \Lambda_{s,1}, \Lambda_{s,2}, ..., \Lambda_{c,1}, \Lambda_{c,2}, ...]$ are set to fulfill the equation of motion (Eq. 4.15).

To write the acceleration term as a function of $\mathbf{\Lambda}$, we write the time derivative of the azimuth position Ψ as a function of λ as

$$\dot{\Psi} = \frac{d\Psi}{dt} = -\frac{u}{R_0} = -2\lambda\kappa_0\frac{v_w}{b}. \tag{4.17}$$

The time derivative of the wing speed ratio is

$$\begin{aligned}
\dot{\lambda}(\Psi(t)) &= \dot{\Psi}(t)\sum_{k=1}^{\infty} k\left(\Lambda_{s,k}\cos(k\Psi(t)) - \Lambda_{c,k}\sin(k\Psi(t))\right) \\
&= -2\lambda\kappa_0\frac{v_w}{b}\sum_{k=1}^{\infty} k\left(\Lambda_{s,k}\cos(k\Psi(t)) - \Lambda_{c,k}\sin(k\Psi(t))\right).
\end{aligned} \tag{4.18}$$

We can now write the $\tilde{h}_\tau$ equation (Eq. 4.15) as

$$\tilde{h}_\tau = \frac{1}{2\pi}\int_0^{2\pi}\left(\frac{C_L}{\pi AR}\lambda\left(1 - a_f\right) - \frac{C_D}{\pi AR}\lambda^2 - \frac{\xi_t^2}{2}C_{T,t}\lambda^2\right)d\Psi = 0, \tag{4.19}$$

where the terms related to gravity and to the acceleration are null.

The $H_{\tau,c,1}$ equation can be written as

$$\begin{aligned}
H_{\tau,c,1} &= \frac{1}{2\pi}\int_0^{2\pi}\left(\frac{C_L}{\pi AR}\lambda\left(1 - a_f\right) - \frac{C_D}{\pi AR}\lambda^2 - \frac{\xi_t^2}{2}C_{T,t}\lambda^2 + \frac{2\mu}{\pi}\frac{bg}{v_w^2}c_\Psi - \frac{2}{\pi}\mu\frac{b}{v_w}\dot{\lambda}\right)c_\Psi d\Psi \\
&= \frac{\mu}{\pi}\left(\frac{bg}{v_w^2} + 2\kappa_0\tilde{\lambda}\Lambda_{s,1}\right) + \frac{1}{2\pi}\int_0^{2\pi}\left(\frac{C_L}{\pi AR}\lambda\left(1 - a_f\right) - \frac{C_D}{\pi AR}\lambda^2 - \frac{\xi_t^2}{2}C_{T,t}\lambda^2\right)c_\Psi d\Psi = 0.
\end{aligned} \tag{4.20}$$

The other coefficients in Eqs. 4.15 can be found by applying the definition. We then wrote the nonlinear differential equation of motion as a set of algebraic equations. Among these algebraic equations, the $H_{\tau,c,1}$ (Eq. 4.20) is the only one where the periodic external input (i.e. gravity) appears. This method of solving a partial differential equation, which accept periodic solution, is named *harmonic balance* in the literature and it is detailed in Sect. 7.1.

4.3 Fundamental frequency

We want now to further characterize the periodic solution by finding the fundamental frequency. The time at the angular position Ψ is

$$t = \int_0^t d\tilde{t} = -\int_0^{\Psi} \frac{R_0}{\lambda v_w} d\tilde{\Psi}, \tag{4.21}$$

where $d\tilde{t} = -\frac{R_0}{\lambda v_w} d\tilde{\Psi}$ (Eq. 4.17). The revolution period $\mathcal{T}$ is

$$\begin{aligned}
\mathcal{T} &= -\frac{R_0}{\tilde{\lambda} v_w} \int_0^{-2\pi} \frac{1}{1 + \sum_{k=1}^{\infty} \left(\tilde{\Lambda}_{s,k} s_{(k\Psi)} + \tilde{\Lambda}_{c,k} c_{(k\Psi)} \right)} d\Psi \\
&\approx -\frac{R_0}{\tilde{\lambda} v_w} \int_0^{-2\pi} 1 + \left(\sum_{k=1}^{\infty} \tilde{\Lambda}_{s,k} s_{(k\Psi)} + \tilde{\Lambda}_{c,k} c_{(k\Psi)} \right)^2 + O\left(\left(\sum_{k=1}^{\infty} \tilde{\Lambda}_{s,k} s_{(k\Psi)} + \tilde{\Lambda}_{c,k} c_{(k\Psi)} \right)^4 \right) d\Psi \\
&\approx \frac{2\pi R_0}{\tilde{\lambda} v_w} \left(1 + \frac{1}{2} \sum_{k=1}^{\infty} \left(\tilde{\Lambda}_{s,k}^2 + \tilde{\Lambda}_{c,k}^2 \right) \right).
\end{aligned} \tag{4.22}$$

We can now write the fundamental frequency

$$\omega = \frac{2\pi}{\mathcal{T}} = \hat{\lambda} \frac{v_w}{R_0} \approx \frac{\tilde{\lambda}}{1 + \frac{1}{2} \sum_{k=1}^{\infty} \left(\tilde{\Lambda}_{s,k}^2 + \tilde{\Lambda}_{c,k}^2 \right)} \frac{v_w}{R_0}, \tag{4.23}$$

where $\hat{\lambda}$ is the mean value in time of the wing speed ratio over one revolution

$$\hat{\lambda} = \frac{\tilde{\lambda}}{1 + \frac{1}{2} \sum_{k=1}^{\infty} \left(\tilde{\Lambda}_{s,k}^2 + \tilde{\Lambda}_{c,k}^2 \right)}. \tag{4.24}$$

We then found that the mean wing speed ratio in time $\hat{\lambda}$ is equal to the mean wing speed ratio in azimuth $\tilde{\lambda}$ divided by a term function of the wing speed ratio fluctuations squared.

4.4 Power balance

To better understand results, we derive the power balance equation by multiplying the equation of motion in Eq. (4.10) with the tangential velocity u

$$\frac{1}{2} \rho A C_L v_w u^2 (1 - a) - \frac{1}{2} \rho A C_{D,p} u^3 - \frac{1}{2} \rho A_t C_{T,t} u^3 + mg \cos \Psi u = miu, \tag{4.25}$$

where the first term is the aerodynamic power due to propulsive lift, the second the aerodynamic power dissipated in parasite drag, the third is the onboard turbines thrust power, the fourth is the gravitational power and the right-hand-side is the variation of kinetic energy. We can normalize Eq. (4.25) with $\mathbb{P} = \frac{1}{2} \rho \pi b^2 v_w^3$, similar to what done for the power coefficient definition, to get to a non dimensional version of the power

balance equation

$$\underbrace{\frac{C_L}{\pi AR}\lambda^2(1-a)}_{C_T} - \underbrace{\frac{C_{D,p}}{\pi AR}\lambda^3}_{C_\tau} - \underbrace{\frac{\xi_t^2}{2}C_{T,t}\lambda^3}_{\frac{C_{T,t}}{C_{P,t}}C_P} + \underbrace{\frac{2}{\pi}\mu\frac{bg}{v_w^2}\lambda\cos\Psi}_{C_g} = \underbrace{\frac{2}{\pi}\mu\frac{b}{v_w}\dot{\lambda}\lambda}_{\frac{\partial e_k}{\partial t}}, \tag{4.26}$$

which can be written in compact form as

$$\underbrace{C_T(1-a) - C_\tau}_{C_a} + C_g = \frac{C_P}{(1-a_t)} + \frac{\partial e_k}{\partial t}. \tag{4.27}$$

The mean value of the power balance equation over the loop is

$$\underbrace{\frac{1}{\mathcal{T}}\int_0^{\mathcal{T}} \left(C_T(1-a) - C_\tau\right) dt}_{\hat{C}_a} = \frac{1}{\mathcal{T}}\int_0^{\mathcal{T}} \frac{C_P}{(1-a_t)} dt, \tag{4.28}$$

where the integrals of the gravitational energy C_g and of the change of $\frac{\partial e_k}{\partial t}$ over the period are null. This equation then represents the balance between the mean aerodynamic power and the mean turbines' thrust power over the period.

The mean aerodynamic power can be also written as

$$\hat{C}_a = \frac{1}{\mathcal{T}}\int_0^{\mathcal{T}} \left(a_n(1-a)\lambda - \frac{C_{D,p}}{\pi AR}\lambda^3\right) dt, \tag{4.29}$$

where $a_n = \frac{C_T}{\lambda}$ (Eq. 3.37).

4.5 Power coefficient

The mean value of the power coefficient in time $\hat{C}_P$ is

$$\hat{C}_P = \frac{\xi_t^2}{2}\frac{1}{\mathcal{T}}\int_0^{\mathcal{T}} C_{P,t}\lambda^3 dt = \frac{\xi_t^2}{2}\hat{\lambda}\frac{1}{2\pi}\int_0^{2\pi} C_{P,t}\lambda^2 d\Psi \tag{4.30}$$

where $dt = -\frac{R_0}{\lambda v_w}d\Psi$ and $\mathcal{T} = \frac{2\pi R_0}{\hat{\lambda} v_w}$.

Using the Fourier expansion of λ in Eq. (4.16), the power coefficient is

$$\hat{C}_P = \frac{\xi_t^2}{2}\hat{\lambda}\tilde{\lambda}^2\frac{1}{2\pi}\int_0^{2\pi} C_{P,t}\left(1 + \sum_{k=1}^{\infty}\tilde{\Lambda}_{s,k}s_{(k\Psi)} + \tilde{\Lambda}_{c,k}c_{(k\Psi)}\right)^2 d\Psi. \tag{4.31}$$

4.6 Optimal control problem (OCP)

We now formulate an optimal control problem (OCP) with the model just introduced. The independent variables are the variables that determine the OCP and are fixed. The control variables are the variables modified by the optimizer to maximize the objective

function. The dependent variables are the variables which solve the equality constraints for the given control variables. The optimal control problem reads

$$\begin{aligned} \text{maximize: } & \hat{C}_P(\overbrace{a_f, \mathbf{\Lambda}}^{\text{dependent vars}}, \overbrace{C_L(\Psi), a_t(\Psi)}^{\text{control variables}}, \overbrace{AR, \mu, d_{te}, b, v_w, \xi_t, C_{d,0}, k_d, C_{d,te}, l_{te}, \overline{\sigma}_{te}}^{\text{independent variables}}) \\ \text{subject to: } & [h_{a_f}; \boldsymbol{H}] = \mathbf{0} \quad \text{equality constraint} \\ & c_{P_r} < 0 \quad \text{inequality constraint,} \end{aligned} \tag{4.32}$$

which is equivalent to look for the lift coefficient C_L and the onboard wind turbines induction a_t which maximize the mean value of the power coefficient for the given independent variables. Note that the denominator in the power coefficient definition is just function of independent variables, so that optimizing for the mean power coefficient is equivalent to optimizing for the mean power. The inequality constraint c_{P_r} limits the mean generated power to the rated power of the generators.

A reminder of the physical interpretation of the independent variables is given in Table 4.2. The air density ρ and the gravitational acceleration g are not listed among the independent variables in OCP (4.32) because they can be considered fixed for wind energy systems on planet Earth at this stage of development. We take $\rho = 1.225$ kg/m^3 and $g = 9.81$ m/s^2.

We want to upgrade this optimal control problem to an optimal design problem. To do this, we need a model for the tether design.

4.7 Tether design

The tether is typically designed for ultimate strength and to survive a given period of operations. Bosman et al. (2013) describe the tether types for airborne wind energy and highlight the creep phenomenon as the main driver determining the tether life. They provide the safe working life curve $\mathcal{L}_{te}$, showing the estimated life of the tether if only one stress level is applied. In Figure 4.2 this curve for a DM20 Dyneema tether is shown. The safe working life curve $\mathcal{L}_{te}$ can be approximated with

$$\mathcal{L}_{te}(\sigma_{te}) = 10\hat{}\left(c_{te,0} + c_{te,1}\sigma_{te} + c_{te,2}\sigma_{te}^2 + c_{te,3}\sigma_{te}^3\right) \tag{4.33}$$

where σ_{te} is in GPa and the parameters are estimated by fitting the DM20 data in Fig. 33.16 from Bosman et al. (2013) and reported in Table 4.1.

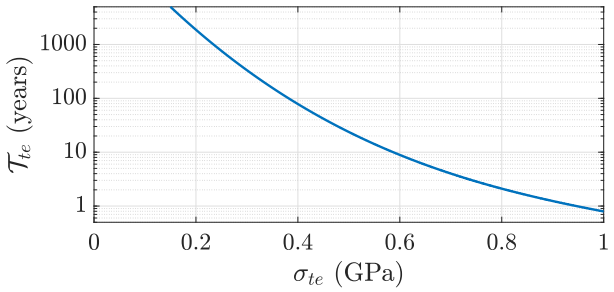

Figure 4.2: *Safe working life (T= 20C) graphs for DM20 Dyneema fibers based on creep rupture (Bosman et al. (2013)).*

Table 4.1: *Safe working life (T= 20C) parameters for DM20 Dyneema fibers based on creep rupture.*

$c_{te,0} = 5.2$	$c_{te,1} = -11.2$	$c_{te,2} = 8.3$	$c_{te,3} = -2.4$

Bosman et al. (2013) suggest the use of the Miner's rule for the estimation of tether life $\mathcal{T}_{te}$

$$\mathcal{T}_{te} \int_{v_{w,\text{in}}}^{v_{w,\text{out}}} \frac{W\left(v_w\right)}{\mathcal{L}_{te}\left(\hat{\sigma}_{te}\left(v_w\right)\right)} dv_w = 1, \tag{4.34}$$

where $W\left(v_w\right)$ is the wind distribution (e.g. Weibull), $\hat{\sigma}_{te}(v_w)$ is the mean tether stress applied as a function of wind speed and $\mathcal{T}_{te}$ in measured in years. In this thesis, we assume a Weibull wind distrubution function

$$W\left(v_w\right) = \frac{k}{A}\left(\frac{v_w}{A}\right)^{k-1} e^{-\left(\frac{v_w}{A}\right)^k}, \tag{4.35}$$

where we take $A = 8$ m/s and $k = 2$.

This design methodology shall be considered when designing for the whole wind speed range. In this thesis, we design for one single wind speed to simplify the results and their understanding. Therefore, we design the tether based on a representative tether strength. We can however use Eq. (4.34) to estimate the life of the tether when studying how the design performs as a function of wind speed.

The tether is designed according to the inequality constraint c_σ

$$c_\sigma(v_w) = \hat{\sigma}_{te}(v_w) - \overline{\sigma}_{te} < 0, \tag{4.36}$$

where $\overline{\sigma}_{te}$ is the representative tether strength. In this work, we take $\overline{\sigma}_{te} = 600$ MPa. Note that the electrical component of the tether (needed to transmit the electrical power to the ground station) is not modeled.

To derive an expression for the mean tether stress, we first write the mean force acting on the tether

$$\begin{aligned} T_{te}(t) &\approx L(t)\sqrt{1+\tan\Phi^2} = \frac{1}{2}\rho\frac{b^2}{AR}\sqrt{1+\tan\Phi^2}v_w^2 C_L(t)\lambda(t)^2 \\ &= \frac{1}{2}\rho\pi b^2\sqrt{1+\tan\Phi^2}v_w^2 C_T(t), \end{aligned} \tag{4.37}$$

where C_T is the thrust coefficient. Writing the tether diameter as D_{te}, the mean stress acting on the tether $\hat{\sigma}_{te}$ is

$$\hat{\sigma}_{te} = \frac{\hat{T}_{te}}{\pi D_{te}^2/4} = 8\rho v_w^2 \frac{\hat{C}_T}{d_{te}^2}\sqrt{1+\tan\Phi^2}, \tag{4.38}$$

where d_{te} is the tether diameter ratio, defined as the ratio between the tether diameter and the semi-span of the plane $d_{te} = \frac{D_{te}}{b/2}$ (Eq. 3.7).

4.8 Optimal design problem (ODP)

We now upgrade the OCP (4.32) to an optimal design problem ODP. We consider the aspect ratio AR, the non-dimensional mass parameter μ and the tether diameter ratio

d_{te} as design variables and not any more as independent variables. The design problem reads

$$\begin{aligned} &\text{maximize: } \hat{C}_P(\overbrace{a_f, \boldsymbol{\Lambda}}^{\text{dependent vars}}, \overbrace{C_L(\Psi), a_t(\Psi), AR, \mu, d_{te}}^{\text{design variables}}, \overbrace{b, v_w, \xi_t, C_{d,0}, k_d, C_{d,te}, l_{te}, \overline{\sigma}_{te}}^{\text{independent variables}}) \\ &\text{subject to: } [h_{a_f}; \boldsymbol{H}] = \mathbf{0} \quad \text{equality constraint} \\ &\qquad\qquad c_\sigma < 0 \quad \text{inequality constraint,} \end{aligned} \tag{4.39}$$

which is equivalent to look for the lift coefficient C_L, the mean turbines induction a_t, the aspect ratio AR, the non-dimensional mass parameter μ and the tether diameter ratio d_{te} which maximize the mean power for the given independent variables. Note that the inequality constraint on the rated power has been removed in the optimal design problem formulation. The inequality constraint defines the tether diameter.

In this work, we model the lift coefficient with two harmonics as

$$C_L(\Psi) = \tilde{C}_L + A_{C_L,s,1} \sin\Psi + A_{C_L,c,1} \cos\Psi + A_{C_L,s,2} \sin(2\Psi) + A_{C_L,c,2} \cos(2\Psi), \tag{4.40}$$

and the onboard turbines' induction with one harmonic as

$$a_t(\Psi) = \tilde{a}_t + A_{a_t,s} \sin\Psi + A_{a_t,c} \cos\Psi. \tag{4.41}$$

4.9 Optimal designs

A realistic windplane design is carried out accounting for the power generated in a range of wind speeds. The design of a wind energy system is typically determined to maximize an economic or a performance metric. A key performance indicator is the capacity factor, measuring how much energy is produced by the system compared with its rated power. Windplanes are expected to reach higher capacity factors than conventional turbines because of the lower CapEx, thus they have lower rated wind speed. Wind turbines typically reach rated power at ≈ 10 m/s.

We chose here to design the windplane and the tether, which is the component transmitting the aerodynamic thrust to the ground, at a wind velocity representative of the rated wind speed for windplanes $v_w = 7$ m/s.

The design is then carried out at a wind speed of $v_w = 7$ m/s and for the independent variables in Table 4.2. The tether drag coefficient is taken as $C_{d,te} = 0.8$, which is representative of a cylindrical tether section. The design tether material strength $\overline{\sigma}_{te}$ is used to size the tether diameter, according to the design methodology illustrated in Sect. 4.7. We consider the order of the Fourier series for the equation of motion $h_\tau(t)$ in Eq. 4.14 and of the wing speed ratio $\lambda(t)$ in Eq. 4.16 to be $k = 5$.

We solve three optimal design problems (ODP) of incremental complexity to better understand the results. The optimal designs are detailed in Table 4.3. The first optimal design problem, denoted with PM_S (Point mass steady), is solved by setting gravity to zero, then looking for steady solutions, and for a constant nondimensional mass parameter $\mu = 0.1$. This is purely an aerodynamic design problem. The second optimal design problem, denoted with PM_L (Point mass light), is solved by including gravity and keeping the nondimensional mass parameter constant to $\mu = 0.1$. The third optimal design problem, denoted with PM_H (Point mass heavy), is solved by considering the full design problem.

Table 4.2: *Values and description of the independent variables for the optimal design problems.*

		units	Description
b	10	m	Wing span
v_w	7	m/s	Wind velocity
ξ_t	0.15	-	Non dimensional onboard wind turbines radius
$C_{d,0}$	0.004	-	Airfoil polar parameters (Eq. 3.2)
k_d	0.008	-	
$C_{d,te}$	0.8	-	Tether drag coefficient
l_{te}	20	-	Tether length ratio
$\overline{\sigma}_{te}$	600	MPa	Design tether material strength

The power coefficient for the first two design problems is $\hat{C}_P = 1.12$ and the designs almost identical. The dynamic is then not influencing the aerodynamic design problem if the mass is kept fixed. When including the nondimensional mass among the design variables, the power coefficient improves and the optimal design slightly changes.

The design lift coefficient is found to be $\hat{C}_L \approx 0.70$ for all designs, corresponding to the maximum lift-to-drag ratio of the airfoil. We then need to use airfoils designed to maximize the lift to drag ratio. These airfoils are well-known as they are used for wind turbines, gliders, aircraft designed to have efficient long cruise, and other applications. The windplane drag coefficient at zero lift is dominated by the equivalent tether drag coefficient.

The optimal aspect ratios are finite and have low values. Low aspect ratio designs are easier to be manufactured and meet the weight requirements.

The non-dimensional mass μ for the third optimization is among the design variables and its optimal value is finite. Depending on the independent variables, extremely light designs might be not required and the optimal mass might be obtained with cheap and sustainable materials.

We try to give a physical interpretation of these results in this section.

Table 4.3: *Optimal designs ODs for the three optimal design problems ODPs.*

PM$_S$ (steady)	$\hat{C}_P = 1.12$	$\hat{C}_T = 2.96$	$\hat{C}_L = 0.70$	$C_{D,0} = 0.014$	$C_{D,te} = 0.010$
$(AR, d_{te}) \subset \boldsymbol{dv}$	$AR = 6.0$	$e = 0.87$	$\mu = 0.1$	$m = 122$ kg	$d_{te} = 1.6$ mm/m
$g = 0$ m/s^2	$\kappa_0 = 0.13$	$a_f = 0.05$	$\hat{\lambda} = 8.87$	$\hat{P} = 74.2$ kW	$\mathcal{T} = 4.0$ s
PM$_L$ (light)	$\hat{C}_P = 1.12$	$\hat{C}_T = 2.96$	$\hat{C}_L = 0.71$	$C_{D,0} = 0.014$	$C_{D,te} = 0.010$
$(AR, d_{te}) \subset \boldsymbol{dv}$	$AR = 6.0$	$e = 0.87$	$\mu = 0.1$	$m = 122$ kg	$d_{te} = 1.6$ mm/m
	$\kappa_0 = 0.13$	$a_f = 0.05$	$\hat{\lambda} = 8.86$	$\hat{P} = 73.8$ kW	$\mathcal{T} = 4.0$ s
PM$_H$ (heavy)	$\hat{C}_P = 1.16$	$\hat{C}_T = 3.27$	$\hat{C}_L = 0.73$	$C_{D,0} = 0.014$	$C_{D,te} = 0.010$
$(AR, d_{te}, \mu) \subset \boldsymbol{dv}$	$AR = 5.3$	$e = 0.88$	$\mu = 0.32$	$m = 390$ kg	$d_{te} = 1.8$ mm/m
	$\kappa_0 = 0.08$	$a_f = 0.03$	$\hat{\lambda} = 8.71$	$\hat{P} = 77.1$ kW	$\mathcal{T} = 6.3$ s

The wing speed ratio λ as function of the non-dimensional time $t/\mathcal{T}$ is shown in Fig. 4.3a for the three ODPs. The initial time corresponds to the position $\Psi = 0$, with the plane moving downwards and thus accelerating ($\dot{\Psi} < 0$, see Fig. 4.1).

The roll angle, necessary to fulfill the radial equation of motion and maintain the circular trajectory, is shown in Fig. 4.3b. When the plane approaches the top part of the loop, its velocity is the lowest. To compensate the radial component of gravity (Eq.

4.9), the roll angle then has the largest value in the top part.

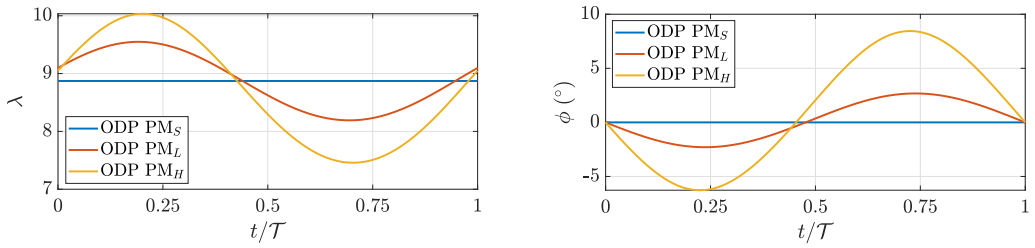

(a) *Wing speed ratio λ as function of non-dimensional time $t/\mathcal{T}$ for the three ODPs.*

(b) *Roll angle ϕ (Eq. 4.9) as function of non-dimensional time $t/\mathcal{T}$ for the three ODPs.*

Figure 4.3

The onboard turbines induction a_t, the thrust coefficient $C_{T,t}$ and the power coefficient $C_{P,t}$ are shown as function of non-dimensional time $t/\mathcal{T}$ in Fig. 4.4a.

In Fig. 4.4b, the lift coefficient as a function of the non-dimensional time is shown. The lift coefficient decreases when the plane moves downwards, and it is in phase with the wing speed ratio (Fig. 4.3a).

Gravity can be compensated by controlling the lift coefficient and the axial induction of the onboard turbines. Gravity has its largest value in the tangential equation of motion at $\Psi = 0$ ($t = 0$) and at $\Psi = \pi$. The lift coefficient appears out of phase with respect to gravity, while the turbines' thrust in phase. This means that the cyclic control of the turbines' thrust is aimed at compensating gravity.

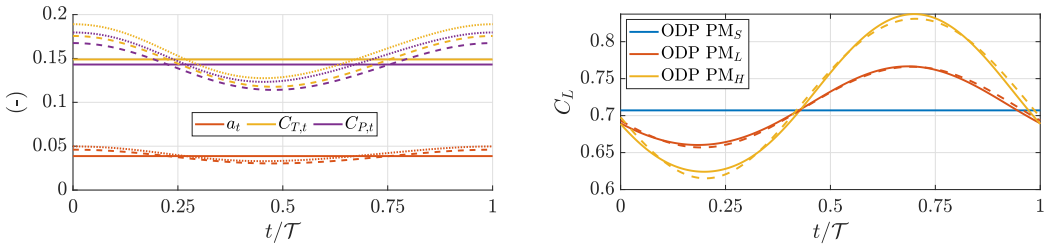

(a) *Onboard turbines induction a_t, thrust coefficient $C_{T,t}$ and power coefficient $C_{P,t}$ as function of non-dimensional time $t/\mathcal{T}$ for ODP PM$_S$ (-), ODP PM$_L$ (- -), ODP PM$_H$ (··).*

(b) *Lift coefficient C_L as function of non-dimensional time $t/\mathcal{T}$ for the three ODPs. The dotted lines are found with the approximation in Eq.* (4.44).

Figure 4.4

The axial induction of the windplane a (Eq. 4.11), is shown in Fig. 4.5a. For all designs, it is constant over the period. The induction $a(t)$ (Eq. (4.11)) is

$$a(t) = a_n(t) + a_f = \frac{C_L(t)}{\pi AR}\lambda(t) + \frac{\kappa_0^{\pi/2}}{4\pi}\frac{\hat{C}_T\hat{\lambda}^2}{(\hat{\lambda} - \hat{C}_T)^{3/2}}. \tag{4.42}$$

The only way for the induction a to be constant is that the product between the two time dependent terms is also constant

$$C_L(t)\lambda(t) = \hat{C}_L\hat{\lambda}\left(1 + \frac{\Delta C_L(t)}{\hat{C}_L}\right)\left(1 + \frac{\Delta\lambda(t)}{\hat{\lambda}}\right) \approx \hat{C}_L\hat{\lambda}\left(1 + \frac{\Delta C_L(t)}{\hat{C}_L} + \frac{\Delta\lambda(t)}{\hat{\lambda}}\right), \tag{4.43}$$

where $\hat{C}_L$ and $\hat{\lambda}$ are the mean value of the lift coefficient and of the wing speed ratio in time. The change in lift coefficient, due to the change in wing speed ratio, necessary to maintain a constant induction is

$$C_L(t) \approx \hat{C}_L \left(1 - \frac{\Delta\lambda(t)}{\hat{\lambda}}\right). \tag{4.44}$$

The dotted lines in Fig. 4.4b are found with the approximation in Eq. (4.44)

In Fig. 4.5b, the power coefficient as a function of the nondimensional time is shown. Recall that the power coefficient is defined as $C_P = \frac{\xi_t^2}{2} C_{P,t} \lambda^3$, where $C_{P,t}$ is shown in Fig. 4.4a and λ in Fig. 4.3a.

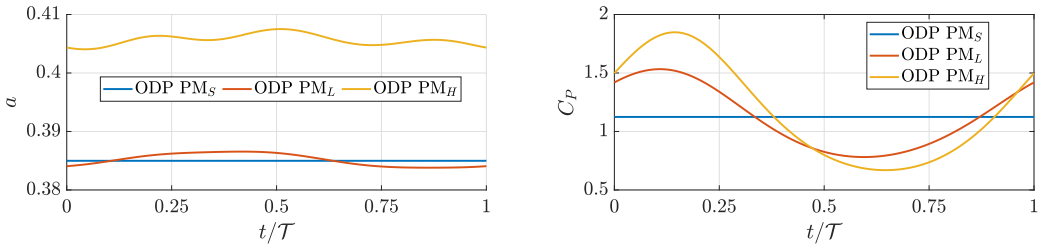

(a) *Axial induction a as function of non-dimensional time $t/\mathcal{T}$ for the three ODPs.*

(b) *Power coefficient C_P as function of non-dimensional time $t/\mathcal{T}$ for the three ODPs.*

Figure 4.5

We now look at the power balance for the different designs, as formulated in Eq. 4.27. In Fig. 4.6a we show the power balance for the steady ODP PM$_S$, in Fig. 4.6b for the ODP PM$_L$ and in Fig. 4.6a for the ODP PM$_H$.

In the steady ODP PM$_S$, the gravitational power is not present, thus the balance is steady. The aerodynamic power C_a is exclusively balanced by the turbines' thrust power $\frac{C_P}{1-a_t}$. A considerable amount of wind power $C_T(1-a)$ is dissipated in parasite drag C_τ.

In the ODP PM$_L$, the gravitational power C_g is present and has its largest value at $\Psi = 0$ and $\Psi = \pi$. The change in kinetic energy $\frac{\partial e_k}{\partial t}$ is in phase with C_g. The plane then accelerates due to gravity. The aerodynamic power C_a is almost constant, while $C_T(1-a)$ and C_τ are not.

We can then solve the integral on the left-hand-side of Eq. (4.29) to find the mean value of the aerodynamic power $\hat{C}_a$. We assume a constant induction a, as a consequence of the optimal result shown in Fig. 4.5a. To find the mean power dissipated in parasite drag $\hat{C}_\tau$, we first solve

$$\begin{aligned}
\frac{1}{\mathcal{T}}\int_0^{\mathcal{T}} \lambda^3 dt &= \hat{\lambda}\tilde{\lambda}^2 \frac{1}{2\pi}\int_0^{2\pi} \left(1 + \sum_{k=1}^{\infty} \tilde{\Lambda}_{s,k} s_{(k\Psi)} + \tilde{\Lambda}_{c,k} c_{(k\Psi)}\right)^2 d\Psi \\
&= \hat{\lambda}\tilde{\lambda}^2 \frac{1}{2\pi}\int_0^{2\pi} 1 + 2\left(\sum_{k=1}^{\infty} \tilde{\Lambda}_{s,k} s_{(k\Psi)} + \tilde{\Lambda}_{c,k} c_{(k\Psi)}\right) + \left(\sum_{k=1}^{\infty} \tilde{\Lambda}_{s,k} s_{(k\Psi)} + \tilde{\Lambda}_{c,k} c_{(k\Psi)}\right)^2 d\Psi \\
&= \hat{\lambda}^3 \left(1 + \frac{1}{2}\sum_{k=1}^{\infty} \left(\tilde{\Lambda}_{s,k}^2 + \tilde{\Lambda}_{c,k}^2\right)\right)^3,
\end{aligned} \tag{4.45}$$

where the relation between $\hat{\lambda}$ and $\tilde{\lambda}$ is given in Eq. (4.24).

The mean power balance can therefore be written as

$$\underbrace{\frac{1}{\mathcal{T}}\int_0^{\mathcal{T}}\frac{C_P}{(1-a_t)}dt}_{\text{turbines' thrust power}} = \underbrace{a_n(1-a)\hat{\lambda}}_{\text{wind power}} - \underbrace{\frac{C_{D,p}}{\pi AR}\hat{\lambda}^3\left(1+\frac{1}{2}\sum_{k=1}^{\infty}\left(\tilde{\Lambda}_{s,k}^2+\tilde{\Lambda}_{c,k}^2\right)\right)^3}_{\text{parasite drag power}}, \quad (4.46)$$

where the left-hand-side is the mean turbines' thrust power over the loop and the right-hand-side is the mean aerodynamic power. To maximize the generated power, the wind power shall be maximized and the power dissipated in parasite drag minimized.

To maximize the wind power, the induction is constant. Therefore, the wing, which travels with a varying velocity in the circular trajectory, generates constant induced velocities. This means that the trailed vorticity is constant over the trajectory and so is the bound circulation.

To minimize the power dissipated in parasite drag, the wing speed ratio shall be as constant as possible. To obtain a constant velocity, the onboard turbines should convert all the potential energy to electric energy, avoiding the conversion to kinetic energy. However, the potential energy converted to electric energy is reduced by the onboard generation efficiency, which decreases for increasing turbines' axial induction $\frac{C_{P,t}}{C_{T,t}} = 1-a_t$. It is therefore optimal to let a part of the gravitational energy to be converted into kinetic energy and a part into electric energy. The ratio of energy converted to kinetic and to electric is defined by the nonlinear conversion processes efficiencies.

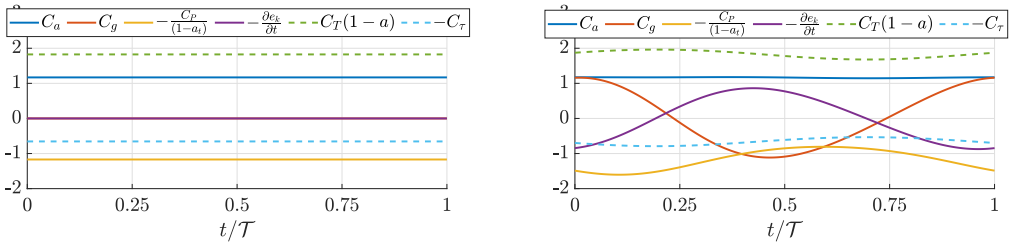

(a) *Non-dimensional power balance for the ODP PM$_S$.* **(b)** *Non-dimensional power balance for the ODP PM$_L$.*

Figure 4.6

In the ODP PM$_H$, the nondimensional mass μ is considered among the design variables. Increasing the nondimensional mass increases the opening angle (Eq. 4.8), thus increases the trajectory radius and decreases the inverse turning ratio κ_0. This results in a decrease of the induction due to the far wake a_f and thus an increase in aerodynamic power. However, a larger and larger mass also increases the gravitational power C_g. The conversion of the gravitational power, as just discussed, has an associated efficiency. For these two conflicting reasons, the optimal mass, which is the main parameter determining the trajectory radius, is finite. In Fig. 4.7b the dependency of the power coefficient with respect to the non-dimensional mass is shown, highlighting that the optimal mass is finite.

In Figure 4.8a, the optimal power coefficients found by solving ODPs with prescribed aspect ratios are shown. The optimal aspect ratios are finite and have low values. Increasing the aspect ratio is found to be detrimental for power production. The

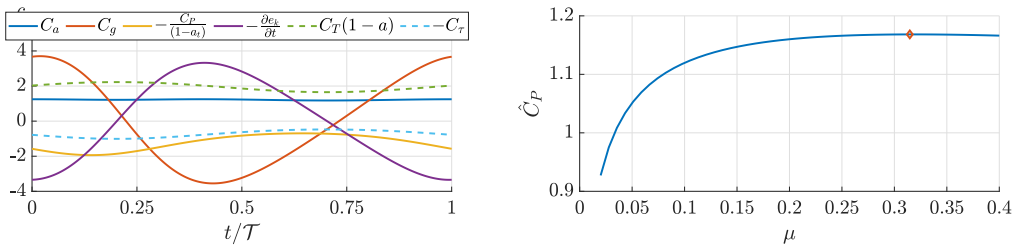

(a) *Non-dimensional power balance for the ODP PM$_H$.* **(b)** *Power coefficient $\hat{C}_P$ found by solving ODPs with prescribed non-dimensional mass μ.*

Figure 4.7

aspect ratio can be understood as the solidity for wind turbines.

In Fig. 4.8b, the power coefficients found by solving OCPs with prescribed lift coefficients $\tilde{C}_L$ are shown for the light design PM$_S$ and the heavy design PM$_H$. As for conventional turbines, the power coefficient is decreased when decreasing or increasing the lift coefficient with respect to the optimal value.

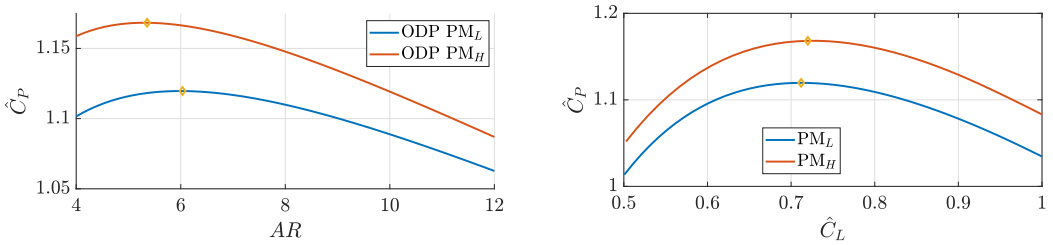

(a) *Power coefficient $\hat{C}_P$ found by solving ODPs with prescribed aspect ratio AR for the optimal designs ODs.* **(b)** *Power coefficient $\hat{C}_P$ as a function of the mean lift coefficient in time $\hat{C}_L$, found by solving OCPs with prescribed $\tilde{C}_L$ for the optimal designs ODs.*

Figure 4.8

We can investigate the operations of the optimal design PM$_L$ and PM$_H$ as a function of wind speed by solving optimal control problems (OCPs). Note that the optimal control problem formulation (Sect. 4.6) lists among the inequality constraints the rated power constraint c_{P_r}. We need then to decide which rated power to assign to the two windplanes. Recall that the rated wind speed is typically determined by economic factors, so we can arbitrarily select a rated power. We chose $P_r = 100$ kW. Above the rated wind speed, a number of strategies to limit power and loads are available (e.g. decreasing lift coefficient, increasing or decreasing the opening angle Φ, increasing the elevation angle, etc.). Analyzing the windplane behavior above the rated wind speed with this simplified formulation would be misleading and therefore it is avoided.

Figure 4.9a shows the power curve of the two windplanes up to $v_w = 10$ m/s and the minimum and maximum power over the loop at low wind speed. The heavy design PM$_H$ has a minimum negative power at very low wind speed. This means that the onboard turbines are used as propellers in the ascending part of the loop. It is inefficient to use the turbine as propellers because the power used to propel the plane has to pass the electric efficiencies twice: when converted from shaft power to electric power and when converted from electric power to shaft power. This phenomenon reduces the

mean electric power and thus it should be avoided if possible. Moreover, a lighter design reduces the power needed during take-off and landing.

In Figure 4.9b the tether stress curve is shown. After the rated power is reached, the tether stress decreases.

The power and tether stress trends are typical trends for wind energy machines.

Using the Weibull distribution function for the wind speed (Eq. 4.35), we can estimate the capacity factor CF and the tether life due to creep $\mathcal{T}_{te}$ (Sect. 4.7), considering only the wind speeds from 3 to 10 m/s. The capacity factor for both designs is of $CF = 0.37$. For the light design PM_L the tether life is $\mathcal{T}_{te} = 27$ years, while for the heavy design PM_H $\mathcal{T}_{te} = 30$ years. If we extend the power curve up to $v_w = 25$ m/s, the capacity factor for both design would be $CF = 0.59$.

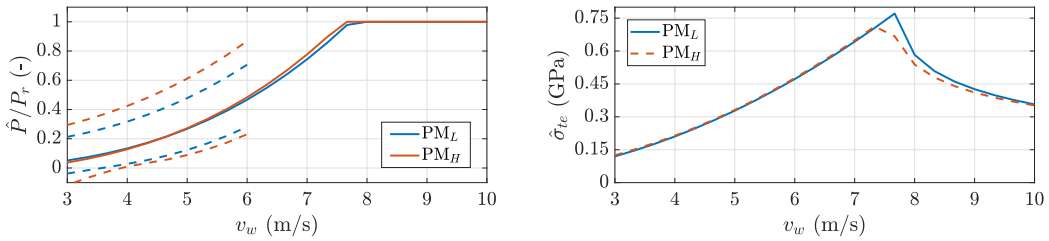

(a) *Normalized power found by solving OCPs at different wind speeds v_w for the light design PM_L and the heavy PM_H design. The rated power is $P_r = 100$ kW.*

(b) *Mean tether stress $\hat{\sigma}_{te}$ found by solving OCPs at different wind speeds v_w for the light design PM_L and the heavy PM_H design.*

Figure 4.9

Figure 4.10a shows the power coefficients for the two planes as functions of the wind speed. The highest power coefficient is found at the rated wind velocity. For wind speeds below the rated wind speed, the power coefficients decrease. This is because gravity is influencing more and more the dynamics, decreasing the power output. For wind speeds above the rated wind speed, the rated power constraint becomes active, thus decreasing the power coefficient. Reducing the power coefficient is mainly achieved by reducing the lift coefficient, as shown in Figure 4.10b. This is typical of wind energy machines, but it is not the only option available for windplanes.

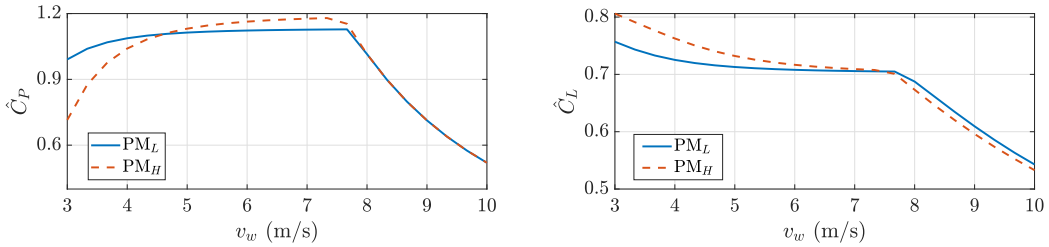

(a) *Mean power coefficient $\hat{C}_P$ found by solving OCPs at different wind speeds v_w for the light design PM_L and the heavy PM_H design.*

(b) *Mean lift coefficient $\hat{C}_L$ found by solving OCPs at different wind speeds v_w for the light design PM_L and the heavy PM_H design.*

Figure 4.10

Figure 4.11a shows the thrust coefficients as functions of wind speed. Before the

rated wind speed, the $\hat{C}_T$ is approximately constant, then it decreases. To conclude, Fig. 4.11b shows the windplanes velocity as a function of wind speed. The maximum velocity $\hat{u}$ is found at the rated wind speed and it is $\hat{u} \approx 70$ m/s. Typically the blade tips of conventional wind turbines reach a velocity of 80 to 100 m/s. The tip velocity of a conventional turbine is limited because of noise (if onshore) and erosion. We then expect the noise produced by the main wing and the erosion on the main wing to be reduced compared to conventional wind turbines.

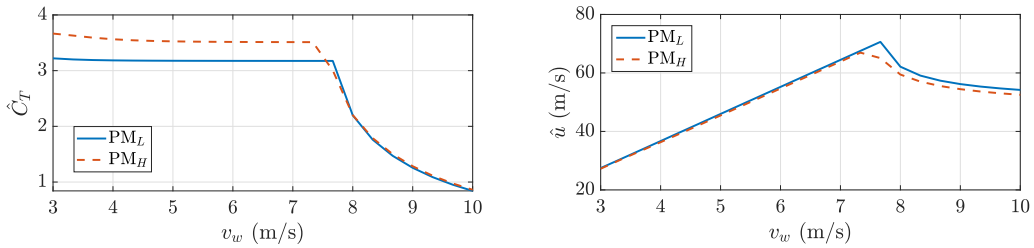

(a) *Mean thrust coefficient $\hat{C}_T$ found by solving OCPs at different wind speeds v_w for the light design PM$_L$ and the heavy PM$_H$ design.*

(b) *Mean tangential velocity $\hat{u}$ found by solving OCPs at different wind speeds v_w for the light design PM$_L$ and the heavy PM$_H$ design.*

Figure 4.11

4.10 Discussion

In this chapter, we assume circular trajectories, so that only one degree of freedom in the tangential direction is remaining. We look for a periodic solution to the tangential equation of motion by expanding the wing speed ratio into Fourier series and applying a harmonic balance methodology. The power balance is composed by the aerodynamic power, the turbines' thrust power, the gravitational power and the change in kinetic energy. The aerodynamic power is the wind power harvested by the plane minus the power dissipated in parasite drag. The mean values in time of the aerodynamic power and the turbines' thrust power are equal.

We use this simplified dynamic model to formulate an optimal control problem (OCP), where the cyclic controls of the lift coefficient C_L and the onboard turbines induction a_t are the control inputs. We later upgrade the OCP into an optimal design problem (ODP), where the wing aspect ratio AR, the windplane non-dimensional mass μ and the tether diameter ratio d_{te} are included among the design variables. This simplified design methodology shows how different disciplines combine in the design process.

We find that the optimal design is obtained by operating the wing at the maximum lift-to-drag ratio of the airfoil. In windplanes, we then need to use airfoils designed to maximize the lift to drag ratio. These airfoils are well-known as they are used for wind turbines, gliders, airplanes designed to have efficient cruise, and other applications.

If the wing is designed to operate at the maximum lift-to-drag ratio of the airfoil, the optimal wing aspect ratio is finite and has a low value. Low aspect ratio designs are easier to be manufactured and meet the weight requirements.

Gravitational potential energy is being exchanged with kinetic energy, aerodynamic energy and electric energy over one revolution. Since this exchange comes with an

associated efficiency, the plane mass and the related trajectory are designed to reduce the potential energy fluctuating over the loop. Reducing the potential energy means reducing the turning radius and the mass. However, for decreasing turning radii, the available wind power decreases because the windplane sweeps a lower area. For these two conflicting reasons, the optimal mass is finite. Depending on the independent variables, extremely light designs might be not required and the optimal mass might be obtained with cheap and sustainable materials.

The windplane makes work on the wind by slowing it down of the induced velocity. It is optimal to have a constant induction over the loop to maximize the raw wind power to be harvested. Therefore, the lift coefficient changes according to the change in wing speed ratio to ensure a constant intensity of the wing circulation, which translates in a constant induction.

Having understood these key points, we can safely move to the second part of this thesis, where we approach the design modeling the windplane as a rigid body.

The formulation presented in this chapter and the resulting considerations on optimal designs are part of the abstract submitted to Torque 2024 Conference (Trevisi and Croce (2024))

4.11 State of the art

4.11.1 Optimal control problem

Optimal control problems employ dynamical models, ranging from low to high fidelity. Typically, low- to mid-fidelity models are used to investigate optimal trajectories of AWE. Low-fidelity dynamic models are characterized by multiple assumptions, which simplify the models, and by the low computational cost. The quasi-steady model (van der Vlugt et al. (2019)) assumes the kite as a point mass in steady state for each point of the loop. This model is validated with experimental data (Schelbergen and Schmehl (2020)) and it is considered accurate for soft kites, where the inertia is low and the AWES quickly reaches the steady state. A similar approach is considered while deriving the Unicycle model (Fagiano et al. (2014); Vermillion et al. (2021)). Also this model, based on a point mass, is developed for soft-wing AWES and computes the velocity vector via quasi-steady flight equations. The kite orientation is found by a turning law that is derived from lateral force equilibrium and is validated through a number of experiments. The Unifoil model (Cobb et al. (2020)) is derived by modification of the Unicycle model in order to be applied to fixed-wing AWES. Indeed, the quasi-steady assumption is removed and the turning maneuvers modelled with a yaw dynamic equation.

Higher fidelity, but still computationally efficient, dynamic models are developed by Sánchez-Arriaga et al. (2017, 2019); Sánchez-Arriaga and Serrano-Iglesias (2021) as a part of the Lagrangian Kite Flight Simulators (LAKSA) package based on minimal coordinates, and by Gros and Diehl (2013) to study the dynamics of multiple AWES configurations. Moreover, thorough Newtonian dynamic models are used to compute reference flight paths and the consequent flight path control for soft-wing AWES (Fechner et al. (2015); Fechner and Schmehl (2016)) and for fixed-wing AWES (Licitra et al. (2019); Malz et al. (2019); Eijkelhof and Schmehl (2022)).

The dynamic models just introduced are particularly suitable to be used within opti-

mal control studies for their computational inexpensiveness and for the reduced number of nonlinearities compared to even higher fidelity codes, such as kiteFAST (Jonkman et al. (2018)). The Unicycle and Unifoil models, introduced earlier, are mainly used to compute reference flight paths and for flight path control development (Cobb et al. (2020); Fernandes et al. (2021)). To ease the deployment of optimal control problems for AWE, *awebox* (De Schutter et al. (2023)) is developed and used, for instance by Leuthold et al. (2018), Haas et al. (2019a) and De Schutter et al. (2019), to solve optimal control problems. *awebox* solves optimal control problems in time, imposing periodicity constraints. A similar optimal control problem is studied by Horn et al. (2013), Malz et al. (2020a) and Malz et al. (2020b), where the optimal trajectory is found in time using a discretization by direct collocation and a homotopy strategy based on the relaxation of the dynamic constraints (Gros et al. (2013)). Licitra et al. (2019) solved an optimal control problem with an experimentally validated dynamic model of a Ground-Gen AWES. They find that, under some prescribed constraints, circular and figure of eight trajectories produce similar mean power and that closed-loop control enhance robustness but decreases power production of about 10 %. Control in all operation phases is studied by Rapp et al. (2019) and Todeschini et al. (2021).

Pasquinelli (2021) investigates the power losses in a circular trajectory with a dynamical quasi-analytical model. He finds that the causes of power losses are mainly two: the AWES span non-perpendicularity with respect to the incoming wind during the motion and the AWES speed fluctuation over the loop. Makani team (Tucker (2020)) studies the flight trajectories of Fly-Gen AWES with a simplified quasi-analytical approach, aiming at describing their physical characteristics. They run their flight simulator for different trajectories and production strategies to derive analytical expressions, which can describe the consequences of different operational choices. Their production strategy at low wind speed is to convert part of the potential energy into kinetic and part into electrical, when the AWES moves downward. To reduce the potential energy exchange, they suggest to squash the trajectories along the vertical direction. Moreover, they explain that using electrical power to push the AWES upward drastically decreases the overall power production, as power needs to be converted from mechanical to electrical and again from electrical to mechanical, so that the related efficiencies are counted twice. They, in accord with the study for Ground-Gen by Stuyts et al. (2015), conclude that the electrical conversion losses should be considered when deciding on the production strategy. Trevisi et al. (2022a) investigate optimal trajectories for Fly-Gen AWESs using the harmonic balance method detailed in Sect. 7.1. A simplification of this method is used in the current Section to solve the tangential equation of motion. This method allows to potentially reduce the problem size by solving only for the main harmonics and to implicitly impose periodicity of the solution. The flight trajectory is described by the Fourier coefficients of the dynamics (elevation and azimuth angles) and of the control inputs (on-board wind turbines thrust and AWES roll angle). To isolate the effects of each physical phenomenon, optimal trajectories are presented with an increasing level of physical representation from the most idealized case: i) If the mean thrust power (mechanical power linked to the dynamics) is considered as the objective function, optimal trajectories are characterized by a constant AWES velocity over the loop and a circular shape. This is done by converting all the gravitational potential energy into electrical energy. At low wind speed, on-board

wind turbines are then used as propellers in the ascendant part of the loop; ii) If the mean shaft power (mechanical power after momentum losses) is the objective function, a part of the potential energy is converted into kinetic and the rest into electrical energy. Therefore, the AWES velocity fluctuates over the loop; iii) If the mean electrical power is considered as the objective function, the on-board wind turbines are never used as propellers because of the power conversion efficiency. Optimal trajectories for case ii) and iii) have a circular shape squashed along the vertical direction. The optimal control inputs can be generally modelled with one harmonic for the on-board wind turbines thrust and two for AWES roll angle without a significant loss of power, demonstrating that the absence of high-frequency control is not detrimental to the power generated by Fly-Gen AWES.

4.11.2 Tether design

Bosman et al. (2013) describe the design drivers for the tether and highlights the creep phenomenon as main cause of tether failure. The authors provide the creep curves relating the tether stress to the operational life for three different rope types and suggest the usage of Miner' Rule for the life estimation. Trevisi et al. (2020b) formulate the Miner' Rule to estimate the tether life and apply this formulation in a design context (Trevisi et al. (2021b)). Bauer et al. (2018) design the tether diameter according to a maximum tether force.

4.11.3 Optimal design problem

Optimal system design problems in airborne wind energy are approached with engineering models by Fasel et al. (2017), Bauer et al. (2018) and Trevisi et al. (2021b). Candade et al. (2020) perform the aero-structural design for specific design load cases to minimize the wing mass.

Fasel et al. (2017) optimize the aerodynamic shape, compliant structure, and composite layup of a morphing wing, with the objective of maximizing the the average annual power production per wing area. Bauer et al. (2018) perform a system design to maximize an economic metric per wing area. Trevisi et al. (2021b) perform a system design to maximize the annual energy production and later the cost of energy. The wing area is fixed within an optimization, leading to optimal designs per wing area. Naik et al. (2021, 2022) study the co-design problem for an underwater crosswind GroundGen system maximizing the power and minimizing the structural mass. The wing area is fixed within one optimization, leading to optimal designs per wing area. Naik and Vermillion (2024) integrate the site selection in the design problem.

In this chapter, we formulate the design problem in a different way compared to the literature, by optimizing the system design per wingspan. This is similar to what is typically done for wind turbines, where the design is optimized per lifting body span and not per lifting body area. If we perform the aerodynamic design of wind turbines per blade area, the optimal rotor would have infinite long blades, as in this condition the swept area is maximized and thus is power. For conventional operations of wind turbines (manufacturing, storage in hangars, transportation, etc.), the critical dimension is the lifting body span, and not the area. Thus, we claim that we should optimize windplanes per wingspan and not per wing area.

4.11.4 Optimal aspect ratio

As just discussed, designing the system per wing area leads to very large aspect ratio, as found by Fasel et al. (2017), Bauer et al. (2018), Tucker (2020), Trevisi et al. (2021b) among others.

Trevisi et al. (2023b) introduce the power coefficient as defined in this thesis (Eq. 2.19) and consequently speculate on the existence of an optimal finite aspect ratio when optimizing for the power production per wingspan.

4.11.5 Optimal airfoils

Airfoils used in airborne wind energy are designed to maximize the metric $\frac{C_L^3}{C_d^2}$ (Bauer et al. (2018); Thedens et al. (2019); Tucker (2020); De Fezza and Barber (2022); Rangriz and Kheiri (2023); Porta Ko et al. (2023) among others) and thus to be operated at high lift coefficients. This metric points to multi-elements airfoils to achieve high lift coefficients, close to stall. These airfoils are complex to be designed, manufactured and operated. Using this metric is a consequence of optimizing the design per wing area and not per wingspan.

If we design the system per wingspan and consider the optimal aspect ratio, we find that the airfoils which maximize the aerodynamic efficiency $\frac{C_L}{C_d}$ are required. These airfoils are used in wind turbines and gliders, among other applications, and they are well-known in the literature.

This, to the best of the author's knowledge, is fist time these airfoils are considered optimal for crosswind airborne wind energy applications.

4.11.6 Optimal mass

In airborne wing energy, the system mass is typically associated with power losses, as the system has to stay airborne and centrifugal forces are typically seen as a source of power losses. Thus, the system mass is typically minimized (Bauer et al. (2018); Candade et al. (2020); Tucker (2020); Trevisi et al. (2021b)). Including a wake model and using the radial component of the tether force to turn (and not the aerodynamic lift), we find that there exist an optimal trajectory radius and thus an optimal mass (which is the main parameter determining the trajectory radius).

This, to the best of the author's knowledge, is fist time an optimal mass is theorized for crosswind airborne wind energy applications.

Part II

Rigid body

Can windplanes fly stable orbits?

CHAPTER 5

Equations of motion

The flight mechanics problem of windplanes is fundamentally different from the one of airplanes for mainly three reasons: the presence of the wind, needed for the power generation (the average wind speed does not influence conventional aircraft flight stability analyses, as the inertial coordinate system can be considered to move with the average wind speed, but this is not the case for windplanes), the presence of the tether, which transfers the aerodynamic forces to the ground, and the always-present turning maneuver. It is therefore clear that conventional design techniques assuming straight and level flight can hardly be used for windplanes. To understand the flight mechanics problem we then need to develop a methodology, analogue to the one used for conventional airplanes, that consider the characteristics of windplanes.

In Chapter 4, we learned that potential energy is being exchanged with kinetic and electric energy over one revolution. This phenomenon is intrinsically non linear, as the change of kinetic energy is function of the velocity squared. This means that for capturing the potential energy exchange in a design framework we need to implement the non-linear equations of motion and a non-linear aerodynamic model.

5.1 Coordinate systems

We define four coordinate systems to derive the equations of motion. The ground coordinate system $\mathcal{F}_G$ (Figure 5.1) is centered at the ground station and it is inertial. Its origin is denoted as *G*. $\boldsymbol{e}_{3,g}$ points upwind and $\boldsymbol{e}_{1,g}$ toward the ground. A second coordinate system $\mathcal{F}_R$ (*R*otating) is defined such that it moves with an angular velocity $\dot{\Psi}$ around $\boldsymbol{e}_{3,r}$ and $\boldsymbol{e}_{2,r}$ points to the tether attachment point.

The third coordinate system $\mathcal{F}_B$ (Body) is attached to the windplane and it is centered at the tether attachment. The geometry and the inertia properties are given in this

coordinate system. The fourth coordinate system $\mathcal{F}_S$ (Stability) is attached to the the windplane, it is centered at the tether attachment but it is rotated of a constant pitch angle with respect to the Body coordinate system.

In Part I, we wrote the equation of motion of the point mass in the rotating coordinate system $\mathcal{F}_R$, we now write the in the equation of motion of the rigid body in the stability coordinate system $\mathcal{F}_S$.

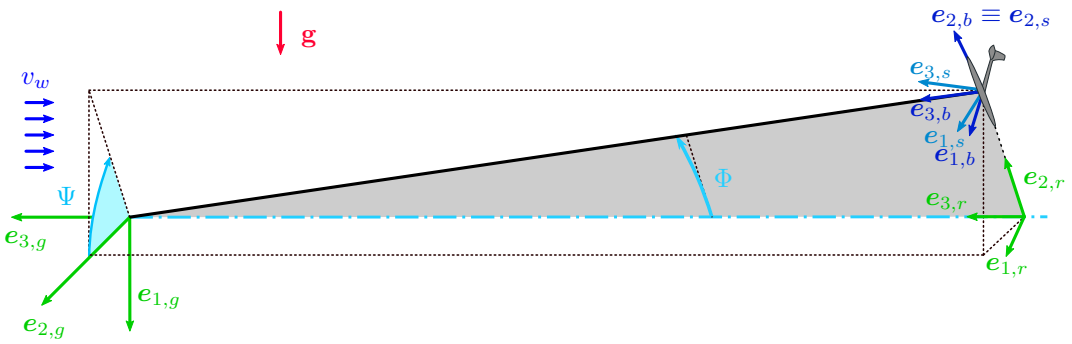

Figure 5.1: *Ground coordinate system $\mathcal{F}_G$, Rotating coordinate system $\mathcal{F}_R$, Body coordinate system $\mathcal{F}_B$ and Stability coordinate system $\mathcal{F}_S$.*

The rotation matrix $\mathbf{R}^G_{z,GR}(\Psi)$, which brings from $\mathcal{F}_G$ to $\mathcal{F}_R$, is defined by one planar rotation of Ψ around the $\boldsymbol{e}_{3,g}$ axis (see Appendix A for rotational matrix notation).

The body coordinate system $\mathcal{F}_B$ (Figure 2.1) is centered at the tether attachment point and is moving with the windplane. Its origin is denoted as *T*. The geometry and the inertia properties are given in this coordinate system. The rotation matrix which brings from $\mathcal{F}_R$ to $\mathcal{F}_B$ is defined with three sequential planar rotations, around the third, first (rotated) and second (rotated) axes of the frame respectively (Euler angles in the sequence $(3,1,2)$)

$$\mathbf{R}^R_{RB}(\phi,\theta_{rb},\psi) = \mathbf{R}^R_{R''B}(\theta_{rb})\,\mathbf{R}^R_{R'R''}(\phi)\,\mathbf{R}^R_{RR'}(\psi) = \mathbf{R}^R_{z,RR'}(\psi)\,\mathbf{R}^{R'}_{x,R'R''}(\phi)\,\mathbf{R}^{R''}_{y,R''B}(\theta_{rb})\,. \tag{5.1}$$

The stability coordinate system $\mathcal{F}_S$ is centered at the tether attachment point and is moving with the windplane. The rotation matrix which brings from $\mathcal{F}_B$ to $\mathcal{F}_S$ is defined with one planar rotation around $\boldsymbol{e}_{2,b}$ of a constant angle θ_{bs}: $\mathbf{R}^B_{y,BS}(\theta_{bs})$. Note that we expect the mean plane pitch to change as a function of wind speed to limit power, similar to conventional turbines. The pitch angle θ_{bs}, constant over one time integration, can be arbitrarily chosen as function of wind speed to follow this pitch variation. This is important when employing a linearized aerodynamic model about nonlinear operating points, as in this thesis. We choose to write the equations of motion in $\mathcal{F}_S$ and not in $\mathcal{F}_B$ for this reason.

The rotation matrix which brings from from $\mathcal{F}_R$ to $\mathcal{F}_S$ is then

$$\mathbf{R}^R_{RS}(\phi,\theta,\psi) = \mathbf{R}^R_{BS}(\theta_{bs})\,\mathbf{R}^R_{RB}(\phi,\theta_{rb},\psi) = \mathbf{R}_z(\psi)\,\mathbf{R}_x(\phi)\,\mathbf{R}_y(\underbrace{\theta_{rb}+\theta_{bs}}_{\theta}). \tag{5.2}$$

As a result of the choice of the rotation sequence for $\mathbf{R}_{RB}^{R}$, the rotation matrix is function of $\theta = \theta_{rb} + \theta_{bs}$.

The rotation matrix which brings from from $\mathcal{F}_G$ to $\mathcal{F}_S$ is then

$$\mathbf{R}_{GS}^{G} = \mathbf{R}_{BS}^{G}\left(\theta_{bs}\right)\mathbf{R}_{RB}^{G}\left(\phi, \theta_{rb}, \psi\right)\mathbf{R}_{GR}^{G}\left(\Psi\right) = \mathbf{R}_{z}\left(\Psi + \psi\right)\mathbf{R}_{x}\left(\phi\right)\mathbf{R}_{y}\left(\theta\right). \tag{5.3}$$

5.2 Equations of motion in the stability coordinate system $\mathcal{F}_S$

The stability coordinate system $\mathcal{F}_S$ is centered on the tether connection, so the windplane center of mass can therefore be elsewhere. The equations of motion for a non-barycentric moving coordinate system are

$$\begin{aligned}&\begin{bmatrix} m\mathbf{1} & -m\boldsymbol{tcg}^{\times} \\ m\boldsymbol{tcg}^{\times} & \mathbf{I} \end{bmatrix}\begin{pmatrix} \dot{\boldsymbol{v}} \\ \dot{\boldsymbol{\omega}} \end{pmatrix} + \\ &\begin{bmatrix} \boldsymbol{\omega}^{\times} & \mathbf{0} \\ \boldsymbol{v}^{\times} & \boldsymbol{\omega}^{\times} \end{bmatrix}\begin{bmatrix} m\mathbf{1} & -m\boldsymbol{tcg}^{\times} \\ m\boldsymbol{tcg}^{\times} & \mathbf{I} \end{bmatrix}\begin{pmatrix} \boldsymbol{v} \\ \boldsymbol{\omega} \end{pmatrix} = \begin{pmatrix} \boldsymbol{F} \\ \boldsymbol{T}_t \end{pmatrix},\end{aligned} \tag{5.4}$$

where m is the windplane mass, $\mathbf{1}$ is a 3-by-3 identity matrix, $\boldsymbol{tcg}$ is the position of the center of mass in $\mathcal{F}_S$, the symbol $()^{\times}$ indicates the skew-symmetric tensor, $\mathbf{I}$ is the inertia tensor by components in $\mathcal{F}_S$, $\boldsymbol{v}$ and $\boldsymbol{\omega}$ are the linear and angular velocity of $\mathcal{F}_S$ with respect to $\mathcal{F}_G$, expressed in $\mathcal{F}_S$, and $\boldsymbol{f}$ and $\mathbf{T}_t$ are the external forces and moments.

We rewrite the equations of motion in compact form as

$$\mathbf{m}\dot{\mathrm{v}} + \mathrm{v}^{\times}\mathbf{m}\mathrm{v} = \boldsymbol{F}_{ext}, \tag{5.5}$$

wherein

$$\mathbf{m} = \begin{bmatrix} m\mathbf{1} & -m\boldsymbol{tcg}^{\times} \\ m\boldsymbol{tcg}^{\times} & \mathbf{I} \end{bmatrix}, \quad \mathrm{v}^{\times} = \begin{bmatrix} \boldsymbol{\omega}^{\times} & \mathbf{0} \\ \boldsymbol{v}^{\times} & \boldsymbol{\omega}^{\times} \end{bmatrix}, \quad \mathrm{v} = \begin{pmatrix} \boldsymbol{v} \\ \boldsymbol{\omega} \end{pmatrix}, \tag{5.6}$$

and $\boldsymbol{F}_{ext} = (\boldsymbol{F}; \boldsymbol{T}_t)$.

5.3 Kinematic constraints: linear velocity

To properly write the kinematic constraints for the linear velocity, we define the tether reference frame $\mathcal{F}_{Te}$. $\mathcal{F}_{Te}$ is centered at the tether attachment and it defined by a rotation around $\boldsymbol{e}_{1,r}$ of Φ, as in Fig. 5.2. The rotation matrix which brings from $\mathcal{F}_R$ to $\mathcal{F}_{Te}$ is then

$$\mathbf{R}_{RTe} = \mathbf{R}_{x}(\Phi), \tag{5.7}$$

with $\mathbf{R}_{x}(\Phi)$ given in Appendix A.

The velocity of the reference frame $\mathcal{F}_S$ with respect to $\mathcal{F}_G$, expressed in $\mathcal{F}_T$, is

$$\boldsymbol{v}_{GS}^{Te} = \mathbf{R}_{TeS}\boldsymbol{v} = \mathbf{R}_{TeR}\mathbf{R}_{RS}\boldsymbol{v} = \begin{bmatrix} -L_{te}\dot{\Psi}\sin\Phi \\ L_{te}\dot{\Phi} \\ \dot{L}_{te} \end{bmatrix}, \tag{5.8}$$

where $\dot{L}_{te} = 0$.

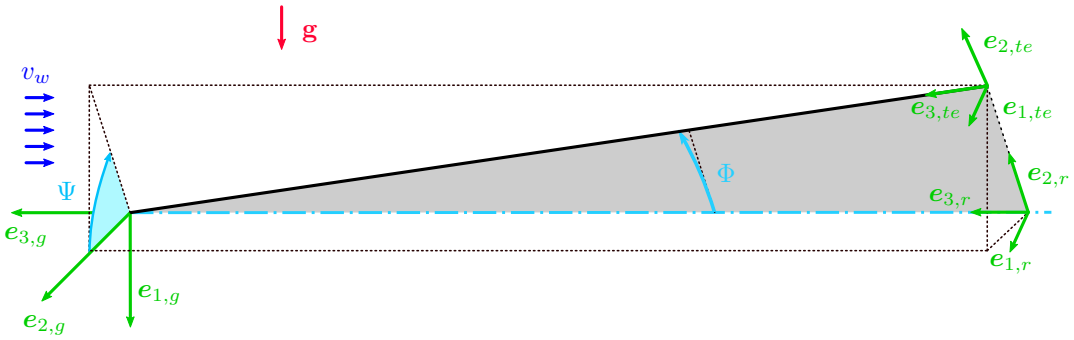

Figure 5.2: *Ground coordinate system $\mathcal{F}_G$, Rotating coordinate system $\mathcal{F}_R$ and tether coordinate system $\mathcal{F}_{te}$.*

5.4 Kinematic constraint: angular velocity

The angular velocity of the reference frame $\mathcal{F}_S$ with respect to $\mathcal{F}_G$, expressed in $\mathcal{F}_G$ is

$$\boldsymbol{\omega}_{GS}^{G} = \mathbf{R}_{GS}\boldsymbol{\omega} = \begin{bmatrix} 0 \\ 0 \\ \dot{\Psi}+\dot{\psi} \end{bmatrix} + \mathbf{R}_z(\Psi+\psi)\begin{bmatrix} \dot{\phi} \\ 0 \\ 0 \end{bmatrix} + \mathbf{R}_z(\Psi+\psi)\mathbf{R}_x(\phi)\begin{bmatrix} 0 \\ \dot{\theta} \\ 0 \end{bmatrix} \tag{5.9}$$

In alternative, we can express the same expression in $\mathcal{F}_S$ as

$$\boldsymbol{\omega} = \mathbf{R}_y^T(\theta)\mathbf{R}_x^T(\phi)\begin{bmatrix} 0 \\ 0 \\ \dot{\Psi}+\dot{\psi} \end{bmatrix} + \mathbf{R}_y^T(\theta)\begin{bmatrix} \dot{\phi} \\ 0 \\ 0 \end{bmatrix} + \begin{bmatrix} 0 \\ \dot{\theta} \\ 0 \end{bmatrix} \tag{5.10}$$

5.5 External force: gravity

Since the center of mass is not located at the center of the coordinate system, the gravitational force generates moments. This is dissimilar to the most typical treatment of the dynamic equations for aircraft, which are typically put in barycentric body components. For windplanes, and considering the reference at the anchor point of the tethering system, the force due to gravity can be written as

$$\boldsymbol{F}_g = \begin{bmatrix} \mathbf{1} \\ \boldsymbol{tcg}^{\times} \end{bmatrix} \mathbf{R}_{SG}\begin{bmatrix} mg \\ 0 \\ 0 \end{bmatrix} = mg\mathbf{P}_g\mathbf{R}_{SR}\begin{bmatrix} \cos\Psi \\ -\sin\Psi \\ 0 \end{bmatrix}, \tag{5.11}$$

where $\boldsymbol{tcg}$ is the position of the center of mass with respect to the tether attachment expressed in $\mathcal{F}_S$ and $\mathbf{R}_{SG}$ is the rotational matrix which brings from $\mathcal{F}_S$ to $\mathcal{F}_G$ (its transposed is given in Eq. 5.3).

5.6 External force: tether tensile force

Since the equations of motion are written in a reference system centered at the tether attachment, no moment is generated by the tether.

The nonlinear equations of motion are

$$\mathbf{m}\dot{\mathrm{v}} + \mathrm{v}^{\times}\mathbf{m}\mathrm{v} = \boldsymbol{F}_a + \boldsymbol{F}_t + \boldsymbol{F}_g + \boldsymbol{F}_{te}, \tag{5.12}$$

where $\boldsymbol{F}_a$ is the aerodynamic force vector, $\boldsymbol{F}_t$ the turbines' force vector, $\boldsymbol{F}_g$ the gravitational force and $\boldsymbol{F}_{te}$ the tether force vector.

The tether force can be written explicitly as

$$\boldsymbol{F}_{te}^{Te} = \mathbf{R}_{TS}\left(\mathbf{m}\dot{\mathrm{v}} + \mathrm{v}^{\times}\mathbf{m}\mathrm{v} - \boldsymbol{F}_a - \boldsymbol{F}_t - \boldsymbol{F}_g\right), \tag{5.13}$$

The tether force in the tether reference frame $\mathcal{F}_{Te}$ is

$$\boldsymbol{F}_{te}^{Te} = T_{te}\boldsymbol{e}_{3,te} \tag{5.14}$$

where T_{te} is the tether tension. Since we model the tether as a constraint, no change of velocity can happen along $\boldsymbol{e}_{3,t}$ ($\dot{L}_{te} = 0$), such that

$$T_{te} = \mathbf{R}_{TS}\left(\mathrm{v}^{\times}\mathbf{m}\mathrm{v} - \boldsymbol{F}_a - \boldsymbol{F}_t - \boldsymbol{F}^g\right) \cdot \boldsymbol{e}_{3,te} \tag{5.15}$$

This value of the tether force is then needed to ensure the equilibrium in the tether direction.

5.7 Discussion

In this chapter, the rigid-body nonlinear 6 degree-of-freedom equations of motion are written in a reference system attached to the windplane and centered at the tether attachment. The equations of motion are complemented with 6 kinematic constraints, so that a set of 12 equations describes the rigid-body dynamics. The plane 3D position is parameterized with the azimuth angle Ψ, the opening angle Φ and the tether length L_{te}, which is constant. The plane 3D orientation is parameterized with the azimuth angle Ψ and the three Euler angles (ϕ, θ, ψ). With this formulation, the Euler angles are expected to be small for nearly circular trajectories. The plane linear and angular velocities are described with a common formulation for airplanes.

The external forces are the aerodynamic force, the onboard turbines' force, the gravity and the tether tensile force. The gravitational force is applied to the center of mass and thus generated moments. The tether acts as a constraint, so the resulting tensile force can be found from the force balance in the tether direction. The aerodynamic force and the onboard turbines' force are derived in the next chapter.

CHAPTER 6

Aerodynamic forces

In this chapter, we model the windplane nonlinear aerodynamics to characterize the external forces in the nonlinear equations of motion (Eq. 5.5).

In Chapter 4, we learned that potential energy is being exchanged with kinetic energy, wind energy and electric energy over one revolution. This phenomenon is intrinsically nonlinear, as the change of kinetic energy is function of the velocity squared. To cope with this non-linearity, the aerodynamic model cannot be linearized with respect to one single reference condition in the loop. However, employing a fully nonlinear aerodynamic model in a design framework at this stage of development would be too computational expensive and not necessary. We then linearize the aerodynamic model about nonlinear operating points. Since the non-linearities are coming from the change in kinetic energy, we should pick the states describing the nonlinear operating point appropriately, so that the nonlinear change of these states can cope with the change in kinetic energy over the revolution. In this chapter, we then linearize the aerodynamic model about a nonlinear operating point.

6.1 Operating point

The state vector for the evaluation of the aerodynamic forces is

$$\boldsymbol{y} = \big[\underbrace{u,\ v,\ w}_{\boldsymbol{v}},\ \underbrace{p,\ q,\ r}_{\boldsymbol{\omega}},\ \underbrace{\phi,\ \theta,\ \psi}_{\boldsymbol{eu}},\ \underbrace{C_{L,al},\ \theta_h,\ \theta_v,\ a_t}_{\boldsymbol{u}}\big]^T, \tag{6.1}$$

where $\boldsymbol{v}$ and $\boldsymbol{\omega}$ are the linear and angular velocity of $\mathcal{F}_S$ with respect $\mathcal{F}_G$, expressed in $\mathcal{F}_S$, $\boldsymbol{eu}$ define the rotational matrix $\mathbf{R}_{RS}^{R}$ (Eq. 5.2) and $\boldsymbol{u}$ are the control inputs. $C_{L,al}$ is the increment in lift coefficient provided by a deflection of the ailerons, θ_h and θ_v

are the pitch angle of the horizontal and vertical stabilizers and a_t is the onboard wind turbine axial induction.

To make the state vector $\boldsymbol{y}$ non-dimensional, we introduce a diagonal matrix as

$$\mathbf{S}_{\boldsymbol{y}} = diag\left(\left[u_0,\ u_0,\ u_0,\ \frac{2u_0}{b},\ \frac{2u_0}{c},\ \frac{2u_0}{b},\ 1,\ 1,\ 1,\ 1,\ 1,\ 1,\ 1\right]\right). \tag{6.2}$$

where b is the wing span and c the reference chord.

We use the inverse of $\mathbf{S}_{\boldsymbol{y}}$ to define the non-dimensional state vector

$$\begin{aligned}\tilde{\boldsymbol{y}} = \mathbf{S}_{\boldsymbol{y}}^{-1}\boldsymbol{y} &= \left[\frac{u}{u_0},\ \frac{v}{u_0},\ \frac{w}{u_0},\ \frac{pb}{2u_0},\ \frac{qc}{2u_0},\ \frac{rb}{2u_0},\ \phi,\ \theta,\ \psi,\ C_{L,al},\ \theta_h,\ \theta_v,\ a_t\right]^T \\ &= \Big[\underbrace{\tilde{u},\ \tilde{v},\ \tilde{w}}_{\tilde{\boldsymbol{v}}},\ \underbrace{\tilde{p},\ \tilde{q},\ \tilde{r}}_{\tilde{\boldsymbol{\omega}}},\ \underbrace{\phi,\ \theta,\ \psi}_{\boldsymbol{eu}},\ \underbrace{C_{L,al},\ \theta_h,\ \theta_v,\ a_t}_{\boldsymbol{u}}\Big]^T.\end{aligned} \tag{6.3}$$

We now write the dimensional aerodynamic forces in $\mathcal{F}_S$ as

$$\boldsymbol{F}_a = \boldsymbol{F}_{a,0} + \frac{\partial \boldsymbol{F}_a}{\partial \tilde{\boldsymbol{y}}}\Delta\tilde{\boldsymbol{y}} \tag{6.4}$$

where in $\boldsymbol{F}_{a,0}$ we want to capture the nonlinear part of the aerodynamics and in $\frac{\partial \boldsymbol{F}_a}{\partial \tilde{\boldsymbol{y}}}\Delta\tilde{\boldsymbol{y}}$ the linear part.

To make the aerodynamic force non-dimensional, we consider the unit force $\mathbb{F}$

$$\mathbb{F} = \frac{1}{2}\rho A u_0^2, \tag{6.5}$$

and we introduce a diagonal matrix as

$$\mathbf{S} = diag\left([1,\ 1,\ 1,\ b,\ c,\ b]\right). \tag{6.6}$$

We can write the non-dimensional aerodynamic force vector as

$$\boldsymbol{f}_a = \frac{\mathbf{S}^{-1}}{\mathbb{F}}\boldsymbol{F}_a = \boldsymbol{f}_{a,0} + \frac{\partial \boldsymbol{f}_a}{\partial \tilde{\boldsymbol{y}}}\Delta\tilde{\boldsymbol{y}} \tag{6.7}$$

The nonlinear part of the aerodynamic force $\boldsymbol{f}_{a,0}$ is defined by the state

$$\boldsymbol{y}_0 = \left[u_0,\ 0,\ 0,\ 0,\ 0,\ r_0,\ 0,\ 0,\ 0,\ C_{L,al},\ \theta_h,\ \theta_v,\ a_t\right]^T. \tag{6.8}$$

Writing $r_0 = -\frac{u_0}{R_0}$ and thus $\frac{r_0 b}{2u_0} = -\frac{b}{2R_0} = -\kappa_0$, the non-dimensional state vector defining the nonlinear part of the aerodynamic force is

$$\tilde{\boldsymbol{y}}_0 = \left[1,\ 0,\ 0,\ 0,\ 0,\ -\kappa_0,\ 0,\ 0,\ 0,\ C_{L,al},\ \theta_h,\ \theta_v,\ a_t\right]^T. \tag{6.9}$$

The linear part of the aerodynamics is then defined by the incremental non-dimensional state

$$\Delta\tilde{\boldsymbol{y}} = \left[0,\ \tilde{v},\ \tilde{w},\ \tilde{p},\ \tilde{q},\ 0,\ \phi,\ \theta,\ \psi\right]^T. \tag{6.10}$$

In the next sections, we will compute the nonlinear force at the operating point $\boldsymbol{f}_{a,0}$ and take derivatives of the aerodynamic forces with respect to nine nondimensional states $\frac{\partial \boldsymbol{f}_a}{\partial \tilde{\boldsymbol{y}}}$: three linear velocities $\tilde{\boldsymbol{v}}$, three angular rates $\tilde{\boldsymbol{\omega}}$, and three angles $\boldsymbol{eu}$.

6.2 Angular velocity

As we want to linearize the aerodynamic forces about the operating point $\boldsymbol{y}_0$, the Euler angles $\boldsymbol{eu} = [\phi, \theta, \psi]^T$ are assumed to be small and $\mathbf{R}^R_{RS}(\phi, \theta, \psi)$ (Eq. 5.2) is linearized, so that

$$\mathbf{R}_{RS}(\phi, \theta, \psi) \approx \begin{bmatrix} 1 & -\psi & \theta \\ \psi & 1 & -\phi \\ -\theta & \phi & 1 \end{bmatrix} = \mathbf{1} + \begin{bmatrix} \phi \\ \theta \\ \psi \end{bmatrix}^{\times} = \mathbf{1} + \boldsymbol{eu}^{\times}, \tag{6.11}$$

where $\mathbf{1}$ is a 3 by 3 identity matrix and the symbol $(\cdot)^{\times}$ applied to a vector represents its corresponding skew-symmetric tensor form. Considering this linearization, $\mathbf{R}_{SR} = \mathbf{R}^T_{RS} = \mathbf{1} - \boldsymbol{eu}^{\times}$.

The angular velocity of $\mathcal{F}_S$ with respect to $\mathcal{F}_G$, expressed in $\mathcal{F}_S$ takes the form

$$\boldsymbol{\omega} \equiv [p, q, r]^T = \boldsymbol{\omega}^S_{GS} \approx \mathbf{R}^R_{SR}\boldsymbol{\omega}^R_{GR} + \dot{\boldsymbol{eu}} = (\mathbf{1} - \boldsymbol{eu}^{\times})\boldsymbol{\omega}^R_{GR} + \dot{\boldsymbol{eu}}. \tag{6.12}$$

6.3 Apparent wind speed

The wind velocity is along the $\boldsymbol{e}_{3,g}$ axis and has a negative direction. The aerodynamic induction due to the far wake a_f is considered constant over the trajectory and it is subtracted to the incoming wind speed.

The definition of the wind speed in the near wake, expressed in the stability coordinate system, can be written as

$$\boldsymbol{v}^S_w = \mathbf{R}^G_{SG} \begin{bmatrix} 0 \\ 0 \\ -v_w(1 - a_f) \end{bmatrix} = -v_w(1 - a_f) \begin{bmatrix} -\theta \\ \phi \\ 1 \end{bmatrix}. \tag{6.13}$$

By considering a generic position in $\mathcal{F}_S$, namely $\boldsymbol{x}^S = [x, y, z]^T$, the undisturbed apparent wind speed $\boldsymbol{v}^S_a$ in $\mathcal{F}_S$ is defined as the subtraction of the plane motion from the wind velocity, yielding

$$\boldsymbol{v}^S_a \equiv -\begin{bmatrix} \mathcal{U} \\ \mathcal{V} \\ \mathcal{W} \end{bmatrix} = \boldsymbol{v}^S_w - \boldsymbol{v} - \boldsymbol{\omega}^{\times}\boldsymbol{x}^S = -v_w(1 - a_f) \begin{bmatrix} -\theta \\ \phi \\ 1 \end{bmatrix} - \begin{bmatrix} u + zq - yr \\ v + xr - zp \\ w + yp - xq \end{bmatrix}, \tag{6.14}$$

where $\boldsymbol{v} \equiv [u, v, w]^T = \boldsymbol{v}^S_{GS}$ is the velocity of $\mathcal{F}_S$ with respect to $\mathcal{F}_G$, expressed in $\mathcal{F}_S$. The operating state is indicated with the subscript 0, therefore yielding for the baseline condition

$$\boldsymbol{v}^S_{a,0} = -\begin{bmatrix} \mathcal{U}_0 \\ \mathcal{V}_0 \\ \mathcal{W}_0 \end{bmatrix} = -v_w(1 - a_f) \begin{bmatrix} 0 \\ 0 \\ 1 \end{bmatrix} - \begin{bmatrix} u_0 - yr_0 \\ xr_0 \\ 0 \end{bmatrix} = -u_0 \begin{bmatrix} 1 + \eta \\ -\xi \\ \frac{1}{\lambda_n} \end{bmatrix}, \tag{6.15}$$

where u_0 is the plane velocity along $\boldsymbol{e}_{1,s}$ at the operating point, $r_0 = -\frac{u_0}{R_0}$, $\xi = \frac{x}{R_0}$, $\eta = \frac{y}{R_0}$ and λ_n is the wing speed ratio of the near wake, defined as

$$\lambda_n = \frac{u_0}{v_w(1 - a_f)} = \frac{\lambda}{1 - a_f}. \tag{6.16}$$

6.4 Main wing

The main wing is assumed to have an elliptic planform with no twist. Wing dihedral and sweep are considered small. The squared wing span is considered small compared to the turning radius squared, or in analytic terms, $\left(\frac{b}{2R_0}\right)^2 = \kappa_0^2 \ll 1$. To make the notation compact, the index "w" is avoided in this section.

6.4.1 Wing coordinate system

Dihedral angle Γ and sweep angle Λ are expected to influence the windplane stability. Therefore, aerodynamic derivatives shall consider these angles. $\mathcal{F}_{Wr}$, a reference system attached to the wing, is defined to be with the $\boldsymbol{e}_{2,wr}$ along the quarter chord line, pointing to the tip of the right wing, as in Figure 6.1. The rotation matrix between $\mathcal{F}_S$ and $\mathcal{F}_{Wr}$ is defined by applying first a rotation around $\boldsymbol{e}_{1,s}$ of Γ (i.e. the dihedral angle), followed by a rotation around the third axis of intensity Λ (i.e. sweep). This yields

$$\mathbf{R}_{S\to Wr}(\Gamma,\Lambda) = \mathbf{R}^{S}_{x,SS'}(\Gamma)\,\mathbf{R}^{S'}_{z,S'Wr}(\Lambda) \approx \mathbf{1} + \boldsymbol{ds}^{\times}, \tag{6.17}$$

where sweep and dihedral angles are assumed to be small and $\boldsymbol{ds} = [\Gamma, 0, \Lambda]^T$. Note that Γ is positive with the right wing pointing down, and Λ is positive with the right wing pointing backwards.

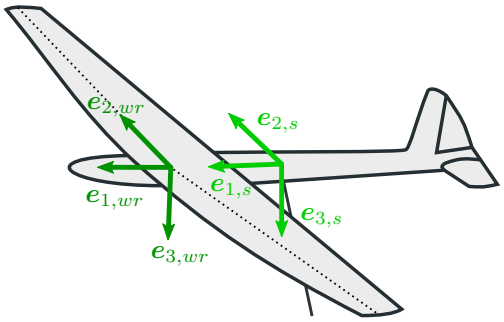

Figure 6.1: *Right wing coordinate system $\mathcal{F}_{Wr}$ and stability coordinate system $\mathcal{F}_S$.*

The coordinate system of the left wing $\mathcal{F}_{Wl}$ can be defined in similar manner. The rotational matrix from $\mathcal{F}_S$ to $\mathcal{F}_{Wl}$ is

$$\mathbf{R}_{S\to Wl}(\Gamma,\Lambda) \approx \mathbf{1} - \boldsymbol{ds}^{\times}. \tag{6.18}$$

The rotational matrices of the two wings can be unified as follows

$$\mathbf{R}_{S\to W}(\Gamma,\Lambda) = \mathbf{1} + \frac{y}{|y|}\boldsymbol{ds}^{\times}, \tag{6.19}$$

where $\frac{y}{|y|} = \frac{y}{|y|}\frac{R_0}{R_0} = \frac{\eta}{|\eta|}$ is the signum function of the wing span coordinate, over the full left and right wing span.

A given position along the wing axis $\boldsymbol{e}_{2,w}$ with respect to the tether attachment can be expressed in $\mathcal{F}_S$ as

$$\boldsymbol{tw}^S = \boldsymbol{tw}_0^S + \mathbf{R}_{SW}\begin{bmatrix}0\\ y_w\\ 0\end{bmatrix} = \begin{bmatrix}tw_x\\ 0\\ tw_z\end{bmatrix} + \begin{bmatrix}0\\ y_w\\ 0\end{bmatrix} + \frac{y_w}{|y_w|}y_w\begin{bmatrix}-\Lambda\\ 0\\ \Gamma\end{bmatrix}, \tag{6.20}$$

where $\boldsymbol{tw}_0$ is the position of the wing root with respect to the tether attachment.

6.4.2 Apparent wind speed in $\mathcal{F}_W$

The aerodynamic forces are evaluated in the wing coordinate system. Thus, the apparent wind speed in the wing coordinate system $\mathcal{F}_W$ is

$$\boldsymbol{v}_a^W = \mathbf{R}_{WS}\boldsymbol{v}_a^S = \boldsymbol{v}_a^S - \frac{\eta}{|\eta|}\boldsymbol{ds}^{\times}\boldsymbol{v}_a^S = -\begin{bmatrix}\mathcal{U}\\ \mathcal{V}\\ \mathcal{W}\end{bmatrix} - \frac{\eta}{|\eta|}\begin{bmatrix}\Lambda\mathcal{V}\\ -\Lambda\mathcal{U}+\Gamma\mathcal{W}\\ -\Gamma\mathcal{V}\end{bmatrix}, \tag{6.21}$$

where the apparent velocity $\boldsymbol{v}_a^S$ and its components are defined in Eq. (6.14). Note that (x, y, z) in Eq. (6.14) are still the coordinates in $\mathcal{F}_S$. Therefore, $\boldsymbol{v}_a^W$ is the apparent wind velocity in $\mathcal{F}_W$ given a point in the $\mathcal{F}_S$.

For the cross-flow principle, only the components on the $\boldsymbol{e}_{1,w}$ and $\boldsymbol{e}_{3,w}$ axes produce aerodynamic forces. Thus, the apparent velocity in the wing coordinate system, needed for the evaluation of aerodynamic forces, does not take into account the component along the $\boldsymbol{e}_{2,w}$ axis. The modulus of the apparent speed squared is then written as the summation of the first and third rows of Eq. (6.21) squared

$$v_a^2 = \left(-\mathcal{U} - \frac{\eta}{|\eta|}\Lambda\mathcal{V}\right)^2 + \left(-\mathcal{W} + \frac{\eta}{|\eta|}\Gamma\mathcal{V}\right)^2 \approx \mathcal{U}^2 + \mathcal{W}^2 - 2\frac{\eta}{|\eta|}\Gamma\mathcal{V}\mathcal{W} + 2\frac{\eta}{|\eta|}\Lambda\mathcal{U}\mathcal{V}, \tag{6.22}$$

where terms proportional to the sweep and dihedral squared are neglected (small higher order terms). Note that the two first terms are not dependent on the dihedral and sweep, so they are the only surviving results for a straight wing.

The inflow angle γ_n in the near wake, assumed to be small, is defined as the angle between the apparent velocity and the $\boldsymbol{e}_{1,w}$ axis measured in the $(\boldsymbol{e}_{1,w}, \boldsymbol{e}_{3,w})$ plane (see Fig 6.2 for a straight wing). Angle γ_n is used to project lift and drag in $\mathcal{F}_W$; it can be written as the ratio between the third and the first row of Eq. (6.21)

$$\begin{aligned}\gamma_n = \frac{\left(-\mathcal{W} + \frac{\eta}{|\eta|}\Gamma\mathcal{V}\right)}{\left(-\mathcal{U} - \frac{\eta}{|\eta|}\Lambda\mathcal{V}\right)} &= \frac{\mathcal{W}}{\mathcal{U}}\frac{\left(1 + \frac{\eta}{|\eta|}\Gamma\frac{\mathcal{V}}{-\mathcal{W}}\right)}{\left(1 - \frac{\eta}{|\eta|}\Lambda\frac{\mathcal{V}}{-\mathcal{U}}\right)}\frac{\left(1 + \frac{\eta}{|\eta|}\Lambda\frac{\mathcal{V}}{-\mathcal{U}}\right)}{\left(1 + \frac{\eta}{|\eta|}\Lambda\frac{\mathcal{V}}{-\mathcal{U}}\right)}\\ &\approx \frac{\mathcal{W}}{\mathcal{U}} - \Gamma\frac{\eta}{|\eta|}\frac{\mathcal{V}}{\mathcal{U}} - \Lambda\frac{\eta}{|\eta|}\frac{\mathcal{W}\mathcal{V}}{\mathcal{U}^2},\end{aligned} \tag{6.23}$$

where the first term is for a straight wing and the odd functions take into account wing geometry. Terms proportional to the sweep and dihedral squared are neglected (small higher order terms).

6.4.3 Angle of attack

The angle of attack is evaluated in the body coordinate system. Thus, the apparent wind speed in the body coordinate system $\mathcal{F}_B$ is

$$\boldsymbol{v}_a^B = \mathbf{R}_{BS}\boldsymbol{v}_a^S = -\begin{bmatrix}\cos\theta_{bs} & 0 & \sin\theta_{bs}\\ 0 & 1 & 0\\ -\sin\theta_{bs} & 0 & \cos\theta_{bs}\end{bmatrix}\begin{bmatrix}\mathcal{U}\\ \mathcal{V}\\ \mathcal{W}\end{bmatrix}, \tag{6.24}$$

The angle of attack α is the ratio between the third velocity component of $\boldsymbol{v}_a^B$ and the first

$$\alpha = \frac{-\mathcal{U}\sin\theta_{bs} + \mathcal{W}\cos\theta_{bs}}{\mathcal{U}\cos\theta_{bs} + \mathcal{W}\sin\theta_{bs}} \approx \frac{\mathcal{W}}{\mathcal{U}} - \tan\theta_{bs}. \tag{6.25}$$

6.4.4 Operating point

At the operating point, the apparent velocity, using Eq. (6.22), and the inflow angle, using Eq. (6.23), take the forms

$$v_{a,0}^2 \approx u_0^2\,(1+\eta)^2 \approx u_0^2\,(1+2\eta)\,, \qquad \gamma_{n,0} \approx \frac{1}{\lambda_n\,(1+\eta)} \approx \frac{1}{\lambda_n}\,(1-\eta)\,, \tag{6.26}$$

where the assumption $\eta^2 = \left(\frac{y}{R_0}\right)^2 \ll 1$ has been invoked and terms proportional to sweep and dihedral angle neglected. Both the apparent velocity squared and inflow angle are linear functions of η.

The angle of attack α_0 at the operating point at the mid span airfoil is derived from Eq. (6.25)

$$\alpha_0 \approx \frac{1}{\lambda_n} - \theta_{bs} \tag{6.27}$$

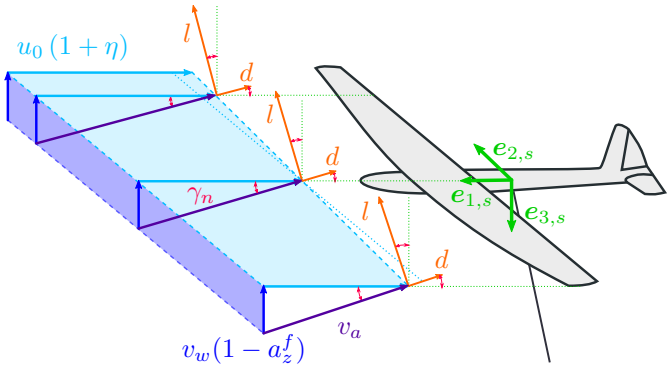

Figure 6.2: *Velocity triangle and aerodynamic forces for the main wing.*

Considering strip theory (Nelson (1998)), the aerodynamic lift coefficient in the $\mathcal{F}_W$ at a given y_w position of the wing is computed as

$$C_L(y_w) = C_L(y) = C_L(y=0) + C_{L\alpha}\frac{\partial\alpha}{\partial y}y = C_L(y=0) - C_{L\alpha}\frac{\eta}{\lambda_n}, \tag{6.28}$$

where $C_{L\alpha}$ can be computed from the airfoil lift coefficient slope $C_{l\alpha}$ and $\frac{\partial\alpha}{\partial y} = \frac{\partial\gamma_n}{\partial y} \approx -\frac{1}{R_0\lambda_n}$

$$C_{L\alpha} = \frac{C_{l\alpha}}{1 + \frac{C_{l\alpha}}{\pi AR}}, \tag{6.29}$$

which is a good approximation for an elliptic wing with no twist. A similar procedure can be applied to the drag coefficient, such that $C_D(y) = C_D(y=0) - C_{D\alpha}\frac{\eta}{\lambda_n}$, where $C_D(y=0)$ and $C_{D\alpha}$ can be found with lifting line theory

$$C_D(y=0) = C_{d0} + k_d C_L(y=0)^2 + \frac{C_L^2(y=0)}{\pi AR}, \tag{6.30}$$

and

$$C_{D\alpha} = 2k_d C_L(y=0) C_{L\alpha} + 2\frac{C_L(y=0)C_{L\alpha}}{\pi AR} \tag{6.31}$$

No dependence of the lift coefficient on the side slip angle is considered. From now on, $C_L(y=0)$ will be indicated as C_L and $C_D(y=0)$ as C_D.

Given this modeling, the non-dimensional aerodynamic forces given by the main wing can be written as

$$\boldsymbol{f} = \int_{-b/2}^{b/2} \frac{1}{2}\rho\, c(y) \frac{\mathbf{S}^{-1}}{\mathtt{F}} \begin{bmatrix} \mathbf{1} \\ \boldsymbol{tw}^{\times} \end{bmatrix} \mathbf{R}_{SW} \begin{bmatrix} C_L(y)\gamma_n(y) - C_D(y) \\ 0 \\ -C_L(y) \end{bmatrix} v_a(y)^2 dy, \tag{6.32}$$

where the apparent wind velocity squared $v_a(y)^2$ (Eq. (6.22)) and the aerodynamic coefficients matrix $\mathbf{C} = [C_L(y)\gamma_n(y) - C_D(y), 0, -C_L(y)]^T$ are computed in $\mathcal{F}_W$, therefore $\mathbf{R}_{SW}$ (Eq (6.19)) brings them into $\mathcal{F}_S$, where the integration happens. The term $C_L(y)\gamma_n(y)$ in the aerodynamic coefficient matrix models the propulsive lift. The term $\boldsymbol{tw}^{\times}$ indicates the skew symmetric matrix of the application location of the aerodynamic forces in $\mathcal{F}_S$ and it is needed to compute moments. The matrix $\mathbf{S}^{-1}$ (Eq. (6.6)) brings moments into forces, the unit force $\mathtt{F}$ (Eq. (6.5)) makes the equation non dimensional and $c(y)$ is the chord.

To get to a closed form solution of the integral, the odd functions of the wing span coordinate in the integral variable are to be separated from those which are even or constant. The first part of the integral function of Eq. (6.32) can be written using Eq. (6.20) and identity $\mathbf{R}_{SW} = \mathbf{1} + \frac{\eta}{|\eta|}\boldsymbol{ds}^{\times}$ (Eq. (6.19))

$$\begin{aligned}\mathbf{S}^{-1} \begin{bmatrix} \mathbf{1} \\ \boldsymbol{tw}^{\times} \end{bmatrix} \mathbf{R}_{SW} = \mathbf{S}^{-1}\Bigg(& \begin{bmatrix} \mathbf{1} \\ [tw_x, 0, tw_z]^{\times} \end{bmatrix} + \eta \begin{bmatrix} \mathbf{0} \\ [0, R_0, 0]^{\times} \end{bmatrix} \\ & + \eta\frac{\eta}{|\eta|} \begin{bmatrix} \mathbf{0} \\ (\boldsymbol{ds}^{\times}[0, R_0, 0]^T)^{\times} \end{bmatrix} + \frac{\eta}{|\eta|} \begin{bmatrix} \boldsymbol{ds}^{\times} \\ [tw_x, 0, tw_z]^{\times}\boldsymbol{ds}^{\times} \end{bmatrix} \\ & + \eta\frac{\eta}{|\eta|} \begin{bmatrix} \mathbf{0} \\ [0, R_0, 0]^{\times}\boldsymbol{ds}^{\times} \end{bmatrix} + \eta\frac{\eta^2}{|\eta|^2} \begin{bmatrix} \mathbf{0} \\ (\boldsymbol{ds}^{\times}[0, R_0, 0]^T)^{\times}\boldsymbol{ds}^{\times} \end{bmatrix} \Bigg).\end{aligned} \tag{6.33}$$

The very last term, including effects proportional to dihedral and sweep squared, can be neglected. Also the second last term can be left out, since the aerodynamic loads are only in the first and third axes [1]. With these two considerations, Eq (6.33) can be written highlighting the dependence on the wing span non-dimensional coordinate η

$$\begin{aligned}\mathbf{S}^{-1} \begin{bmatrix} \mathbf{1} \\ \boldsymbol{tw}^{\times} \end{bmatrix} \mathbf{R}_{SW} \approx \mathbf{S}^{-1} & \left(\begin{bmatrix} \mathbf{1} \\ [tw_x, 0, tw_z]^{\times} \end{bmatrix} + \eta\frac{\eta}{|\eta|} \begin{bmatrix} \mathbf{0} \\ (\boldsymbol{ds}^{\times}[0, R_0, 0]^T)^{\times} \end{bmatrix} \right) \\ & + \eta\mathbf{S}^{-1} \left(\begin{bmatrix} \mathbf{0} \\ [0, R_0, 0]^{\times} \end{bmatrix} + \frac{1}{|\eta|} \begin{bmatrix} \boldsymbol{ds}^{\times} \\ [tw_x, 0, tw_z]^{\times}\boldsymbol{ds}^{\times} \end{bmatrix} \right) \equiv \mathbf{P} + \eta\mathbf{D},\end{aligned} \tag{6.34}$$

where $\mathbf{P}$ and $\mathbf{D}$ are even functions of η.

[1] $[0, R_0, 0]^{\times}\boldsymbol{ds}^{\times}[C_x, 0, C_z]^T = [0, R_0, 0]^T \times ([\Gamma, 0, \Lambda]^T \times [C_x, 0, C_z]^T) = [0, R_0, 0]^T \times [0, \Lambda C_x - \Gamma C_z, 0] = 0.$

For readability, the following matrices, derived in Appendix B.1, are defined

$$\mathbf{P}_A \equiv \frac{1}{A}\int_{-b/2}^{b/2} c(y)\mathbf{P}dy, \qquad \mathbf{P}_\eta \equiv \frac{1}{A}\int_{-b/2}^{b/2} c(y)\frac{\eta^2}{|\eta|}\mathbf{P}dy, \qquad \mathbf{P}_{\eta\eta} \equiv \frac{1}{A}\int_{-b/2}^{b/2} c(y)\eta^2\mathbf{P}dy,$$
$$\mathbf{D}_\eta \equiv \frac{1}{A}\int_{-b/2}^{b/2} c(y)\frac{\eta^2}{|\eta|}\mathbf{D}dy, \qquad \mathbf{D}_{\eta\eta} \equiv \frac{1}{A}\int_{-b/2}^{b/2} c(y)\eta^2\mathbf{D}dy. \tag{6.35}$$

The aerodynamic coefficient matrix at trim $\mathbf{C}_0$, where $\mathbf{C}$ is introduced in Eq. (6.32), is

$$\begin{aligned}\mathbf{C}_0 &= \begin{bmatrix} C_L(y)\gamma_{n,0}(y) - C_D(y) \\ 0 \\ -C_L(y) \end{bmatrix} \approx \begin{bmatrix} \frac{C_L}{\lambda_n} - C_D \\ 0 \\ -C_L \end{bmatrix} - \frac{\eta}{\lambda_n}\begin{bmatrix} C_L + \frac{C_{L\alpha}}{\lambda_n} - C_{D\alpha} \\ 0 \\ -C_{L\alpha} \end{bmatrix} \\ &= \mathbf{C}_{R_0} - \eta\frac{\mathbf{C}_\eta}{\lambda_n},\end{aligned} \tag{6.36}$$

where $\gamma_{n,0}(y)$ is given in Eq. (6.26) and $C_L(y)$ in Eq. (6.28). The definition of $\mathbf{C}_{R_0}$ and $\mathbf{C}_\eta$ is useful when performing derivatives with respect to a generic state variable $\tilde{y}_j$ of the state vector (Eq. (6.3))

$$\begin{aligned}\frac{\partial \mathbf{C}}{\partial \tilde{y}_j} &= \begin{bmatrix} C_{L\alpha}\gamma_{n,0}(y) - C_{D\alpha} \\ 0 \\ -C_{L\alpha} \end{bmatrix}\frac{\partial \alpha}{\partial \tilde{y}_j} + \begin{bmatrix} C_L - \frac{\eta}{\lambda_n}C_{L\alpha} \\ 0 \\ 0 \end{bmatrix}\frac{\partial \gamma_n}{\partial \tilde{y}_j} \\ &= \left(\begin{bmatrix} C_L + \frac{C_{L\alpha}}{\lambda_n} - C_{D\alpha} \\ 0 \\ -C_{L\alpha} \end{bmatrix} - 2\eta\begin{bmatrix} \frac{C_{L\alpha}}{\lambda_n} \\ 0 \\ 0 \end{bmatrix}\right)\frac{\partial \gamma_n}{\partial \tilde{y}_j} = \left(\mathbf{C}_\eta - 2\eta\mathbf{C}_{L\alpha}\right)\frac{\partial \gamma_n}{\partial \tilde{y}_j},\end{aligned} \tag{6.37}$$

where the derivative of the angle of attack with respect to a generic variable is equal to the derivative of the inflow angle with respect to the same variable $\frac{\partial \alpha}{\partial \tilde{y}_j} = \frac{\partial \gamma_n}{\partial \tilde{y}_j}$. The three new aerodynamic coefficient matrices, defined to highlight the dependence of the aerodynamic coefficient matrix at trim $\mathbf{C}_0$ (Eq. (6.36)) and of its derivative $\frac{\partial \mathbf{C}}{\partial \tilde{y}_j}$ (Eq. (6.37)) with respect to η are

$$\mathbf{C}_{R_0} = \begin{bmatrix} \frac{C_L}{\lambda_n} - C_D \\ 0 \\ -C_L \end{bmatrix}, \qquad \mathbf{C}_\eta = \begin{bmatrix} C_L + \frac{C_{L\alpha}}{\lambda_n} - C_{D\alpha} \\ 0 \\ -C_{L\alpha} \end{bmatrix}, \qquad \mathbf{C}_{L\alpha} = \begin{bmatrix} \frac{C_{L\alpha}}{\lambda_n} \\ 0 \\ 0 \end{bmatrix}. \tag{6.38}$$

Deleting the odd functions of y, which provide a null contribution along the wingspan, the following form for non-dimensional force and moment at the operating point is ob-

tained

$$\begin{aligned}\boldsymbol{f}_{w,0} &= \frac{1}{\mathrm{F}}\frac{1}{2}\rho\int_{-b/2}^{b/2} c(y)\left(\mathbf{P}+\eta\mathbf{D}\right)\left(\mathbf{C}_{R_0}-\eta\frac{\mathbf{C}_\eta}{\lambda_n}\right)u_0^2\left(1+\eta\right)^2 dy \\ &\approx \frac{1}{A}\int_{-b/2}^{b/2} c(y)\left(\mathbf{P}+\eta\mathbf{D}\right)\left(\mathbf{C}_{R_0}+\eta\left(2\mathbf{C}_{R_0}-\frac{\mathbf{C}_\eta}{\lambda_n}\right)\right)dy \\ &= \mathbf{P}_A\mathbf{C}_{R_0}+\mathbf{D}_{\eta\eta}\left(2\mathbf{C}_{R_0}-\frac{\mathbf{C}_\eta}{\lambda_n}\right).\end{aligned} \tag{6.39}$$

$\boldsymbol{f}_{w,0}$ can be written explicitly as

$$\begin{aligned}\boldsymbol{f}_{w,0} = \begin{bmatrix}\tilde{X}_{w,0}\\ \tilde{Y}_{w,0}\\ \tilde{Z}_{w,0}\\ \tilde{L}_{w,0}\\ \tilde{M}_{w,0}\\ \tilde{N}_{w,0}\end{bmatrix} &= \begin{bmatrix}1 & 0\\ 0 & 0\\ 0 & 1\\ 0 & 0\\ \frac{tw_z}{c}-\Gamma\frac{y_\eta}{c} & -\frac{tw_x}{c}-\Lambda\frac{y_\eta}{c}\\ 0 & 0\end{bmatrix}\begin{bmatrix}\frac{C_L}{\lambda_n}-C_D\\ -C_L\end{bmatrix} \\ &+\left(\frac{I_{\eta\eta}}{A}\begin{bmatrix}0&0\\0&0\\0&0\\0&\frac{R_0}{b}\\0&0\\-\frac{R_0}{b}&0\end{bmatrix}+\frac{I_\eta}{A}\begin{bmatrix}0&0\\\Lambda&-\Gamma\\0&0\\-\Lambda\frac{tw_z}{b}&\Gamma\frac{tw_z}{b}\\0&0\\\Lambda\frac{tw_x}{b}&-\Gamma\frac{tw_x}{b}\end{bmatrix}\right)\begin{bmatrix}\frac{C_L}{\lambda_n}-2C_D-\frac{C_{L\alpha}}{\lambda_n^2}+\frac{C_{D\alpha}}{\lambda_n}\\ -2C_L+\frac{C_{L\alpha}}{\lambda_n}\end{bmatrix}.\end{aligned} \tag{6.40}$$

The non dimensional aerodynamic force component $\tilde{X}_{w,0}$ is equal to the propulsive lift minus the drag. $\tilde{Y}_{w,0}$ appears just because of the dihedral angle Γ and sweep Λ and the difference in apparent wind speed between the inner and outer wing. Indeed, loads in the two wings are different and so is their projection on the $\boldsymbol{e}_{2,s}$ axis. . $\tilde{Z}_{w,0}$ is just function of the lift coefficient. The moments $\tilde{L}_{w,0}$ and $\tilde{N}_{w,0}$ appear because of the difference in apparent wind speed between an inner and outer wing. It is also noteworthy that $\tilde{M}_{w,0}$ basically does not depend on dihedral nor sweep.

In Appendix B, we go through the steps to compute derivatives of the aerodynamic forces and moments with respect to the non-dimensional state vector $\tilde{\boldsymbol{y}}$. Table 6.1 summarizes all the non-null derivatives for the case of a straight wing. The passages leading to these forms are provided in Appendix B.3. In Table 6.2 all the non-null derivatives due to sweep and dihedral angle are reported. The passages leading to the results presented here are given in Appendix B.4.

6.5 Ailerons

Equation 6.40 shows that the linear variation of the apparent wind and of the inflow angle are generating a roll moment L in the operating condition. A control strategy to control the roll axis of windplanes could be based on the use of ailerons, as shown in Figure 6.3. For this reason, it is especially interesting to model the effect of ailerons on

$\frac{\partial \boldsymbol{f}_w}{\partial \tilde{u}}$	$\mathbf{P}_A \left(2\mathbf{C}_{w,R_0} - \frac{\mathbf{C}_{w,\eta}}{\lambda_n}\right) + 2\mathbf{D}_{\eta\eta} \left(\mathbf{C}_{w,R_0} - \frac{\mathbf{C}_{w,\eta}}{\lambda_n} + \frac{\mathbf{C}_{w,L\alpha}}{\lambda_n}\right)$
$\frac{\partial \boldsymbol{f}_w}{\partial \tilde{w}}$	$\mathbf{P}_A \left(\mathbf{C}_{w,\eta} + 2\frac{\mathbf{C}_{w,R_0}}{\lambda_n}\right) + \mathbf{D}_{\eta\eta} \left(\mathbf{C}_{w,\eta} - 2\mathbf{C}_{w,L\alpha}\right)$
$\frac{\partial \boldsymbol{f}_w}{\partial \tilde{p}}$	$\frac{R_0}{b/2} \left[\mathbf{P}_{\eta\eta} \left(\mathbf{C}_{w,\eta} - 2\mathbf{C}_{w,L\alpha}\right) + \mathbf{D}_{\eta\eta} \left(\mathbf{C}_{w,\eta} + 2\frac{\mathbf{C}_{w,R_0}}{\lambda_n}\right)\right]$
$\frac{\partial \boldsymbol{f}_w}{\partial \tilde{q}}$	$\frac{\mathbf{P}_{A,z}}{c/2} \left[2\mathbf{C}_{w,R_0} - \frac{\mathbf{C}_{w,\eta}}{\lambda_n}\right] - \frac{\mathbf{P}_{A,x}}{c/2} \left[\mathbf{C}_{w,\eta} + 2\frac{\mathbf{C}_{w,R_0}}{\lambda_n}\right] +$ $2\frac{\mathbf{D}_{\eta\eta,z}}{c/2} \left[\mathbf{C}_{w,R_0} - \frac{\mathbf{C}_{w,\eta}}{\lambda_n} + \frac{\mathbf{C}_{w,L\alpha}}{\lambda_n}\right] - \frac{\mathbf{D}_{\eta\eta,x}}{c/2} \left[\mathbf{C}_{w,\eta} - 2\mathbf{C}_{w,L\alpha}\right]$
$\frac{\partial \boldsymbol{f}_w}{\partial \tilde{r}}$	$-\frac{R_0}{b/2} \left[2\mathbf{P}_{\eta\eta} \left(\mathbf{C}_{w,R_0} - \frac{\mathbf{C}_{w,\eta}}{\lambda_n} + \frac{\mathbf{C}_{w,L\alpha}}{\lambda_n}\right) + \mathbf{D}_{\eta\eta} \left(2\mathbf{C}_{w,R_0} - \frac{\mathbf{C}_{w,\eta}}{\lambda_n}\right)\right]$
$\frac{\partial \boldsymbol{f}_w}{\partial \phi}$	$-\frac{c/2}{R_0} \frac{\partial \boldsymbol{f}_w}{\partial \tilde{q}}$
$\frac{\partial \boldsymbol{f}_w}{\partial \theta}$	$\mathbf{P}_A \mathbf{C}_{w,\eta} + 2\mathbf{D}_{\eta\eta} \left(\mathbf{C}_{w,\eta} - \mathbf{C}_{w,L\alpha}\right)$

Table 6.1: *Derivatives for the case of the straight main wing (the passages leading to these forms are provided in Appendix B.3).*

aerodynamics. This can be done again via strip theory, thus making use of most of the formulation already introduced. The corresponding control derivative, expressing the sensitivity of aerodynamic forces and moments to control variables, can be studied as follows.

By hypothesis, a relatively small sensitivity to aileron control can be considered, since the size of ailerons (hence their control authority) is generally limited compared to that of the wing. Furthermore, derivatives and forces at the operating point are computed neglecting the dihedral and sweep angle for simplicity and it is assumed that outside the wing sections where ailerons are deflected, the span-wise aerodynamic loading remains unaffected.

Assuming a symmetric displacement of the right and left ailerons, the force associ-

$\frac{\partial \boldsymbol{f}_w}{\partial \tilde{v}}$	$-\Gamma \left[\mathbf{P}_\eta \left(\mathbf{C}_{w,\eta} - 2\mathbf{C}_{w,L\alpha}\right) + \mathbf{D}_\eta \left(\mathbf{C}_{w,\eta} + 2\frac{\mathbf{C}_{w,R_0}}{\lambda_n}\right)\right]$ $+\Lambda \left[2\mathbf{P}_\eta \left(\mathbf{C}_{w,R_0} - \frac{\mathbf{C}_{w,\eta}}{\lambda_n} + \frac{\mathbf{C}_{w,L\alpha}}{\lambda_n}\right) + \mathbf{D}_\eta \left(2\mathbf{C}_{w,R_0} - \frac{\mathbf{C}_{w,\eta}}{\lambda_n}\right)\right]$
$\frac{\partial \boldsymbol{f}_w}{\partial \tilde{p}}$	$\Gamma \left[\frac{\mathbf{P}_{\eta z}}{b/2} \left(\mathbf{C}_{w,\eta} - 2\mathbf{C}_{w,L\alpha}\right) + \frac{\mathbf{D}_{\eta z}}{b/2} \left(\mathbf{C}_{w,\eta} + 2\frac{\mathbf{C}_{w,R_0}}{\lambda_n}\right)\right]$ $-\Lambda \left[2\frac{\mathbf{P}_{\eta z}}{b/2} \left(\mathbf{C}_{w,R_0} - \frac{\mathbf{C}_{w,\eta}}{\lambda_n} + \frac{\mathbf{C}_{w,L\alpha}}{\lambda_n}\right) + \frac{\mathbf{D}_{\eta z}}{b/2} \left(2\mathbf{C}_{w,R_0} - \frac{\mathbf{C}_{w,\eta}}{\lambda_n}\right)\right]$
$\frac{\partial \boldsymbol{f}_w}{\partial \tilde{r}}$	$-\Gamma \left[\frac{\mathbf{P}_{\eta x}}{b/2} \left(\mathbf{C}_{w,\eta} - 2\mathbf{C}_{w,L\alpha}\right) + \frac{\mathbf{D}_{\eta x}}{b/2} \left(\mathbf{C}_{w,\eta} + 2\frac{\mathbf{C}_{w,R_0}}{\lambda_n}\right)\right]$ $+\Lambda \left[2\frac{\mathbf{P}_{\eta x}}{b/2} \left(\mathbf{C}_{w,R_0} - \frac{\mathbf{C}_{w,\eta}}{\lambda_n} + \frac{\mathbf{C}_{w,L\alpha}}{\lambda_n}\right) + \frac{\mathbf{D}_{\eta x}}{b/2} \left(2\mathbf{C}_{w,R_0} - \frac{\mathbf{C}_{w,\eta}}{\lambda_n}\right)\right]$
$\frac{\partial \boldsymbol{f}_w}{\partial \phi}$	$\frac{1}{\lambda_n} \frac{\partial \boldsymbol{f}_w}{\partial \tilde{v}}\Big\vert_{\Gamma,\Lambda}$

Table 6.2: *Derivatives due to dihedral and sweep angle (The passages leading to the results presented here are given in Appendix B.4).*

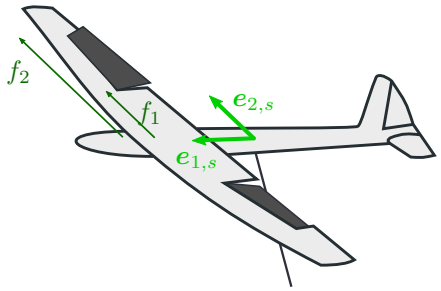

Figure 6.3: *Symmetrical ailerons deflection.*

ated to their deflection is

$$\boldsymbol{f}_{al} = \int_{-b/2}^{b/2} \frac{1}{2}\rho\, c(y) f_{al}(y) \frac{\mathbf{S}^{-1}}{\mathbb{F}} \begin{bmatrix} \mathbf{1} \\ \boldsymbol{tw}^{S\times} \end{bmatrix} \frac{\eta}{|\eta|} \begin{bmatrix} C_{L,al}\gamma_{w,n} - C_{D,al} \\ 0 \\ -C_{L,al} \end{bmatrix} v_a^2 dy, \tag{6.41}$$

where the function $f_{al}(y)$ takes a value of 1 along the portion of the wingspan between the aileron extremities

$$f_{al}(y) = \begin{cases} 0 & for\ |y| < f_1 \\ 1 & for\ f_1 < |y| < f_2 \\ 0 & for\ f_2 < |y| \end{cases}, \tag{6.42}$$

where f_1 and f_2 are shown in Fig. 6.3 and in this thesis we take $f_1 = 0.5$ and $f_2 = 0.8$.

Typically, $C_{L,al}$ and $C_{D,al}$ are provided as function of the ailerons deflections. We define the aerodynamic coefficient matrix $\mathbf{C}_a$

$$\mathbf{C}_{al} = \left[C_{L,al}\gamma_{w,n} - C_{D,al}, 0, -C_{L,al}\right]^T, \tag{6.43}$$

where $\gamma_{w,n}$ is the inflow angle at the main wing due to the near wake. Its value at the operating point is

$$\mathbf{C}_{al,0} \approx \begin{bmatrix} \frac{C_{L,al}}{\lambda_n} - C_{D,al} \\ 0 \\ -C_{L,al} \end{bmatrix} - \frac{\eta}{\lambda_n} \begin{bmatrix} C_{L,al} \\ 0 \\ 0 \end{bmatrix} = \mathbf{C}_{al,R_0} - \frac{\eta}{\lambda_n}\mathbf{C}_{al,\eta}. \tag{6.44}$$

Consequently, the derivative of the aerodynamic coefficient matrix can be written (according to the same procedure introduced for other force and moment derivatives) as

$$\frac{\partial \mathbf{C}_{al}}{\partial \tilde{y}_j} = \frac{\partial}{\partial \tilde{y}_j} \begin{bmatrix} C_{L,al}\gamma_{w,n} - C_{D,al} \\ 0 \\ -C_{Lal} \end{bmatrix} = \begin{bmatrix} C_{L,al} \\ 0 \\ 0 \end{bmatrix} \frac{\partial \gamma_{w,n}}{\partial \tilde{y}_j} = \mathbf{C}_{al,\eta} \frac{\partial \gamma_{w,n}}{\partial \tilde{y}_j}, \tag{6.45}$$

where it is assumed that $C_{L,al}$ and $C_{D,al}$ do not depend on the angle of attack. The force

vector due to the ailerons at the operating point is therefore

$$\begin{aligned}\boldsymbol{f}_{al,0} &= \frac{1}{A}\int_{-b/2}^{b/2} c(y) f_{al}(y) \frac{\eta}{|\eta|} \left(\mathbf{P}_{al} + \eta \mathbf{D}_{al}\right) \left(\mathbf{C}_{al,R_0} - \frac{\eta}{\lambda_n}\mathbf{C}_{al,\eta}\right)(1+2\eta)\, dy \\ &\approx \frac{I_{f\eta}}{A}\mathbf{P}_{al}\left(2\mathbf{C}_{al,R_0} - \frac{\mathbf{C}_{al,\eta}}{\lambda_n}\right) + \frac{I_{f\eta}}{A}\mathbf{D}_{al}\mathbf{C}_{al,R_0},\end{aligned} \tag{6.46}$$

where the new terms appearing in the latter expression are $\mathbf{P}_{al} = \mathbf{S}^{-1}\left[\mathbf{1}; [tw_x, 0, tw_z]^{\times}\right]$, $\mathbf{D}_{al} = \mathbf{S}^{-1}\left[\mathbf{0}; [0, R_0, 0]^{\times}\right]$ and $I_{f\eta} = \int_{-b/2}^{b/2} c(y) f_{al}(y) \frac{\eta}{|\eta|}\eta dy$.

In Table 6.3 the derivatives due to the ailerons are reported. In this thesis, the change in drag coefficient due to the change in lift coefficient due to ailerons $C_{D,al}$ is neglected. Note that $\frac{\partial \gamma_{w,n}}{\partial \tilde{y}_j}$ and $\frac{\partial v_a^2}{\partial \tilde{y}_j}$ are the same as for the straight wing case (Table B.1).

$\frac{\partial \boldsymbol{f}_{al}}{\partial \tilde{u}}$	$2\frac{I_{f\eta}}{A}\mathbf{P}_{al}\left(\mathbf{C}_{al,R_0} - \frac{\mathbf{C}_{al,\eta}}{\lambda_n}\right) + \frac{I_{f\eta}}{A}\mathbf{D}_{al}\left(2\mathbf{C}_{al,R_0} - \frac{\mathbf{C}_{al,\eta}}{\lambda_n}\right)$
$\frac{\partial \boldsymbol{f}_{al}}{\partial \tilde{w}}$	$\frac{I_{f\eta}}{A}\mathbf{P}_{al}\mathbf{C}_{al,\eta} + \frac{I_{f\eta}}{A}\mathbf{D}_{al}\left(\mathbf{C}_{al,\eta} + 2\frac{\mathbf{C}_{al,R_0}}{\lambda_n}\right)$
$\frac{\partial \boldsymbol{f}_{al}}{\partial \tilde{p}}$	$\frac{R_0}{b/2}\frac{I_{f\eta}}{A}\mathbf{P}_{al}\left(\mathbf{C}_{al,\eta} + 2\frac{\mathbf{C}_{al,R_0}}{\lambda_n}\right)$
$\frac{\partial \boldsymbol{f}_{al}}{\partial \tilde{q}}$	$\frac{tw_z}{c/2}\frac{\partial \boldsymbol{f}_{al}}{\partial \tilde{u}} - \frac{tw_x}{c/2}\frac{\partial \boldsymbol{f}_{al}}{\partial \tilde{w}}$
$\frac{\partial \boldsymbol{f}_{al}}{\partial \tilde{r}}$	$-\frac{R_0}{b/2}\frac{I_{f\eta}}{A}\mathbf{P}_{al}\left(2\mathbf{C}_{al,R_0} - \frac{\mathbf{C}_{al,\eta}}{\lambda_n}\right)$
$\frac{\partial \boldsymbol{f}_{al}}{\partial \phi}$	$-\frac{c/2}{R_0}\frac{\partial \boldsymbol{f}_{al}}{\partial \tilde{q}}$
$\frac{\partial \boldsymbol{f}_{al}}{\partial \theta}$	$2\frac{I_{f\eta}}{A}\mathbf{P}_{al}\mathbf{C}_{al,\eta} + \frac{I_{f\eta}}{A}\mathbf{D}_{al}\mathbf{C}_{al,\eta}$

Table 6.3: *Derivatives of the ailerons contribution.*

6.6 Horizontal tail

For the sake of simplicity, the horizontal tail surface is lumped at the symmetry plane of the aircraft. Thus, only the apparent wind velocity and the inflow angle at the mid-airfoil of the horizontal tail are to be considered. The inflow angle is the summation of the apparent wind speed (Eq. (6.14)) and of the downwash of the main wing

$$\gamma_h \approx \frac{\mathcal{W}}{\mathcal{U}} - \varepsilon_d = \gamma_h^* - \varepsilon_d, \tag{6.47}$$

where ε_d is evaluated using the formulation by Phillips et al. (2002), which models the downwash in the aft tail considering also the contribution of the main wing sweep, yielding

$$\varepsilon_d \approx \frac{\kappa_v \kappa_p \kappa_s}{\kappa_b}\frac{C_{L,w}}{AR_w}, \tag{6.48}$$

where AR_w is the main wing aspect ratio. For an elliptic wing, $\kappa_v = 1$, $\kappa_b = \frac{\pi}{4}$, and κ_p takes into account the aft tail position with respect to the main wing. Finally κ_s

models the effect of the main wing sweep on the downwash. Based on the model just introduced, the variation in the downwash angle for a change in the angle of attack of the main wing can be computed as

$$\varepsilon_{d,\alpha} = \frac{\partial \varepsilon_d}{\partial \alpha} = \frac{\kappa_v \kappa_p \kappa_s}{\kappa_b} \frac{C_{L\alpha,w}}{AR_w}. \tag{6.49}$$

The angle of attack α_h of the horizontal stabilizer is

$$\alpha_h = \gamma_h - \theta_{bs} + \theta_h, \tag{6.50}$$

where θ_h is the pitch of the horizontal stabilizer, measured as a rotation around $\boldsymbol{e}_{2,b}$.

The lift coefficient $C_{L,h}$ can be found as function of the angle of attack as

$$C_{L,h} = \frac{C_{l\alpha,h}}{1 + \frac{C_{l\alpha,h}}{\pi AR_h}} \alpha_h \tag{6.51}$$

and the drag coefficient $C_{D,h}$ as

$$C_{D,h} = C_{d,h,0} + k_{d,h} C_{L,h}^2 + \frac{C_{L,h}^2}{\pi AR_h}, \tag{6.52}$$

where $C_{d,h,0}$ and $k_{d,h}$ describe the airfoils polars.

The non-dimensional force given by the horizontal tail can be written as

$$\boldsymbol{f}_h = \frac{A_h}{A u_0^2} \mathbf{S}^{-1} \begin{bmatrix} \mathbf{1} \\ \boldsymbol{th}^\times \end{bmatrix} \begin{bmatrix} C_{L,h}\gamma_h - C_{D,h} \\ 0 \\ -C_{L,h} \end{bmatrix} v_a^2, \tag{6.53}$$

where A_h is the horizontal tail area. At the operating point $\boldsymbol{y}_0$, the aerodynamic force non-dimensional force given by the horizontal tail is

$$\boldsymbol{f}_{h,0} = \frac{A_h}{A} \mathbf{P}_h \mathbf{C}_h. \tag{6.54}$$

where $\mathbf{P}_h = \mathbf{S}^{-1} \left[\mathbf{1}; \boldsymbol{th}^\times\right]$ and $\mathbf{C}_h = \left[C_{L,h}\gamma_h - C_{D,h}, 0, -C_{L,h}\right]^T$.

The derivative of the force with respect to a generic variable $\tilde{y}_j$ is

$$\frac{\partial \boldsymbol{f}_h}{\partial \tilde{y}_j} = \frac{\partial}{\partial \tilde{y}_j} \left\{ \frac{A_h}{A u_0^2} \mathbf{P}_h \mathbf{C}_h v_a^2 \right\} = \frac{A_h}{A} \mathbf{P}_h \left(\frac{\partial \mathbf{C}_h}{\partial \tilde{y}_j} + \frac{\mathbf{C}_{h,0}}{u^2} \frac{\partial v_a^2}{\partial \tilde{y}_j} \right). \tag{6.55}$$

The derivative of the aerodynamic coefficient matrix $\mathbf{C}_h$ with respect to a generic variable $\tilde{y}_j$ is

$$\frac{\partial \mathbf{C}_h}{\partial \tilde{y}_j} = \frac{\partial}{\partial \tilde{y}_j} \begin{bmatrix} C_{L,h}\gamma_h - C_{D,h} \\ 0 \\ -C_{L,h} \end{bmatrix} = \begin{bmatrix} C_{L\alpha,h}\gamma_{h,0} - C_{D\alpha,h} \\ 0 \\ -C_{L\alpha,h} \end{bmatrix} \frac{\partial \alpha}{\partial \tilde{y}_j} + \begin{bmatrix} C_{L,h} \\ 0 \\ 0 \end{bmatrix} \frac{\partial \gamma_h}{\partial \tilde{y}_j} = \mathbf{C}_\theta \frac{\partial \gamma_h}{\partial \tilde{y}_j}, \tag{6.56}$$

where $\frac{\partial \alpha}{\partial \tilde{y}_j} = \frac{\partial \gamma_h}{\partial \tilde{y}_j}$.

The derivative of the inflow angle γ_h for the horizontal tail features two contributions, according to the model in Eq. (6.47)

$$\frac{\partial \gamma_h}{\partial \tilde{y}_j} = \frac{\partial \gamma_h^*}{\partial \tilde{y}_j} - \frac{\partial \varepsilon_d}{\partial \tilde{y}_j} = \frac{\partial \gamma_h^*}{\partial \tilde{y}_j} - \varepsilon_{d\alpha} \frac{\partial \gamma_{w,n}}{\partial \tilde{y}_j} = \frac{\partial \gamma_h^*}{\partial \tilde{y}_j} \left(1 - \varepsilon_{d\alpha} \frac{\frac{\partial \gamma_{w,n}}{\partial \tilde{y}_j}}{\frac{\partial \gamma_h^*}{\partial \tilde{y}_j}} \right) \tag{6.57}$$

where $\frac{\partial \gamma_{w,n}}{\partial \tilde{y}_j} / \frac{\partial \gamma_h^*}{\partial \tilde{y}_j}$ is a function of the derivation variable. In particular, $\frac{\partial \gamma_{w,n}}{\partial u} / \frac{\partial \gamma_h^*}{\partial u} = \frac{\partial \gamma_{w,n}}{\partial w} / \frac{\partial \gamma_h^*}{\partial w} = \frac{\partial \gamma_{w,n}}{\partial \theta} / \frac{\partial \gamma_h^*}{\partial \theta} = 1$ and $\varepsilon_{d\alpha} \frac{\partial \gamma_{w,n}}{\partial q} / \frac{\partial \gamma_h^*}{\partial q} \ll 1$ [2]. In Table 6.4, the derivatives with respect to the pertinent states of the windplane are provided. Furthermore, note that derivatives given in Table B.1 can be used also for the horizontal tail.

$\frac{\partial \boldsymbol{f}_h}{\partial \tilde{u}}$	$\frac{A_h}{A} \mathbf{P}_h \left(2\mathbf{C}_h - (1 - \varepsilon_{d\alpha}) \frac{\mathbf{C}_\theta}{\lambda_n} \right)$
$\frac{\partial \boldsymbol{f}_h}{\partial \tilde{w}}$	$\frac{A_h}{A} \mathbf{P}_h \left(2\frac{\mathbf{C}_h}{\lambda_n} + (1 - \varepsilon_{d\alpha}) \mathbf{C}_\theta \right)$
$\frac{\partial \boldsymbol{f}_h}{\partial \tilde{q}}$	$\frac{th_z}{c/2} \frac{A_h}{A} \mathbf{P}_h \left(2\mathbf{C}_h - \frac{\mathbf{C}_\theta}{\lambda_n} \right) - \frac{th_x}{c/2} \frac{A_h}{A} \mathbf{P}_h \left(2\frac{\mathbf{C}_h}{\lambda_n} + \mathbf{C}_\theta \right)$
$\frac{\partial \boldsymbol{f}_h}{\partial \phi}$	$-\frac{th_z}{R_0} \frac{\partial \boldsymbol{f}_h}{\partial \tilde{u}} + \frac{th_x}{R_0} \frac{\partial \boldsymbol{f}_h}{\partial \tilde{w}}$
$\frac{\partial \boldsymbol{f}_h}{\partial \theta}$	$\frac{A_h}{A} \mathbf{P}_h \left(1 - \varepsilon_{d\alpha} \right) \mathbf{C}_\theta$

Table 6.4: *Derivatives of the horizontal tail.*

6.7 Vertical tail

The vertical tail is meant to give lateral stability over the circular path. As the tether attachment position is not located in the center of mass in general, the centrifugal forces generate a moment around the $\boldsymbol{e}_{3,s}$ axis. The vertical tail should then contribute to the moment balance around the yaw axis, as shown in Figure 6.4.

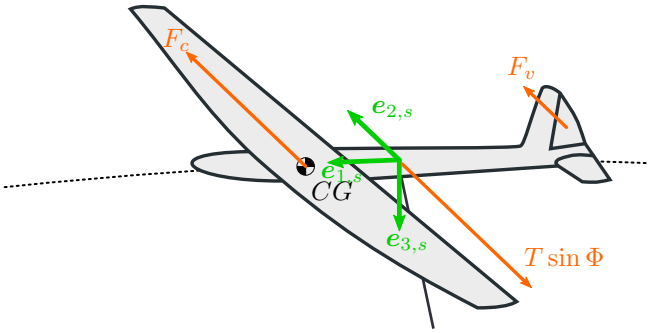

Figure 6.4: *Main forces acting along the y_s axis. The vertical tail aerodynamic force F_v is stabilizing the effect of the centrifugal forces F_c.*

[2] $\frac{\frac{\partial \gamma_{w,n}}{\partial q}}{\frac{\partial \gamma_h^*}{\partial q}} = \frac{\frac{\partial \gamma_{w,n}}{\partial \mathcal{U}} \frac{\partial \mathcal{U}}{\partial q} + \frac{\partial \gamma_{w,n}}{\partial \mathcal{W}} \frac{\partial \mathcal{W}}{\partial q}}{\frac{\partial \gamma_h^*}{\partial \mathcal{U}} \frac{\partial \mathcal{U}}{\partial q} + \frac{\partial \gamma_h^*}{\partial \mathcal{W}} \frac{\partial \mathcal{W}}{\partial q}} = \frac{-\frac{\mathcal{W}_0}{\mathcal{U}_0^2} tw_z - \frac{1}{\mathcal{U}_0} tw_x}{-\frac{\mathcal{W}_0}{\mathcal{U}_0^2} th_z - \frac{1}{\mathcal{U}_0} th_x} \approx \frac{tw_x}{th_x}$

Similar to the horizontal tail, the vertical tail is modelled as a lumped lifting surface, located on the aircraft symmetry plane (i.e. $tv_y = 0$). We assume the vertical tail quarter-chord axis to be parallel to the $\boldsymbol{e}_{3,b}$ axis. The apparent wind velocity perpendicular to the vertical tail lifting line generates aerodynamic forces and can be written as

$$v_a^2 = (c_{\theta_{bs}}\mathcal{U} - s_{\theta_{bs}}\mathcal{W})^2 + \mathcal{V}^2 \approx c_{\theta_{bs}}^2\mathcal{U}^2 + \mathcal{V}^2 - c_{\theta_{bs}}s_{\theta_{bs}}\mathcal{U}\mathcal{W} \approx c_{\theta_{bs}}^2\mathcal{U}^2, \tag{6.58}$$

where $(\mathcal{U}, \mathcal{V}, \mathcal{W})$ the are given in Eq. (6.14).

The inflow angle on the vertical tail γ_v is defined as

$$\gamma_v = \frac{\mathcal{V}}{c_{\theta_{bs}}\mathcal{U} - s_{\theta_{bs}}\mathcal{W}} = \frac{\mathcal{V}}{c_{\theta_{bs}}\mathcal{U}\left(1 - tg_{\theta_{bs}}\frac{\mathcal{W}}{\mathcal{U}}\right)} \approx \frac{\mathcal{V}}{c_{\theta_{bs}}\mathcal{U}}. \tag{6.59}$$

The inflow angle on the vertical tail γ_v at the operating point is defined as

$$\gamma_{v,0} = -\frac{x_v}{R_0 c_{\theta_{bs}}}, \tag{6.60}$$

where x_v is the vertical tail collocation point along $\boldsymbol{e}_{1,s}$.

The angle of attack α_v of the vertical stabilizer is

$$\alpha_v = \gamma_v - \theta_v, \tag{6.61}$$

where θ_v is the pitch of the vertical stabilizer wing, measured as a rotation around $\boldsymbol{e}_{3,b}$.

The lift coefficient $C_{L,v}$ can be found as function of the angle of attack as

$$C_{L,v} = \frac{C_{l\alpha,v}}{1 + \frac{C_{l\alpha,v}}{\pi A R_v}}\alpha_v \tag{6.62}$$

and the drag coefficient $C_{D,v}$ as

$$C_{D,v} = C_{d,v,0} + k_{d,v}C_{L,v}^2 + \frac{C_{L,v}^2}{\pi A R_v}. \tag{6.63}$$

where $C_{d,v,0}$ and $k_{d,v}$ describe the airfoils polars.

The force given by the vertical tail can be written in vector form as

$$\boldsymbol{f}_v = \frac{A_v}{A u_0^2}\mathbf{S}^{-1}\begin{bmatrix}\mathbf{1}\\ \boldsymbol{t}\boldsymbol{v}^{\times}\end{bmatrix}\begin{bmatrix}C_{L,v}\gamma_v - C_{D,v}\\ -C_{L,v}\\ 0\end{bmatrix}v_a^2, \tag{6.64}$$

where A_v is the vertical tail area and $C_{L,v}$ and $C_{D,v}$ the aerodynamic coefficients of the vertical tail.

At the operating point $\boldsymbol{y}_0$, the aerodynamic force non-dimensional force given by the vertical tail is

$$\boldsymbol{f}_{v,0} = \frac{A_v}{A}\mathbf{P}_v\mathbf{C}_{v,0}c_{\theta_{bs}}^2, \tag{6.65}$$

where $\mathbf{P}_v = \mathbf{S}^{-1}[\mathbf{1}; \boldsymbol{t}\boldsymbol{v}^{\times}]$, $\mathbf{C}_{v,0} = [C_{L,v}\gamma_v - C_{D,v}, -C_{L,v}, 0]^T$.

Correspondingly, the derivative of the force vector with respect to a generic variable $\tilde{y}_j$ can be written as

$$\frac{\partial \boldsymbol{f}_v}{\partial \tilde{y}_j} \approx \frac{A_v}{A}\mathbf{P}_v \left(\frac{\partial \mathbf{C}_v}{\partial \tilde{y}_j} + \frac{\mathbf{C}_{v,0}}{u_0^2}\frac{\partial \mathcal{U}^2}{\partial \tilde{y}_j} \right) c_{\theta_{bs}}^2, \tag{6.66}$$

and the derivative of the aerodynamic coefficient matrix $\frac{\partial \mathbf{C}_v}{\partial \tilde{y}_j}$ can be written as follows

$$\frac{\partial \mathbf{C}_v}{\partial \tilde{y}_j} = \begin{bmatrix} C_{L,v} \\ 0 \\ 0 \end{bmatrix} \frac{\partial \gamma_v}{\partial \tilde{y}_j} + \begin{bmatrix} C_{L\alpha,v}\gamma_{v,0} - C_{D\alpha,v} \\ -C_{L\alpha,v} \\ 0 \end{bmatrix} \frac{\partial \alpha_v}{\partial \tilde{y}_j} = \mathbf{C}_\psi \frac{\partial \gamma_v}{\partial \tilde{y}_j}. \tag{6.67}$$

The derivative with respect to the control input θ_v is

$$\frac{\partial \boldsymbol{f}_v}{\partial \theta_v} = \frac{A_v}{A}\mathbf{P}_v \frac{\partial \mathbf{C}_v}{\partial \alpha_v}\frac{\partial \alpha_v}{\partial \theta_v} c_{\theta_{bs}}^2 = -\frac{A_v}{A}\mathbf{P}_v \begin{bmatrix} C_{L\alpha,v}\gamma_{v,0} - C_{D\alpha,v} \\ -C_{L\alpha,v} \\ 0 \end{bmatrix} c_{\theta_{bs}}^2, \tag{6.68}$$

where $\frac{\partial \alpha_v}{\partial \theta_v} = -1$.

In Table 6.5 the derivatives of γ_v and v_a^2 with respect to $\mathcal{U}$, $\mathcal{V}$, $\mathcal{W}$ are reported, while in Table 6.6 the contributions to the force and moment derivatives with respect to the windplane state variables are provided for the vertical tail.

	γ_v	$\mathcal{U}^2$
$\mathcal{U}$	$-\frac{\gamma_{v,0}}{u_0}$	$2u_0$
$\mathcal{V}$	$\frac{1}{c_{\theta_{bs}} u_0}$	≈ 0
$\mathcal{W}$	0	0

Table 6.5: *Derivatives of $\gamma_{w,n}$ and v_a^2 with respect to $\mathcal{U}$, $\mathcal{V}$ and $\mathcal{W}$ for the vertical tail.*

$\frac{\partial \boldsymbol{f}_v}{\partial \tilde{u}}$	$\frac{A_v}{A}\mathbf{P}_v \left(-\gamma_{v,0}\mathbf{C}_\psi + 2\mathbf{C}_v\right) c_{\theta_{bs}}^2$
$\frac{\partial \boldsymbol{f}_v}{\partial \tilde{v}}$	$\frac{A_v}{A}\mathbf{P}_v \mathbf{C}_\psi c_{\theta_{bs}}$
$\frac{\partial \boldsymbol{f}_v}{\partial \tilde{p}}$	$-\frac{tv_z}{b/2}\frac{\partial \boldsymbol{f}_v}{\partial \tilde{v}}$
$\frac{\partial \boldsymbol{f}_v}{\partial \tilde{q}}$	$\frac{tv_z}{c/2}\frac{\partial \boldsymbol{f}_v}{\partial \tilde{u}}$
$\frac{\partial \boldsymbol{f}_v}{\partial \tilde{r}}$	$\frac{tv_x}{b/2}\frac{\partial \boldsymbol{f}_v}{\partial \tilde{v}}$
$\frac{\partial \boldsymbol{f}_v}{\partial \phi}$	$-\frac{c/2}{R_0}\frac{\partial \boldsymbol{f}_v}{\partial \tilde{q}}$

Table 6.6: *Derivatives of the vertical tail.*

6.8 Tether

In this thesis, we treat the tether as a constraint on the radial position with respect to the ground station. Since only the component of the apparent velocity perpendicular to the tether direction generates drag, the apparent velocity is expressed in $\mathcal{F}_{Te}$, defined in Sect. 5.3. As in Sect. 3.2, the tether drag is lumped with the windplane at the tether attachment and the wind velocity is neglected. We use the same modeling approach here

$$\boldsymbol{v}_a^{Te} = \mathbf{R}_{TeS}\boldsymbol{v}_a \approx -\mathbf{R}_{TeR}\mathbf{R}_{RS}\boldsymbol{v} = -\begin{bmatrix} 1 & 0 & 0 \\ 0 & \cos\Phi & \sin\Phi \\ 0 & -\sin\Phi & \cos\Phi \end{bmatrix}\begin{bmatrix} 1 & -\psi & \theta \\ \psi & 1 & -\phi \\ -\theta & \phi & 1 \end{bmatrix}\begin{bmatrix} u \\ v \\ w \end{bmatrix} \tag{6.69}$$

where $\mathbf{R}_{TeR} = \mathbf{R}_x(-\Phi)$ and $\mathbf{R}_{RS} = 1 + \boldsymbol{e}\boldsymbol{u}^{\times}$.

For the crossflow principle, only the components of the apparent velocity perpendicular to the tether are contributing to aerodynamic forces. The apparent velocity contributing to aerodynamic force is

$$\boldsymbol{v}_{a,te}^{Te} \approx \begin{bmatrix} -u \\ \cos\Phi\left(-\psi u - v\right) + \sin\Phi\left(\theta u - w\right) \\ 0 \end{bmatrix} \tag{6.70}$$

where the products of two small quantities are neglected.

The modulus of the apparent velocity is then

$$v_{a,te}^2 = u^2 + \left(\cos\Phi\left(-\psi u - v\right) + \sin\Phi\left(\theta u - w\right)\right)^2 \approx u^2 \tag{6.71}$$

which at the operating point is $v_{a,te,0}^2 = u_0^2$.

The inflow angle γ_{te} is the ratio between the second and the first element of Eq. (6.70)

$$\gamma_{te} = \frac{\cos\Phi\left(\psi u + v\right) + \sin\Phi\left(w - \theta u\right)}{u} \tag{6.72}$$

The equivalent tether drag force in $\mathcal{F}_S$ is

$$\boldsymbol{f}_{te} = -C_{D,te}\mathbf{R}_{STe}\begin{bmatrix} 1 \\ \gamma_{te} \\ 0 \end{bmatrix}\frac{v_{a,te}^2}{u_0^2} = -C_{D,te}(1 - \boldsymbol{e}\boldsymbol{u}^{\times})\mathbf{R}_{RTe}\begin{bmatrix} 1 \\ \gamma_{te} \\ 0 \end{bmatrix}\frac{v_{a,te}^2}{u_0^2}, \tag{6.73}$$

where $C_{D,te}$ is defined in Eq. (3.6)

At the operating point $\boldsymbol{y}_0$, the aerodynamic force due to the tether acting on the windplane is

$$\boldsymbol{f}_{te,0} = -C_{D,te}\boldsymbol{e}_1, \tag{6.74}$$

The derivative of the equivalent tether drag with respect to a generic variable $\tilde{y}_j$ is

$$\frac{\partial \boldsymbol{f}_{te}}{\partial \tilde{y}_j} = -C_{D,te}\left(\frac{1}{u_0^2}\frac{\partial v_{a,te}^2}{\partial \tilde{y}_j} - \frac{\partial \boldsymbol{e}\boldsymbol{u}^{\times}}{\partial \tilde{y}_j}\right)\boldsymbol{e}_1 - C_{D,te}\begin{bmatrix} 0 \\ \cos\Phi_0 \\ \sin\Phi_0 \end{bmatrix}\frac{\partial \gamma_{te}}{\partial \tilde{y}_j} \tag{6.75}$$

where Φ_0 is the opening angle at the operating point.

The only derivative of the apparent velocity squared different from zero is the derivative with respect to $\tilde{u}$ ($\frac{1}{u_0^2}\frac{\partial v_{a,te}^2}{\partial \tilde{u}} = 2$). In Table 6.7, the derivatives of the inflow angle γ_{te} with respect to the state variables is given. The derivative of the force with respect to $\tilde{u}$ is

$$\frac{\partial \boldsymbol{f}_{te}}{\partial \tilde{u}} = -2C_{D,te}\boldsymbol{e}_1. \tag{6.76}$$

	γ_{te}	$\frac{\partial \boldsymbol{e}\boldsymbol{u}^\times}{\partial \tilde{y}_j}\boldsymbol{e}_1$
$\tilde{u}$	0	0
$\tilde{v}$	$\cos\Phi_0$	0
$\tilde{w}$	$\sin\Phi_0$	0
θ	$-\sin\Phi_0$	$\boldsymbol{e}_3$
ψ	$\cos\Phi_0$	$-\boldsymbol{e}_2$

Table 6.7: *Derivatives of $\gamma_{w,n}$ and v_a^2 with respect to $\mathcal{U}$, $\mathcal{V}$ and $\mathcal{W}$ for the vertical tail.*

The other derivatives can be evaluated with the results in Table 6.7. The derivative of the force with respect to $\tilde{v}$ is

$$\frac{\partial \boldsymbol{f}_{te}}{\partial \tilde{v}} = -C_{D,te}\cos\Phi_0 \begin{bmatrix} 0 \\ \cos\Phi_0 \\ \sin\Phi_0 \end{bmatrix}. \tag{6.77}$$

The derivative of the force with respect to $\tilde{w}$ is

$$\frac{\partial \boldsymbol{f}_{te}}{\partial \tilde{w}} = -C_{D,te}\sin\Phi_0 \begin{bmatrix} 0 \\ \cos\Phi_0 \\ \sin\Phi_0 \end{bmatrix}. \tag{6.78}$$

The derivative of the force with respect to the pitch angle θ is

$$\frac{\partial \boldsymbol{f}_{te}}{\partial \theta} = C_{D,te}\left(\boldsymbol{e}_3 + \sin\Phi_0 \begin{bmatrix} 0 \\ \cos\Phi_0 \\ \sin\Phi_0 \end{bmatrix}\right). \tag{6.79}$$

Finally, the derivative of the force with respect to the yaw angle ψ is

$$\frac{\partial \boldsymbol{f}_{te}}{\partial \psi} = -C_{D,te}\left(\boldsymbol{e}_2 + \cos\Phi_0 \begin{bmatrix} 0 \\ \cos\Phi_0 \\ \sin\Phi_0 \end{bmatrix}\right). \tag{6.80}$$

Note that this last derivative is the only dependence of the aerodynamic forces $\boldsymbol{f}_a$ with respect to the yaw angle ψ. The aerodynamic of the windplanes, similarly to airplanes, does not depend of the yaw, but the aerodynamics of the tether does.

6.9 Onboard wind turbines

The onboard turbines generate aerodynamic forces, necessary for the power generation. Depending on where they are located and how they are operated, they generate moments. For a easier understanding of the results, we assume they are concentrated at the tether attachment and thus do not generate any moment.

The rotor axes are assumed to be aligned with the $\boldsymbol{e}_{1,b}$ direction. The apparent velocity in the body coordinate system $\mathcal{F}_B$ along $\boldsymbol{e}_{1,b}$ is

$$v_{a,t} = \boldsymbol{v}_a \cdot \boldsymbol{e}_{1,b} = -\mathbf{R}_{BS} \begin{bmatrix} \mathcal{U} \\ \mathcal{V} \\ \mathcal{W} \end{bmatrix} \cdot \begin{bmatrix} 1 \\ 0 \\ 0 \end{bmatrix} = -(\mathcal{U}\cos\theta_{bs} + \mathcal{W}\sin\theta_{bs}) \approx -u_0\cos\theta_{bs} \tag{6.81}$$

The aerodynamic force generated by the onboard turbines is

$$\boldsymbol{f}_t = -\frac{A_t}{Au_0^2}\mathbf{R}_{SB}^S \begin{bmatrix} C_{T,t} \\ 0 \\ 0 \end{bmatrix} v_{a,t}^2. \tag{6.82}$$

At the operating point $\boldsymbol{y}_0$, the turbine force is

$$\boldsymbol{f}_{t,0} = -\frac{A_t}{A}C_{T,t}\cos\theta_{bs}^2 \begin{bmatrix} \cos\theta_{bs} \\ 0 \\ \sin\theta_{bs} \end{bmatrix}. \tag{6.83}$$

Neglecting the dependence of the thrust coefficient with respect to any state variable, the only derivative different from zero is

$$\frac{\partial \boldsymbol{f}_t}{\partial \tilde{u}} = -2\frac{A_t}{A}C_{T,t}\cos\theta_{bs}^2 \begin{bmatrix} \cos\theta_{bs} \\ 0 \\ \sin\theta_{bs} \end{bmatrix}. \tag{6.84}$$

The dimensional instantaneous power generated by the onboard turbines is

$$P = \frac{1}{2}\rho A_t C_{P,t} v_{a,t}^3 \approx \frac{1}{2}\rho A_t C_{P,t} u_0^3 \cos\theta_{bs}^3. \tag{6.85}$$

6.10 Discussion

In this section, the aerodynamic forces acting on the windplane are linearized about a nonlinear operating point. The non-dimensional aerodynamic force can then be written as

$$\boldsymbol{f}_a = \boldsymbol{f}_{w,0} + \boldsymbol{f}_{al,0} + \boldsymbol{f}_{h,0} + \boldsymbol{f}_{v,0} + \boldsymbol{f}_{te,0} + \left(\frac{\partial \boldsymbol{f}_w}{\partial \tilde{\boldsymbol{y}}} + \frac{\partial \boldsymbol{f}_{al}}{\partial \tilde{\boldsymbol{y}}} + \frac{\partial \boldsymbol{f}_h}{\partial \tilde{\boldsymbol{y}}} + \frac{\partial \boldsymbol{f}_v}{\partial \tilde{\boldsymbol{y}}} + \frac{\partial \boldsymbol{f}_{te}}{\partial \tilde{\boldsymbol{y}}}\right)\Delta\tilde{\boldsymbol{y}}, \tag{6.86}$$

where the operating point state vector $\boldsymbol{y}_0$ is defined in Eq. (6.8) and the incremental state vector $\Delta\tilde{\boldsymbol{y}}$ in Eq. (6.9). Note that the contribution from the onboard wind turbines is not considered among the aerodynamic force.

In the derivation of this aerodynamic model, an elliptic planform for the main wing, for the horizontal and vertical stabilizers is assumed. The main wing dihedral and sweep angles are considered small. The wake curvature is neglected and the induction due to the far wake is decreasing the incoming wind speed. The aerodynamic derivatives are taken analytically by an extensive use of strip theory.

This aerodynamic model has been validated with a vortex lattice formulation (Trevisi et al. (2021a)).

CHAPTER 7

Windplane optimal trajectories: T-GliDe

In Part I, the windplane is modeled as a point mass and a conceptual design is performed based on this idealization. We now want to study the design with an higher level of physical representation. The nonlinear rigid body equations of motion derived in Chap. 5 and the aerodynamic model derived in Chap. 6 are then used to formulate optimal problems.

In this chapter, the design framework T-GliDe (Tethered Gliding systems Design) is introduced and it is used to study optimal trajectories. This chapter is organized as follows:

The harmonic balance method, which is used to solve the equations of motion, is introduced in Sec 7.1. The fundamental frequency and the power balance equation are derived in Sect. 7.2 and 7.3. A yaw stability augmentation system, needed to enhance flight stability, is proposed in Sect. 7.4. The optimization problem is formulated in Sect. 7.5. The optimal trajectories of the light windplane, designed in Chap. 4, are analyzed in Sect. 7.6. The main results are discussed in Sect. 7.7.

7.1 Harmonic balance method

Since the problem of optimal trajectories for windplanes has a periodic nature, its flight dynamic model is expressed in the frequency domain. The harmonic balance methodology is used to transform the differential equations of motion into a set of nonlinear algebraic equations (Dimitriadis (2017)). In this section, the formulation of the harmonic balance method used in this thesis is presented.

The equations of motion (Eq. 5.5) can be written as a set of nonlinear differential equations with respect to the state variables $\boldsymbol{y}$ and the control variables $\boldsymbol{u}$

$$\boldsymbol{h}(\boldsymbol{y}, \dot{\boldsymbol{y}}, \boldsymbol{u}) = \boldsymbol{0}. \tag{7.1}$$

The state vector $\boldsymbol{y}$ describing the windplane dynamic is

$$\boldsymbol{y} = \left[u,\ v,\ w,\ p,\ q,\ r,\ \phi,\ \theta_{rb},\ \psi,\ \dot{\Psi},\ \Phi\right]^T, \tag{7.2}$$

and the control vector $\boldsymbol{u}$ is

$$\boldsymbol{u} = \left[C_{L,al},\ \theta_h,\ \theta_v,\ a_t\right]^T, \tag{7.3}$$

By assuming that the equations of motion (Eq. 7.1) accepts periodic solutions, every variable of the state vector $\boldsymbol{y}$ is expanded as a Fourier series of order N_y

$$y_j(t) \approx \frac{Y_{j,0}}{2} + \sum_{k=1}^{N_y} Y_{j,k,s} \sin\left(k\omega t\right) + Y_{j,k,c} \cos\left(k\omega t\right), \tag{7.4}$$

with $\omega = \dfrac{2\pi}{\mathcal{T}}$ being the fundamental frequency of the motion and $\mathcal{T}$ the period. Note that we listed among the state vector $\boldsymbol{y}$ the time derivative of the azimuth position $\dot{\Psi}$, which is periodic, and not the azimuth position itself Ψ, which is not periodic. The Fourier coefficients can be grouped as

$$\mathbf{Y}_j = \left[Y_{j,0},\ Y_{j,1,s},\ Y_{j,2,s},\ ...Y_{j,1,c},\ Y_{j,2,c},\ ...\right]^T, \tag{7.5}$$

The first and second time derivatives of the state vector can be found analytically

$$\dot{y}_j(t) \approx \sum_{k=1}^{N_x} k\omega \left(Y_{j,k,s} \cos\left(k\omega t\right) - Y_{j,k,c} \sin\left(k\omega t\right)\right), \tag{7.6}$$

and

$$\ddot{y}_j(t) \approx -\sum_{k=1}^{N_x} (k\omega)^2 \left(Y_{j,k,s} \sin\left(k\omega t\right) + Y_{j,k,c} \cos\left(k\omega t\right)\right). \tag{7.7}$$

Similarly, the control inputs, assumed to be periodic, can be modeled as a Fourier series of order N_u

$$u_j(t) = \frac{U_{j,0}}{2} + \sum_{k=1}^{N_u} U_{j,k,s} \sin\left(k\omega t\right) + U_{j,k,c} \cos\left(k\omega t\right), \tag{7.8}$$

where $N_u < N_y$ because the equations of motion need to be solved at frequencies higher than the control inputs order. The Fourier coefficients can be grouped as

$$\mathbf{U}_j = \left[U_{j,0},\ U_{j,1,s},\ U_{j,2,s},\ ...U_{j,1,c},\ U_{j,2,c},\ ...\right]^T, \tag{7.9}$$

Each equation of the equations of motion (Eq. 7.1) can also be expanded as a Fourier series of order N_y

$$h_j(\mathbf{Y}, \mathbf{U}, \omega, t) \approx \frac{H_{j,0}}{2} + \sum_{k=1}^{N_y} H_{j,k,s} \sin\left(k\omega t\right) + H_{j,k,c} \cos\left(k\omega t\right) = \mathbf{0}, \tag{7.10}$$

where the Fourier coefficients of the nonlinear equations of motion are grouped as

$$\mathbf{H}_j = \left[H_{j,0},\ H_{j,1,s},\ H_{j,2,s},\ ...H_{j,1,c},\ H_{j,2,c},\ ...\right]^T. \tag{7.11}$$

The Fourier coefficients of the equations of motion are found numerically by applying the Fourier coefficient definition to the time series, which should have a minimum size of $2N_y + 1$. The result is $(2N_y + 1)$ nonlinear algebraic equations per each state as a consequence of the orthogonality properties of the selected basis of trigonometric functions

$$\boldsymbol{h}_{ocp} = \mathbf{H}(\mathbf{Y}, \mathbf{U}, \omega) = \left[\mathbf{H}_0,\ \mathbf{H}_{1,s},\ \mathbf{H}_{2,s},\ ...\mathbf{H}_{1,c},\ \mathbf{H}_{2,c},\ ...\right]^T = \mathbf{0}, \tag{7.12}$$

which can be understood as the residuals of the equations of motion expressed in the frequency domain. For given periodic control inputs $\mathbf{U}$, the periodic solution can be found by looking for the Fourier coefficients $\mathbf{Y}$ of the dynamics which solve Eq. 7.12.

7.2 Fundamental frequency estimation

The azimuth $\Psi(t)$ can be found by integrating $\dot{\Psi}(t)$ between the initial time and t

$$\Psi(t) = \int_0^t \dot{\Psi} dt. \tag{7.13}$$

For the solution to be periodic, Ψ after one period needs to be -2π

$$\Psi(T) = \int_{\mathcal{T}_0}^{\mathcal{T}_0+\mathcal{T}} \dot{\Psi} dt = \int_0^{\mathcal{T}} \dot{\Psi} dt = -2\pi. \tag{7.14}$$

The mean value of $\dot{\Psi}(t)$ over a period is

$$\hat{\dot{\Psi}}(T) = \frac{1}{\mathcal{T}} \int_{\mathcal{T}_0}^{\mathcal{T}_0+\mathcal{T}} \dot{\Psi} dt = \frac{1}{\mathcal{T}} \int_0^{\mathcal{T}} \dot{\Psi} dt = -\frac{2\pi}{\mathcal{T}}. \tag{7.15}$$

Defining the fundamental frequency $\omega = \frac{2\pi}{\mathcal{T}}$, we find that

$$\omega = -\hat{\dot{\Psi}}. \tag{7.16}$$

7.3 Power balance

We can get to a power balance equation by multiplying the dimensional equations of motion (Eq. 5.5) with the plane velocity

$$\left(\mathbf{m}\dot{\mathrm{v}} + \mathrm{v}^{\times}\mathbf{m}\mathrm{v}\right) \cdot \mathrm{v} = \boldsymbol{F}_a \cdot \mathrm{v} + \boldsymbol{F}_t \cdot \mathrm{v} + \boldsymbol{F}_g \cdot \mathrm{v}, \tag{7.17}$$

Note that the tether force does not contribute to the power balance because no displacement is allowed in the tether direction (i.e. the tether is a constraint).

We write the power balance equation in non-dimensional form considering the reference power $\mathbb{P} = \frac{1}{2}\rho\pi b^2 v_w^3$, so that the nondimensional aerodynamic power is

$$\frac{1}{\mathbb{P}}\boldsymbol{F}_a \cdot \mathrm{v} = \frac{\mathbb{F}}{\mathbb{P}}\mathbf{S}\boldsymbol{f}_a \cdot \mathrm{v} = \frac{\lambda^2}{\pi \mathcal{R}}\mathbf{S}\boldsymbol{f}_a \cdot \frac{\mathrm{v}}{v_w}. \tag{7.18}$$

where in the unit force $\mathbb{F}$, used to compute the aerodynamic force, we take the plane velocity u

$$\frac{\mathbb{F}}{\mathbb{P}} = \frac{\frac{1}{2}\rho A u^2}{\frac{1}{2}\rho\pi b^2 v_w^3} = \frac{\lambda^2}{\pi \mathcal{R}}\frac{1}{v_w}. \tag{7.19}$$

We can now rewrite Eq. (7.17) in nondimensional form as

$$\underbrace{\frac{1}{\mathbb{P}}\left(\mathbf{m}\dot{\mathrm{v}}+\mathrm{v}^{\times}\mathbf{m}\mathrm{v}\right)\cdot\mathrm{v}}_{\frac{\partial e_k}{\partial t}}=\underbrace{\frac{\lambda^2}{\pi\mathcal{AR}}\mathbf{S}\boldsymbol{f}_a\cdot\frac{\mathrm{v}}{v_w}}_{C_a}+\underbrace{\frac{\lambda^2}{\pi\mathcal{AR}}\mathbf{S}\boldsymbol{f}_t\cdot\frac{\mathrm{v}}{v_w}}_{C_P\frac{C_{T,t}}{C_{P,t}}}+\underbrace{\frac{\boldsymbol{F}_g\cdot\mathrm{v}}{\mathbb{P}}}_{C_g},\tag{7.20}$$

where the left-hand-side is the change in kinetic energy and on the right-hand-side the first term is the aerodynamic power, the second is the thrust power of the onboard turbines, the third is the gravitational power.

The aerodynamic power C_a can be written as in Sec. 4.4

$$C_a = C_T(1-a) - C_\tau,\tag{7.21}$$

where C_T is the thrust coefficient, defined as in Eq. (2.20), and C_τ is power dissipated in parasite drag. The thrust power of the onboard turbines can be derived from Eq. (6.82) and the gravitational power from Eq. (5.11).

7.4 Yaw stability augmentation system

The aerodynamic model depends on the yaw angle exclusively because of the tether drag through Eq. (6.80). Thus, the open-loop aerodynamic yaw damping relies only on the tether drag. A closed-loop control is needed to increase directional stability. The benefits of the simple yaw stability augmentation system presented in this section are discussed in the next chapter.

The control force due to the pitching of the vertical stabilizer θ_v is

$$\boldsymbol{f}_{\theta_v} = \frac{\partial \boldsymbol{f}_v}{\partial \theta_v}\theta_v\tag{7.22}$$

where $\frac{\partial \boldsymbol{f}_v}{\partial \theta_v}$ is found in Eq. (6.68).

The pitch angle of the vertical stabilizer can be controlled proportionally to the time derivative of the yaw angle $\theta_v = \kappa_d\dot{\psi}$, such that

$$\boldsymbol{f}_{\theta_v} = \kappa_d\frac{\partial \boldsymbol{f}_v}{\partial \theta_v}\dot{\psi}.\tag{7.23}$$

In this chapter, the derivative gain is considered to be $\kappa_d = 0.075$ s.

7.5 T-GliDe

In this section, the multidisciplinary design, analysis and optimization framework T-GliDe (Tethered Gliding systems Design) is introduced and the optimal design problem formulated. T-GliDe has a monolithic structure, characterized by an "all-at-once" formulation. This enable the use of algorithmic differentiation for the gradient evaluation. The problem is solved with gradient descendant optimization algorithms, which are typically the best methods for continuous physics-based design problems.

In Fig. 7.1, the XDSM diagram (Lambe and Martins (2012)) of T-GliDe is presented. The XDSM diagram describes the optimal design problem, which can be easily converted to an optimal control problem by moving (AR, μ, d_{te}) from design variables

to independent variables. A reminder of the physical meaning of the design variables is given in Table 7.1, the constraints in Table 7.2 and the independent variables in Table 7.3.

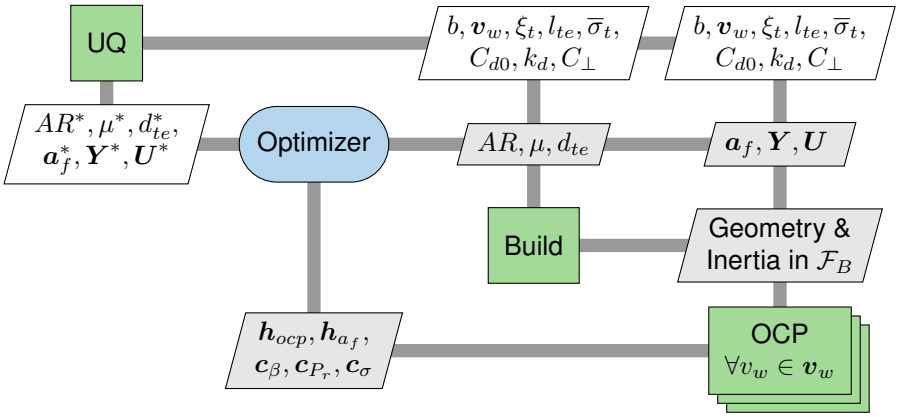

Figure 7.1: *XDSM diagram of T-GliDe.*

The geometrical design variables AR, μ, d_{te} are first used to build the plane geometry and compute the inertia tensor in $\mathcal{F}_B$. The inertia tensor is estimated with the procedure in Appendix C. The optimal control problems are then solved at each wind speed. The optimizer makes use of the optimal control problems' outputs to improve the design, while setting the residual of the equations of motion to zero and respecting the other constraints. This problem formulation is called "all-at-once" (AAO), as it makes the main optimizer to solve at the same time the optimization problem and the individual disciplines (Martins and Lambe (2013)). As this problem formulation is suitable to be used with algorithmic differentiation, *Casadi* (Andersson et al. (2019)) is used to compute analytically the derivatives of the objective function and of the constraints with respect to the design variables. The derivative expressions are then provided to the optimizer. This technique enable a drastic reduction in computational time with respect to a problem formulation employing a finite-difference method for the gradient evaluation. In this thesis, T-GliDe is not used to solve optimal design problems, but to solve optimal control problems. The optimal design problem will be approached with T-GliDe in the future.

To study how uncertainties propagate throughout the design process, the uncertainty quantification toolbox *UQLab* (Marelli and Sudret (2014)) is linked to the optimization problem. In this thesis, no uncertainty quantification study is carried out. These investigations will be performed in the future.

7.6 Optimal trajectories

In this section, we analyze two optimal trajectories of the light windplane in Table 4.3.

The first OCP is an open-loop aerodynamic steady problem, with the gravity set to zero $g = 0$. We refer to this OCP as T-GliDe$_a$, where a stands for aerodynamic. The control inputs ($C_{L,al},\ \theta_h,\ \theta_v,\ a_t$) are trimmed to constant values by the optimizer.

The second OCP is a closed-loop dynamic problem, where the gravity is included. We refer to this OCP as T-GliDe$_g$, where g stands for gravity. In Chap. 4, we found

Table 7.1: *Dimension and description of the design variables for the optimal design problems.*

	dimensions	Description
AR	1	Wing aspect ratio
μ	1	Non-dimensional mass ($\mu = \frac{m}{\rho b^3}$)
d_{te}	1	Non-dimensional tether diameter ($d_{te} = \frac{D_{te}}{b/2}$)
$\boldsymbol{a}_f$	N_{v_w}	Far wake induction
$\boldsymbol{Y}$	$N_{v_w} \cdot 11 \cdot (2N_y + 1)$	Fourier coefficients of the state variables $\boldsymbol{y}$
$\boldsymbol{U}$	$N_{v_w} \cdot 4 \cdot (2N_u + 1)$	Fourier coefficients of the control variables $\boldsymbol{u}$

Table 7.2: *Description of the constraints for the optimal design problems.* $\boldsymbol{h}$ *are equality constraints and* $\boldsymbol{c}$ *are inequality constraints.*

	dimensions	Description
$\boldsymbol{h}_{ocp}$	$N_{v_w} \cdot 11 \cdot (2N_y + 1)$	Residuals of the equations of motion (Eq. (7.12))
$\boldsymbol{h}_{a_f}$	N_{v_w}	Residual of the far wake equation
$\boldsymbol{c}_\beta$	N_{v_w}	Positive mean elevation angle $\hat{\beta} > 0$
$\boldsymbol{c}_{P_r}$	$N_{v_w} \cdot N_t$	Rated power of onboard generators
$\boldsymbol{c}_\sigma$	N_{v_w}	Maximum mean tether stress

that the windplane stays airborne by compensating the radial component of gravity by means of the roll angle (Figures 4.1 and 4.3b). The roll is mainly controlled by the differential lift coefficient provided by the ailerons $C_{L,al}$. Therefore, the control input $C_{L,al}$ is modeled up to the first harmonic as

$$C_{L,al} = \hat{C}_{L,al} + Y_{C_{L,al},1,s} \sin(\omega t) + Y_{C_{L,al},1,c} \cos(\omega t). \tag{7.24}$$

The other control inputs ($\theta_h,\ \theta_v,\ a_t$) are still trimmed to constant values by the optimizer.

The equations of motion are solved up to the tenth harmonic $N_y = 10$. The algorithm SQP available in MATLAB is used to solve the optimization problems.

The OCPs are solved on an Intel Core i7-9700 3.0 GHz, 16GB RAM, system. The computation times of the presented optimal control problems require a few minutes. The optimization problem T-GliDe$_a$ converges in 61 iterations and 262 seconds, starting from a general and not feasible circular trajectory. The OCP T-GliDe$_g$ converges in 20 iterations and 65 seconds, starting from the solution of T-GliDe$_a$.

We consider the same independent variables as for the point mass case (Table 4.2), which are reported in Table 7.3 with some additional independent variables defining the problem in T-GliDe. A wind speed of $v_w = 5$ m/s is considered in this chapter, to study the windplane at a low wind speed. The inequality constraint related to the tether stress c_σ and the rated power c_{P_r} are not considered for the optimal control problem. The optimal design problem is modified to an optimal control problem by treating the variables (AR, μ, d_{te}) as independent variables.

In Table 7.4, the main results from the point mass model are reported, together with the corresponding results from the aerodynamic OCP T-GliDe$_a$ and the dynamic OCP T-GliDe$_g$. To compare results between the point mass and the rigid body formulations, two point mass OCPs are solved. The first is a steady aerodynamic OCP, where gravity is set to zero (PM$_a$). In the second OCP PM$_g$, the gravity is included. The onboard

Table 7.3: *Values and description of the independent variables for the optimal control problem.*

		units	Description
b	10	m	Wing span
AR	6	-	Aspect ratio of main wing and stabilizers
v_w	5	m/s	Wind velocity
ξ_t	0.15	-	Non dimensional onboard wind turbines radius
$C_{d,0}$	0.004	-	Airfoil polar parameters (Eq. 3.2) of main wing and stabilizers
k_d	0.008	-	
$C_{d,te}$	0.8	-	Tether section drag coefficient
l_{te}	20	-	Tether length ratio ($L_{te}/(b/2)$)
d_{te}	1.6	mm/m	Tether diameter ratio ($D_{te}/(b/2)$)
μ	0.1	-	Nondimensional mass ($m/(\rho b^3)$), leading to a mass $m = 122.5$ kg
Γ	-20	$^\circ$	Main wing dihedral in $\mathcal{F}_B$
Λ	0	$^\circ$	Main wing sweep in $\mathcal{F}_B$
b_h/b	0.3	-	Ratio between horizontal stabilizer span and wingspan
b_v/b	0.2	-	Ratio between vertical stabilizer span and wingspan
tw	$[0.1, 0, 0]$	-	Non-dimensional main wing quarter-chord position (normalized with $b/2$)
ts	$[-1, 0, 0]$	-	Non-dimensional vertical and horizontal stabilizer position (normalized with $b/2$)
I_{xx}	277	kg m^2	Inertia with respect to $\boldsymbol{e}_{1,b}$ axis
I_{yy}	133	kg m^2	Inertia with respect to $\boldsymbol{e}_{2,b}$ axis
I_{zz}	410	kg m^2	Inertia with respect to $\boldsymbol{e}_{3,b}$ axis
κ_d	0.075	s	Derivative gain for the yaw SAS ($\theta_v = \kappa_d \dot{\psi}$)

turbines axial induction is set constant, and two harmonics are used to model the lift coefficient as a function of the azimuth position.

Table 7.4: *Optimal trajectory results obtained with the point-mass model (OD PM$_L$ of Table 4.3) and with T-GliDe at $v_w = 5$ m/s. The pedix a and g stand for aerodynamic and gravity.*

PM$_a$	$\hat{C}_P = 1.13$	$\hat{C}_T = 3.2$	$\hat{C}_L = 0.70$	$\kappa_0 = 0.13$	$a_f = 0.057$
$g = 0$ m/s^2	$a_t = 0.03$	$C_{T,t} = 0.13$	$\hat{\lambda} = 9.29$	$\hat{P} = 27.3$ kW	$\mathcal{T} = 5.4$ s
PM$_g$	$\hat{C}_P = 1.11$	$\hat{C}_T = 3.2$	$\hat{C}_L = 0.72$	$\kappa_0 = 0.13$	$a_f = 0.058$
	$a_t = 0.03$	$C_{T,t} = 0.12$	$\hat{\lambda} = 9.24$	$\hat{P} = 26.7$ kW	$\mathcal{T} = 5.35$ s
T-GliDe$_a$	$\hat{C}_P = 1.052$	$\hat{C}_T = 3.01$	$\hat{C}_L = 0.72$	$\kappa_0 = 0.135$	$a_f = 0.058$
$g = 0$ m/s^2	$a_t = 0.040$	$C_{T,t} = 0.15$	$\hat{\lambda} = 8.58$	$\hat{P} = 25.3$ kW	$\mathcal{T} = 5.4$ s
T-GliDe$_g$	$\hat{C}_P = 1.035$	$\hat{C}_T = 3.32$	$\hat{C}_L = 0.83$	$\kappa_0 = 0.16$	$a_f = 0.094$
	$a_t = 0.043$	$C_{T,t} = 0.16$	$\hat{\lambda} = 8.11$	$\hat{P} = 24.9$ kW	$\mathcal{T} = 4.7$ s

The mean quantities predicted by T-GliDe and by the point mass model PM are similar. The differences, analyzed in this section, are attributed to the presence of the stabilizers and to the different hypotheses of the models.

The wing speed ratio as a function of the non-dimensional time is shown in Fig. 7.2a and the power coefficient C_P in Fig. 7.2b. The trends predicted by the two models are similar, with the plane increasing the velocity and generating more electric power when moving downwards.

In Fig. 7.3a, the differential lift coefficient provided by the ailerons $C_{L,al}$ and the roll angle ϕ are shown. The trend of the roll angle is similar to what found with the point mass model (Fig. 4.3b), with a different mean value. The cyclic control of the ailerons makes the windplane to stay airborne and respect the minimum elevation angle

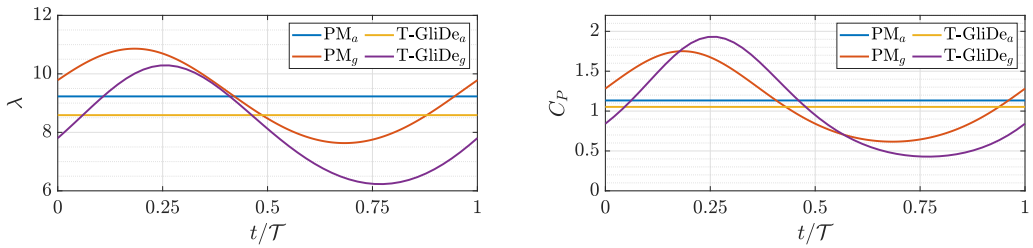

(a) *Wing speed ratio λ as function of non-dimensional time $t/\mathcal{T}$.*

(b) *Power coefficient C_P as function of non-dimensional time $t/\mathcal{T}$.*

Figure 7.2

constraint c_β (Table 7.2). A negative roll angle rotates the lift inwards, to decrease the trajectories radius and thus increase the turning ratio κ_0. This is to reduce the potential energy fluctuating over the loop.

In Fig. 7.3b, the lift coefficient provided by the horizontal stabilizer $C_{L,h}$ (left axis) and pitch angle θ_{rb} (right axis) are shown. The horizontal stabilizer pitch angle θ_h is constant, so the change in lift coefficient is only driven by the change in inflow angle. The change of inflow angle at the horizontal stabilizer is mainly due to the change in wing speed ratio.

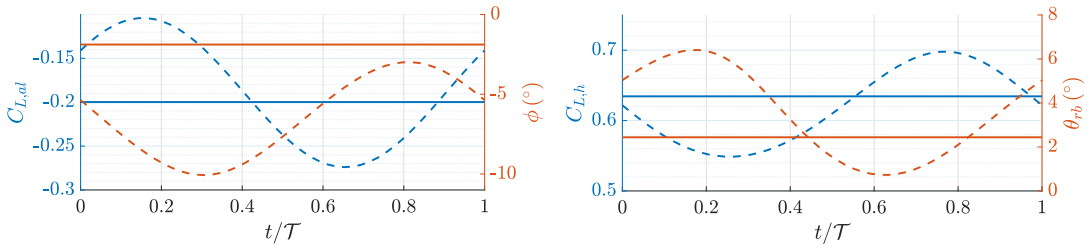

(a) *Differential lift coefficient provided by the ailerons $C_{L,al}$ (left axis) and roll angle ϕ (right axis). OCP T-GliDe$_a$ with continuous lines and OCP T-GliDe$_g$ with dotted lines.*

(b) *Lift coefficient provided by the horizontal stabilizer $C_{L,h}$ (left axis) and pitch angle θ (right axis). OCP T-GliDe$_a$ with continuous lines and OCP T-GliDe$_g$ with dotted lines.*

Figure 7.3

In Fig. 7.4a, the lift coefficient provided by the vertical stabilizer $C_{L,v}$ (left axis) and yaw angle ψ (right axis) are shown. The vertical stabilizer pitch angle θ_v is constant, so the change in lift coefficient is only driven by the change in inflow angle at the vertical tail. The vertical stabilizer lift coefficient has a negative mean value. This is to balance the positive yaw moment induced by the centrifugal force, as shown in Fig. 6.4.

In Fig. 7.4b, the main wing lift coefficients found with the point mass model and with the rigid body model are shown. In the point mass model, the lift coefficient is controlled cyclically, while in T-GliDe it is not. This explains the differences in amplitude and phase. The dynamic problem T-GliDe$_g$ finds an optimal lift coefficient higher than the steady case T-GliDe$_a$. This is also seen with the point mass model in Fig. 4.10b. In this chapter, the control inputs, apart from the ailerons, are trimmed to constant values and the vertical stabilizer is controlled in closed-loop. High power coefficients can be achieved with just a cyclic control of the ailerons and a yaw stability

augmentation system.

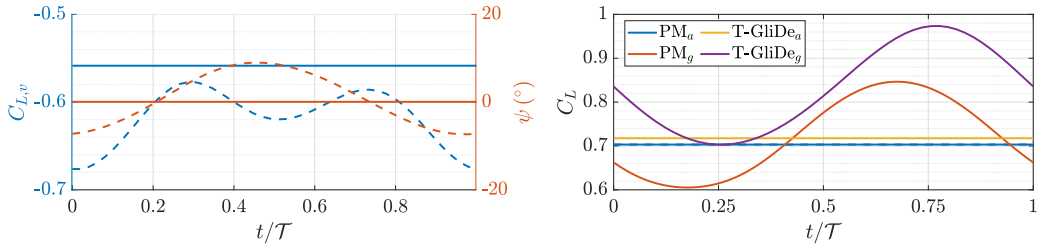

(a) *Lift coefficient provided by the vertical stabilizer $C_{L,v}$ (left axis) and yaw angle ψ (right axis). OCP T-GliDe$_a$ with continuous lines and OCP T-GliDe$_g$ with dotted lines.*

(b) *Main wing lift coefficient C_L as function of non-dimensional time $t/\mathcal{T}$.*

Figure 7.4

Fig. 7.5a shows the tether stress. The point mass under-predicts the fluctuations of the forces acting on the tether. This is because of the assumption of lateral equilibrium and circular trajectories in the point mass model.

The axial induction a for both models is shown in Fig. 7.5b. In the point mass model, the optimal induction a is found to be constant (Eq. 4.46). With the rigid body model, considering constant control inputs, the optimal induction a fluctuates. The power coefficient decreases of a small quantity when including gravity (i.e. passing from the aerodynamic to the dynamic OCPs). Therefore, the sensitivity of the power coefficient with respect to the longitudinal cyclic controls (a_t, θ_h) and to the vertical stabilizer (θ_v) is found to be small.

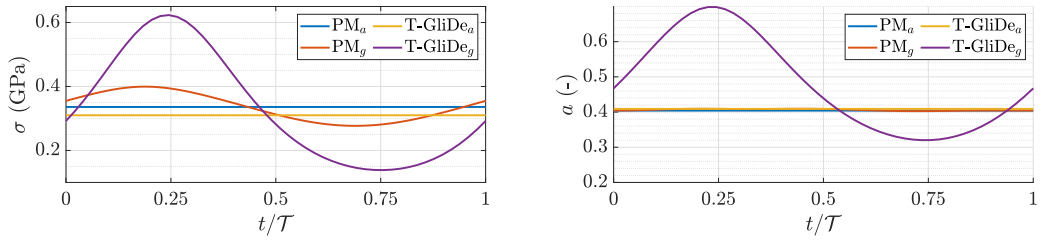

(a) *Tether stress σ as function of non-dimensional time $t/\mathcal{T}$.*

(b) *Axial induction a as a function of the non-dimensional time $t/\mathcal{T}$.*

Figure 7.5

In Fig. 7.6a, the power balances of the two models are shown for the aerodynamic case. As in these OCPs the gravity is set to zero, the problem is just an aerodynamic problem, where $C_a = -\frac{C_P}{1-a_t}$. The wind power $C_T(1-a)$ is also shown. The difference between the wind power and the aerodynamic power is the power dissipated in parasite drag $C_\tau = C_T(1-a) - C_a$ (Eq. 7.21).

In Fig. 7.6b, the power balances for the cases including gravity is shown. The wind-plane accelerates due to gravity gravitational power C_g, changing its kinetic energy e_k. Since the horizontal stabilizer is trimmed, the aerodynamic power C_a is not controlled cyclically. Therefore, it fluctuates. The onboard turbines thrust powers $\frac{C_P}{1-a_t}$ predicted by the two models have however a similar trend.

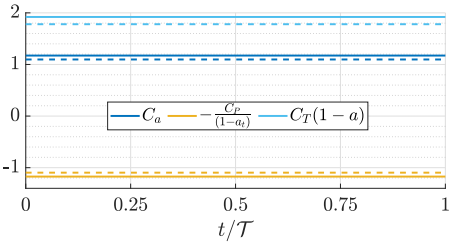

(a) *Non-dimensional power balance as function of non-dimensional time $t/\mathcal{T}$ for the steady aerodynamic case. The continuous line refers to the point mass model PM$_a$, while the dotted line to the rigid body model T-GliDe$_a$.*

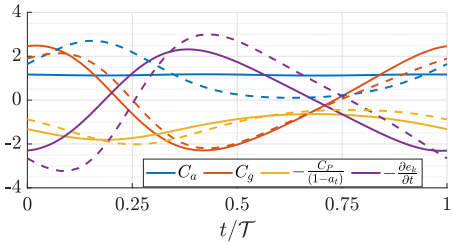

(b) *Non-dimensional power balance as function of non-dimensional time $t/\mathcal{T}$ for the dynamic case including gravity. The continuous line refers to the point mass model PM$_g$, while the dotted line to the rigid body model T-GliDe$_g$.*

Figure 7.6

In Fig. 7.7a, the opening angle predicted by the two models is shown. A constant opening angle Φ is assumed in the point mass model. In the problem T-GliDe$_g$, the optimal trajectory has an optimal lower opening angle (hence higher κ_0) to reduce the trajectory radius and thus the potential energy exchanged. In Fig. 7.7b, the time derivative of the azimuth angle $\dot{\Psi}$ and the yaw rate r are shown. They have a similar trend and magnitude.

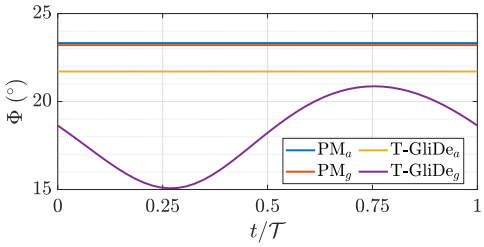

(a) *Opening angle Φ as function of non-dimensional time $t/\mathcal{T}$.*

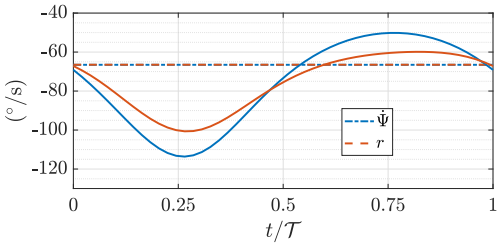

(b) *Time derivative of the azimuth angle $\dot{\Psi}$ and the yaw rate r as function of non-dimensional time $t/\mathcal{T}$. The dotted lines refer to the aerodynamic case T-GliDe$_a$, while the continuous lines to the dynamic case T-GliDe$_g$.*

Figure 7.7

Finally, the linear velocities v and w are shown in Fig. 7.8a and the angular velocities p and q are shown in Fig. 7.8b. The fluctuations are small compared to the longitudinal velocity $u = \lambda v_w$ and to the yaw rate r. Recall that the aerodynamic model is linearized with respect to $(v, w, p, q, \phi, \theta, \psi)$, which seems reasonable.

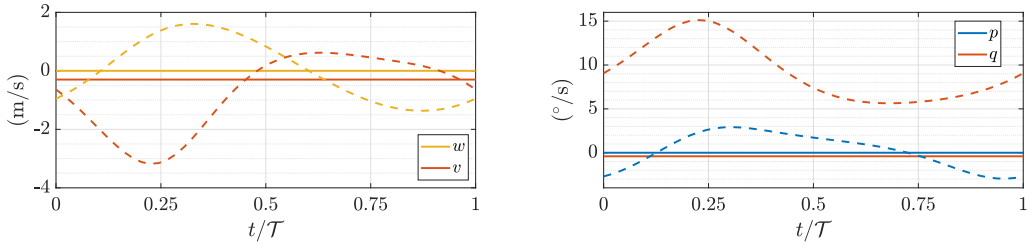

(a) *Linear velocities v and w as function of non-dimensional time $t/\mathcal{T}$. The continuous line refers to the aerodynamic case T-GliDe$_a$, while the dotted line to the dynamic case T-GliDe$_g$.*

(b) *Angular velocities p and q as function of non-dimensional time $t/\mathcal{T}$. The continuous line refers to the aerodynamic case T-GliDe$_a$, while the dotted line to the dynamic case T-GliDe$_g$.*

Figure 7.8

7.7 Discussion

In this chapter, the optimization problem implemented in T-GliDe (Tethered Gliding system Design) is formulated and optimal trajectories are analyzed.

T-GliDe is a multidisciplinary design, analysis and optimization framework for windplanes. The current version of T-GliDe involves a structural model (Appendix C), a aerodynamic model (Chap. 3 and 6), an optimal control formulation based on a harmonic balance method, and an economic model (Chap. 9). The gradient-descendant optimizer solves all disciplines at the same time ("all-at-once" formulation), enabling the use of automatic differentiation. An uncertainty quantification toolbox is also linked to the optimization framework to study how uncertainties propagate throughout the design process.

In this chapter, T-GliDe is used to solve two optimal control problems OCPs at a low wind speed of $v_w = 5$ m/s. The first OCP is an open-loop aerodynamic steady problem, where the gravity is set to zero $g = 0$. The second OCP is a closed-loop dynamic problem, which includes gravity. The onboard turbines axial induction a_t and the horizontal and vertical stabilizers pitch angles (θ_h, θ_v) are trimmed to constant values to study a baseline trajectory. The ailerons are actuated cyclically to control the roll angle. The cyclic control of the roll angle redirects the lift to compensate gravity and thus to stay airborne. The vertical stabilizer is controlled in closed loop to augment stability. This is discussed in the next chapter. A small reduction in power coefficient between the steady aerodynamic case and the dynamic case is found. Therefore, the sensitivity of the power coefficient with respect to the control inputs $(a_t, \theta_h, \theta_v)$ is found to be small. A rigorous validation of these results is still to be done.

The assumptions of the models employed in T-GliDe ultimately define the applicability of the results. The equations of motion describe the rigid body motion, thus neglecting aero-elastic effects. The linearized aerodynamic model, using the assumptions listed in Sect. 6.10, is challenged when the optimal trajectory deviates significantly from a circular trajectory, which does not seem the case for the current example. Since the sensitivity of the power coefficient with respect to the longitudinal controls is small, to maintain a constant induction over the trajectory, as found with the point mass model, is found to be not necessary to maintain high lift coefficients. Similar results are expected for Ground-Gen AWESs as the flight dynamics is similar.

7.8 State of the art and open questions

The state of the art of the optimal control problems and of the optimal design problems is given in Sect. 4.11.

A preliminary version T-GliDe was introduced by Trevisi et al. (2022b), where a global sensitivity analysis of a set candidate design variables on the eigendynamics was performed. The results presented in this chapter are produced for this thesis and will be published in the future. They need to be validated. Many research questions on optimal designs will be addressed with T-GliDe in the future.

CHAPTER 8

Flight stability

An asymptotically stable windplane returns back to the periodic trajectory after a perturbation from an external disturbance. The main disturbance is expected to be the wind turbulence. A good windplane design should be open-loop asymptotically stable, or at least open-loop simply stable. This relieve the closed-loop control design from the task of stabilizing the system. Closed-loop control can be anyway used to increase stability.

The stability of a nonlinear periodic dynamic problem should be evaluated with Floquet theory or similar methods. If gravity is neglected, the trimmed solution is steady and its aerodynamic quantities are similar to the mean quantities obtained including gravity. The flight dynamics about the trimmed steady problem is then considered representative of the flight dynamics over the loop. In this chapter, the flight dynamics is modeled as a linear time invariant system about the steady solution and the eigendynamics is studied.

8.1 Representative point

The generic state vector defining the windplane dynamics is

$$\boldsymbol{y} = \big[\underbrace{u,\ v,\ w}_{\boldsymbol{v}},\ \underbrace{p,\ q,\ r}_{\boldsymbol{\omega}},\ \underbrace{\phi,\ \theta_{rb},\ \psi}_{\boldsymbol{eu}},\ \underbrace{\Psi,\ \Phi,\ L_{te}}_{\boldsymbol{x}}\big]^T, \tag{8.1}$$

which we want to write as

$$\boldsymbol{y} = \boldsymbol{y}_0 + \Delta\boldsymbol{y}. \tag{8.2}$$

where $\boldsymbol{y}_0$ describes the representative point and $\Delta\boldsymbol{y}$ the perturbation.

The representative state is

$$\boldsymbol{y}_0 = \big[\underbrace{\underbrace{u_0,\ 0,\ 0}_{\boldsymbol{v}_0},\ \underbrace{0,\ 0,\ r_0}_{\boldsymbol{\omega}_0}}_{\mathrm{v}_0},\ 0,\ \theta_{rb,0},\ 0,\ 0,\ \Phi_0,\ L_{te}\big]^T, \tag{8.3}$$

where we consider the non-null states of the representative point as the values of the aerodynamic optimal control problem T-GliDe$_a$.

Taking $\theta_{bs} = -\theta_{rb,0}$, the incremental state $\Delta\boldsymbol{y}$ is

$$\Delta\boldsymbol{y} = \big[\underbrace{\underbrace{\Delta u,\ v,\ w}_{\Delta\boldsymbol{v}},\ \underbrace{p,\ q,\ \Delta r}_{\Delta\boldsymbol{\omega}}}_{\Delta\mathrm{v}},\ \underbrace{\phi,\ \theta,\ \psi}_{\boldsymbol{eu}},\ \Psi,\ \Delta\Phi,\ \Delta L_{te}\big]^T, \tag{8.4}$$

where $\theta = \theta_{rb} - \theta_{rb,0} = \theta_{rb} + \theta_{bs} = \theta_{rs}$.

The time derivative of the state vector is

$$\dot{\boldsymbol{y}} = \big[\underbrace{\underbrace{\dot{u},\ \dot{v},\ \dot{w}}_{\dot{\boldsymbol{v}}},\ \underbrace{\dot{p},\ \dot{q},\ \dot{r}}_{\dot{\boldsymbol{\omega}}}}_{\dot{\mathrm{v}}},\ \underbrace{\dot{\phi},\ \dot{\theta},\ \dot{\psi}}_{\dot{\boldsymbol{eu}}},\ \dot{\Psi},\ \dot{\Phi},\ \dot{L}_{te}\big]^T, \tag{8.5}$$

which we write as

$$\dot{\boldsymbol{y}} = \dot{\boldsymbol{y}}_0 + \Delta\dot{\boldsymbol{y}}. \tag{8.6}$$

The time derivative of the state at the representative point $\dot{\boldsymbol{y}}_0$ is

$$\dot{\boldsymbol{y}}_0 = \big[0,\ 0,\ 0,\ 0,\ 0,\ 0,\ 0,\ 0,\ 0,\ \dot{\Psi}_0,\ 0,\ 0\big]^T, \tag{8.7}$$

and the incremental state $\Delta\dot{\boldsymbol{y}}$ is

$$\Delta\dot{\boldsymbol{y}} = \big[\dot{u},\ \dot{v},\ \dot{w},\ \dot{p},\ \dot{q},\ \dot{r},\ \dot{\phi},\ \dot{\theta},\ \dot{\psi},\ \Delta\dot{\Psi},\ \dot{\Phi},\ \dot{L}_{te}\big]^T, \tag{8.8}$$

We now want to linearize the equations of motion and the external forces about the representative point $\boldsymbol{y}_0$.

8.2 Linearized equations of motion

The equations of motion are linearized about the reference condition as

$$\frac{\mathbf{S}^{-1}}{\mathrm{F}}\mathbf{m}\dot{\mathrm{v}} + \frac{\mathbf{S}^{-1}}{\mathrm{F}}\mathrm{v}_0^{\times}\mathbf{m}\mathrm{v}_0 + \frac{\mathbf{S}^{-1}}{\mathrm{F}}\Delta\mathrm{v}^{\times}\mathbf{m}\mathrm{v}_0 + \frac{\mathbf{S}^{-1}}{\mathrm{F}}\mathrm{v}_0^{\times}\mathbf{m}\Delta\mathrm{v} = \boldsymbol{f}_0 + \Delta\boldsymbol{f}, \tag{8.9}$$

where $\Delta\mathrm{v} = \mathrm{v} - \mathrm{v}_0$, $\mathbf{m}$ and $\mathrm{v}^{\times}$ are given in Eq. (5.6), the diagonal matrix is given in Eq. (6.6) and

$$\mathbb{F} = \frac{1}{2}\rho A u_0^2. \tag{8.10}$$

The third term in the latter form can be expressed as a function of the incremental velocity $\Delta\mathrm{v}$ as

$$\Delta\mathrm{v}^{\times}\mathbf{m}\mathrm{v}_0 = \begin{bmatrix} \Delta\boldsymbol{\omega}^{\times} & \mathbf{0} \\ \Delta\boldsymbol{v}^{\times} & \Delta\boldsymbol{\omega}^{\times} \end{bmatrix}\begin{pmatrix} \mathbf{c}_0 \\ \mathbf{d}_0 \end{pmatrix} = -\begin{bmatrix} \mathbf{0} & \mathbf{c}_0^{\times} \\ \mathbf{c}_0^{\times} & \mathbf{d}_0^{\times} \end{bmatrix}\begin{pmatrix} \Delta\boldsymbol{v} \\ \Delta\boldsymbol{\omega} \end{pmatrix} = -\mathbf{c}\mathbf{d}_0^{\times}\Delta\mathrm{v}. \tag{8.11}$$

Upon substitution, the linearized part of the equation of motion is

$$\frac{\mathbf{S}^{-1}}{\mathtt{F}}\Delta\mathtt{v}^{\times}\mathbf{m}\mathtt{v}_0 + \frac{\mathbf{S}^{-1}}{\mathtt{F}}\mathtt{v}_0^{\times}\mathbf{m}\Delta\mathtt{v} = -\frac{\mathbf{S}^{-1}}{\mathtt{F}}\left(\mathbf{c}\mathtt{d}_0^{\times} - \mathtt{v}_0^{\times}\mathbf{m}\right)\Delta\mathtt{v} = -\mathbf{A}_{\mathbf{c}}\Delta\mathtt{v}. \tag{8.12}$$

The linearized equation of motion (Eq. 8.9) can be then written as

$$\frac{\mathbf{S}^{-1}}{\mathtt{F}}\mathbf{m}\dot{\mathtt{v}} = \left(\boldsymbol{f}_0 - \frac{\mathbf{S}^{-1}}{\mathtt{F}}\mathtt{v}_0^{\times}\mathbf{m}\mathtt{v}_0\right) + \mathbf{A}_{\mathbf{c}}\Delta\mathtt{v} + \Delta\boldsymbol{f}, \tag{8.13}$$

8.3 Kinematic constraints: linear velocity

The kinematic constraints of the linear velocity are given in Sect. 5.3. We now need to linearize them.

We recall that $\mathbf{R}_{TeR} = \mathbf{R}_x(-\Phi)$, such that its perturbation is

$$\Delta\mathbf{R}_{TeR} = \left.\frac{\partial\mathbf{R}_{TeR}}{\partial\Phi}\right|_{\Phi=\Phi_0}\Delta\Phi = \begin{bmatrix} 0 & 0 & 0 \\ 0 & \sin\Phi_0 & \cos\Phi_0 \\ 0 & -\cos\Phi_0 & \sin\Phi_0 \end{bmatrix}\Delta\Phi \tag{8.14}$$

We write the linear version of the left-hand-side of Eq. 5.8 $\boldsymbol{v}_{GS}^{Te} = \mathbf{R}_{TeR}\mathbf{R}_{RS}\boldsymbol{v}$ as

$$\begin{aligned}\Delta\boldsymbol{v}_{GS}^{Te} &= \Delta\mathbf{R}_{TeR}\boldsymbol{v}_0 + \mathbf{R}_{TeR}(\Phi_0)\Delta\mathbf{R}_{RS}\boldsymbol{v}_0 + \mathbf{R}_{TeR}(\Phi_0)\Delta\boldsymbol{v} \\ &= -\mathbf{R}_x(-\Phi_0)\boldsymbol{v}_0^{\times}\boldsymbol{e}\boldsymbol{u} + \mathbf{R}_x(-\Phi_0)\Delta\boldsymbol{v}\end{aligned} \tag{8.15}$$

where $\Delta\mathbf{R}_{RS}^{R} = \boldsymbol{e}\boldsymbol{u}^{\times}$ and $\Delta\mathbf{R}_{TeR}\boldsymbol{v}_0 = \mathbf{0}$.

The linear version of the right-hand-side of Eq. 5.8 is

$$\begin{aligned}\Delta\boldsymbol{v}_{GS}^{Te} &= \begin{bmatrix} -L_{te}\Delta\dot{\Psi}\sin\Phi_0 - L_{te}\dot{\Psi}_0\cos\Phi_0\Delta\Phi \\ L_{te}\Delta\dot{\Phi} \\ \Delta\dot{L}_{te} \end{bmatrix} \\ &= \begin{bmatrix} 0 & -L_{te}\dot{\Psi}_0\cos\Phi_0 & 0 \\ 0 & 0 & 0 \\ 0 & 0 & 0 \end{bmatrix}\begin{bmatrix} 0 \\ \Delta\Phi \\ 0 \end{bmatrix} + \begin{bmatrix} -L_{te}\sin\Phi_0 & 0 & 0 \\ 0 & L_{te} & 0 \\ 0 & 0 & 1 \end{bmatrix}\begin{bmatrix} \dot{\Psi} \\ \Delta\dot{\Phi} \\ \dot{L}_{te} \end{bmatrix}\end{aligned} \tag{8.16}$$

8.4 Kinematic constraints: angular velocity

The kinematic constraints of the linear velocity are given in Sect. 5.4. Equation (5.10) can be linearized as

$$\Delta\boldsymbol{\omega} = (-\theta\boldsymbol{e}_2^{\times} - \phi\boldsymbol{e}_1^{\times})\begin{bmatrix} 0 \\ 0 \\ \dot{\Psi}_0 \end{bmatrix} + \begin{bmatrix} 0 \\ 0 \\ \Delta\dot{\Psi} + \Delta\dot{\psi} \end{bmatrix} + \begin{bmatrix} \Delta\dot{\phi} \\ 0 \\ 0 \end{bmatrix} + \begin{bmatrix} 0 \\ \Delta\dot{\theta} \\ 0 \end{bmatrix}, \tag{8.17}$$

which can be re-organized as

$$\begin{bmatrix} 0 \\ 0 \\ \Delta\dot{\Psi} \end{bmatrix} + \begin{bmatrix} \dot{\phi} \\ \dot{\theta} \\ \dot{\psi} \end{bmatrix} = \begin{bmatrix} p \\ q \\ \Delta r \end{bmatrix} - \begin{bmatrix} 0 \\ 0 \\ \dot{\Psi}_0 \end{bmatrix}^{\times}\begin{bmatrix} \phi \\ \theta \\ \psi \end{bmatrix}. \tag{8.18}$$

8.5 Linearized dynamics: explicit formulation

Based on the linearization just introduced, the linearized dynamics of the system can be written as

$$\mathbf{M}\Delta\dot{\boldsymbol{y}} = \mathbf{A}_{eq}\Delta\boldsymbol{y} + \frac{\partial \boldsymbol{f}_a}{\partial \boldsymbol{y}}\Delta\boldsymbol{y} + \frac{\partial \boldsymbol{f}_a}{\partial \dot{\boldsymbol{y}}}\Delta\dot{\boldsymbol{y}}. \tag{8.19}$$

In this expression, the mass matrix $\mathbf{M}$ writes

$$\mathbf{M} = \begin{bmatrix} \frac{\mathbf{S}^{-1}}{\mathrm{F}}\mathbf{m} & \mathbf{0}_{6\times3} & \mathbf{0}_{6\times3} \\ \cdots & \cdots & \cdots \\ \mathbf{0}_{3\times3} & \mathbf{0}_{3\times3} & \mathbf{0}_{3\times3} \\ \cdots & \cdots & \cdots \\ \mathbf{0}_{3\times3} & \mathbf{0}_{3\times3} & \mathbf{1}_{3\times3} \end{bmatrix} \quad \begin{matrix} -L_{te}\sin\Phi_0 & 0 & 0 \\ 0 & L_{te} & 0 \\ 0 & 0 & 1 \\ \cdots & \cdots & \cdots \\ 0 & 0 & 0 \\ 0 & 0 & 0 \\ 1 & 0 & 0 \end{matrix}, \tag{8.20}$$

with $\mathbf{1}_{3\times3}$ is a 3 by 3 identity matrix. The coefficient matrix $\mathbf{A}_{eq}$ can be written as

$$\mathbf{A}_{eq} = \begin{bmatrix} \mathbf{A_c} & \mathbf{0}_{6\times3} & \mathbf{0}_{6\times3} \\ \cdots & \cdots & \cdots \\ \mathbf{R}_x(-\Phi_0) & \mathbf{0}_{3\times3} & -\mathbf{R}_x(-\Phi_0)\boldsymbol{v}_0^{\times} \\ \cdots & \cdots & \cdots \\ \mathbf{0}_{3\times3} & \mathbf{1}_{3\times3} & -\dot{\Psi}_0\boldsymbol{e}_3^{\times} \end{bmatrix} \quad \begin{matrix} 0 & L_{te}\dot{\Psi}_0\cos\Phi_0 & 0 \\ 0 & 0 & 0 \\ 0 & 0 & 0 \\ \cdots & \cdots & \cdots \\ & \mathbf{0}_{3\times3} & \end{matrix}. \tag{8.21}$$

The external force matrix $\mathbf{A}_f$ is instead used to describe the linear variation of the external forces with respect to a variation of the state space variables. As a further step in dealing with dynamic equations, the system of linearized equations can be made non-dimensional. This is achieved by normalizing the state variables according to dimensional groups typically found in flight mechanics literature. In the process, a diagonal matrix $\mathbf{S}_y$ is defined as

$$\mathbf{S}_y = diag\left(\left[u_0,\ u_0,\ u_0,\ \frac{2u_0}{b},\ \frac{2u_0}{c},\ \frac{2u_0}{b},\ 1,\ 1,\ 1,\ 1,\ 1,\ 1\right]\right). \tag{8.22}$$

We use the inverse of $\mathbf{S}_y$ to define the non-dimensional state vector

$$\tilde{\boldsymbol{y}} = \mathbf{S}_{\boldsymbol{y}}^{-1}\Delta\boldsymbol{y} = \Big[\underbrace{\frac{\Delta u}{u_0},\ \frac{v}{u_0},\ \frac{w}{u_0}}_{\tilde{\boldsymbol{v}}},\ \underbrace{\frac{pb}{2u_0},\ \frac{qc}{2u_0},\ \frac{\Delta rb}{2u_0}}_{\tilde{\boldsymbol{\omega}}},\ \underbrace{\phi,\ \theta,\ \psi}_{\boldsymbol{eu}},\ \underbrace{\Psi,\ \Phi,\ L_{te}}_{\boldsymbol{x}}\Big]^T. \tag{8.23}$$

The linearized dynamic problem in Eq. (8.19) can be expressed with respect to the non dimensional state as

$$\mathbf{M}\mathbf{S}_y\dot{\tilde{\boldsymbol{y}}} - \frac{\partial \boldsymbol{f}_a}{\partial \dot{\tilde{\boldsymbol{y}}}}\dot{\tilde{\boldsymbol{y}}} = \mathbf{A}_{eq}\mathbf{S}_y\tilde{\boldsymbol{y}} + \frac{\partial \boldsymbol{f}_a}{\partial \tilde{\boldsymbol{y}}}\tilde{\boldsymbol{y}} \tag{8.24}$$

The linear problem can be finally written as

$$\dot{\tilde{\boldsymbol{y}}} = \tilde{\mathbf{A}}\tilde{\boldsymbol{y}}, \tag{8.25}$$

where the linear matrix $\tilde{\mathbf{A}}$ is

$$\tilde{\mathbf{A}} = \text{inv}\left(\mathbf{M}\mathbf{S}_y - \frac{\partial \boldsymbol{f}_a}{\partial \tilde{\boldsymbol{y}}}\right)\left(\mathbf{A}_{eq}\mathbf{S}_y, + \frac{\partial \boldsymbol{f}_a}{\partial \tilde{\boldsymbol{y}}}\right). \tag{8.26}$$

The aerodynamic derivatives term $\frac{\partial \boldsymbol{f}_a}{\partial \tilde{\boldsymbol{y}}}$ can be taken from the linearized model derived in Chapter 6 (Eq. 6.7) and the aerodynamic derivaties term $\frac{\partial \boldsymbol{f}_a}{\partial \tilde{\boldsymbol{y}}}$ from the feedback control formulation in Sect. 7.4.

8.6 Windplane eigendynamics

The state vector characterizing the dynamics $\tilde{\boldsymbol{y}}$ has 12 dimensions, so the linearized dynamics has 12 eigenmodes and 12 eigenvalues. Since gravity is removed from the modeling, the dynamics is not influenced by the azimuth position Ψ. Moreover, the state related to the tether elongation L_{te} is constrained. Therefore only 10 states are actually entering the dynamical problem. We then find 10 eigenvalues different from zero. In Figure 8.1, the open-loop eigenvalues in the complex plane are shown. In Table 8.1, the eigenvalues are given, together with their correspondent eigenfrequency f_n, damping ratio ζ and time to halve $t_{1/2}$ for the open-loop and for the closed-loop case. The plane is controlled in closed-loop with the yaw stability augmentation system proposed in Sect. 7.4.

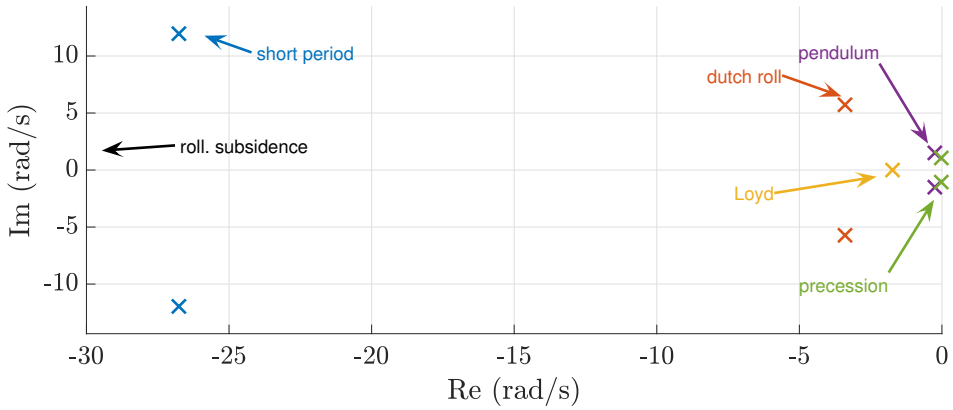

Figure 8.1: *Open-loop eigenvalue position in the complex plane.*

The roll subsidence is a real fast mode. In Table 8.2 the components of its eigenvector, normalized with the largest value, are shown. The roll subsidence eigenmode mainly involves the roll rate $\tilde{p}$ and the roll angle ϕ, as for airplanes.

The other eigenmode with real eigenvalue is the Loyd mode (named after Miles L. Loyd (1980)). The Loyd mode involves mainly the lateral variables $(\tilde{v}, \phi, \psi)$, typical of the spiral mode for airplanes, and the longitudinal velocity $\tilde{u}$. The longitudinal velocity in equilibrium is given by the balance of the projection of lift along the $\boldsymbol{e}_{1,s}$ axis and drag. When $\tilde{u}$ is perturbed, the plane tends to go back to the equilibrium point. A

	open-loop				closed-loop			
mode	eigenvalue	f_n (Hz)	ζ	$t_{1/2}$ (s)	eigenvalue	f_n (Hz)	ζ	$t_{1/2}$ (s)
Roll	-54	-	-	0.013	-54	-	-	0.013
Short period	$-26.8 \pm 12.0i$	4.6	0.91	0.026	$-26.8 \pm 12.0i$	4.6	0.91	0.026
Dutch roll	-3.4 ± 5.7	1.06	0.51	0.20	4.96 ± 4.11	1.03	0.77	0.14
Loyd	-1.73	-	-	0.40	-2.05	-	-	0.34
Pendulum	$-0.25 \pm 1.50i$	0.24	0.16	2.77	$-0.15 \pm 1.53i$	0.24	0.10	4.5
Precession	$-0.02 \pm 1.06i$	0.17	0.021	31.6	$-0.12 \pm 1.00i$	0.16	0.12	5.58

Table 8.1: *Eigenvalues, eigenfrequency, damping ratio and time to halve of the windplanes eigendynamics evaluated with and without yaw SAS.*

state	$\tilde{u}$	$\tilde{v}$	$\tilde{w}$	$\tilde{p}$	$\tilde{q}$	$\tilde{r}$	ϕ	θ	ψ	$\Delta\Phi$
Roll	-0.0035	-0.0617	-0.0122	-1.0000	-0.0090	-0.1251	0.1594	0.0033	0.0200	0.0004
Loyd	-0.6737	-0.4349	-0.1623	0.1728	0.0059	-0.1409	-0.6550	0.2992	1.0000	-0.0875

Table 8.2: *Eigenmode for the two real negative eigenvalues.*

graphical representation of this part of the mode is given in Figure 8.2. In the figure, the windplane velocity is decreased of Δu, such that the inflow angle γ_a is increased with respect to the steady state value ($\gamma_a' > \gamma_a$). Since lift is perpendicular to the apparent wind speed, a positive force ΔX along the $\boldsymbol{e}_{1,s}$ axis is generated. This force acts to restore the equilibrium condition.

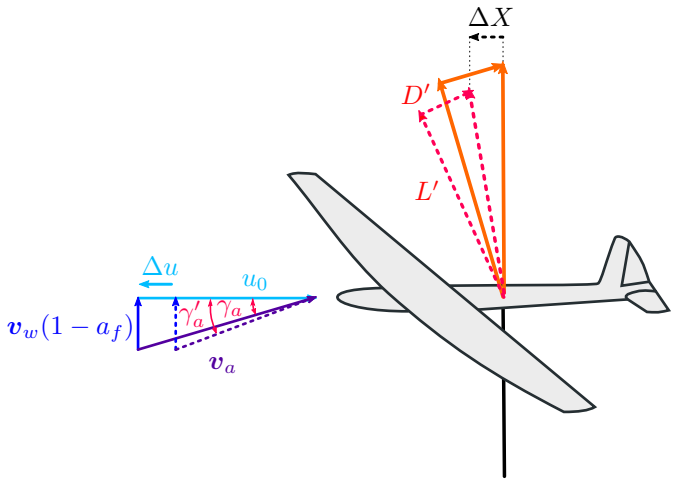

Figure 8.2: *Graphical representation of the longitudinal part of the Loyd mode.*

The short period is a fast oscillating mode with a high damping ratio. Its eigenmode is shown in Fig. 8.3a. It involves mainly longitudinal states ($\tilde{w}$, $\tilde{q}$, θ), as for airplanes, and the roll rate $\tilde{p}$. The dutch roll is also a fast oscillating mode with a relative high damping ratio. Its eigenmode is shown in Fig. 8.3b. It involves mainly the lateral states ($\tilde{v}$,$\tilde{p}$,$\tilde{r}$, ϕ,ψ), as for airplanes.

The pendulum is slow oscillating mode with low damping ratio typical of windplanes, shown in in Fig. 8.4a. The pendulum involves the linear velocities $\tilde{w}$, all the Euler angles (ϕ, θ, ψ) and the opening angle $\Delta\Phi$. There is a phase difference of approx $\pi/2$ between the roll angle and the opening angle ($\Delta\Phi, \phi$) and ($\tilde{w}, \theta, \psi$). The pendulum

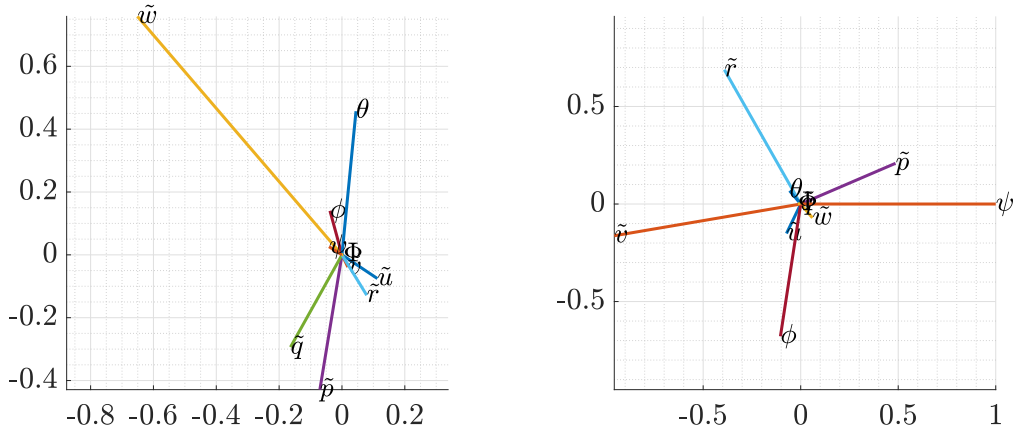

(a) *Open-loop short period eigenmode in the complex plane.* **(b)** *Open-loop dutch roll eigenmode in the complex plane.*

Figure 8.3

damping is strongly influenced by the main wing dihedral angle. This is the reason for taking a dihedral angle of $\Gamma = -20°$.

The precession eigenmode in open-loop has an almost null real part, meaning that it is an oscillatory mode lightly damped. The damping is due to the derivative of the tether aerodynamic force with respect to the yaw angle $\frac{\partial \boldsymbol{f}_{te}}{\partial \psi}$ (Eq. 6.80). Controlling the vertical stabilizer proportionally to the time derivative of the yaw, as proposed in Sec. 7.4, increases the damping of this mode (Table 8.1).

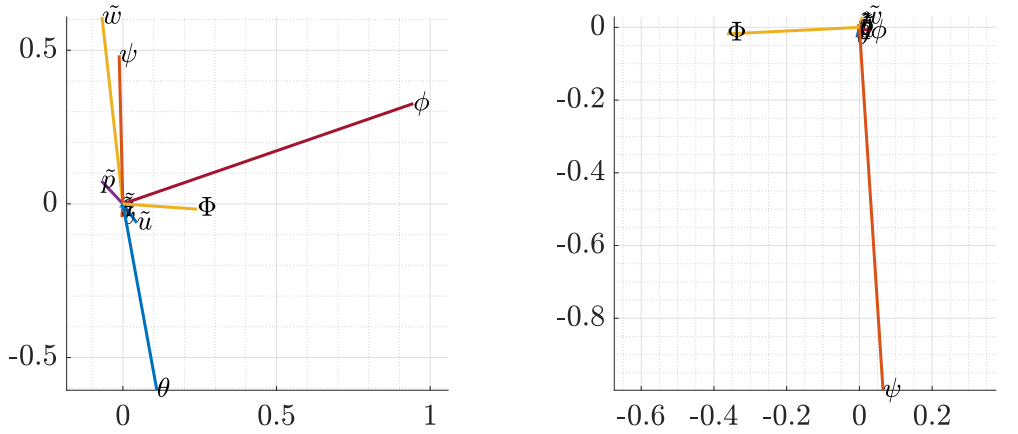

(a) *Open-loop pendulum eigenmode in the complex plane.* **(b)** *Open-loop precession eigenmode in the complex plane.*

Figure 8.4

Figure 8.5 shows a graphical illustration of the precession mode. The plane precesses by making the opening angle Φ and the azimuth position Ψ (this is not shown in the figure for simplicity) to oscillate. Since the plane aerodynamics is not influencing this mode, the aerodynamic velocity triangle remains constant and the yaw angle ψ is settled such that the velocity along the $\boldsymbol{e}_{2,s}$ direction (i.e. the side-slip) is constant.

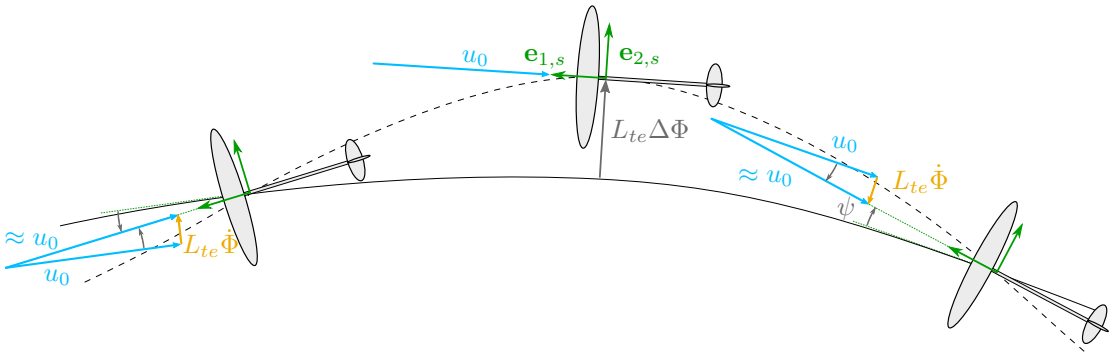

Figure 8.5: *Graphical representation of the precession mode.*

8.7 Discussion

In this chapter, the eigendynamics of the light windplane designed in Chap. 4 is investigated. The windplane dynamics is modeled as a linear time invariant system about the trimmed steady solution obtained by neglecting gravity. As the steady solution involves a constant turning maneuver, the longitudinal and lateral equations of motion are coupled. The dynamic problem is characterized by 12 states, of which 10 are actually entering the linear problem. Therefore, 10 non-null eigenvalues are found.

The roll and the Loyd modes are real stable eigenmodes. The longitudinal part of the Loyd mode brings the plane back to the equilibrium longitudinal velocity after a perturbation.

Four oscillating modes are found. The short period and the dutch roll are modes typical of airplanes, which are modified by the presence of the tether and the constant turning maneuver. The pendulum eigenmode is a lightly damped mode typical of windplanes. The precession eigenvalue has an almost null real part in open-loop. The little open-loop damping of this mode is exclusively due to the derivative of the tether drag with respect to the yaw angle. Controlling in closed-loop the vertical stabilizer proportionally to the time derivative of the yaw increases the damping of the precession mode. A rigorous validation of these results is still to be done.

The flight stability of the non-linear trajectory needs to be evaluated with rigorous methods (e.g. Floquet theory), which will ultimately prove its stability. However, the linear time-invariant approximation about aerodynamic steady trajectories is an invaluable tool to understand the system dynamics and to develop closed-loop control strategies. Similar results are expected for Ground-Gen AWESs as the flight dynamics is similar.

8.8 State of the art and open questions

Houska and Diehl (2010) look for the open-loop stability of a soft kites for airborne wind energy flying figure of eights. They find that open-loop stable trajectories can be obtained with a considerable power loss. Later, Sternberg et al. (2012) robustify these open-loop stable trajectories with respect to wind turbulence. Terink et al. (2011) fly an experimental inflatable kite from Tu Delft group, which suffers from pendulum instability in crosswind mode. They then find that the dihedral angle and the vertical

stabilizer area are most influencing this mode.

Salord Losantos and Sánchez-Arriaga (2015) study the stability of the periodic kite motion around the vertical equilibrium with Floquet theory and Pastor-Rodríguez et al. (2017) investigate the longitudinal stability of kites in this condition. Sánchez-Arriaga et al. (2017) study the flight stability of a two-lines kite fling crosswind figure-of-eight trajectories. They find that the effective dihedral largely impacts the lateral kite dynamics.

Makani Power, before the shutdown, started investigating the possibility of designing the flight path and aerodynamic characteristics of the AWES to achieve passive stability (Homsy (2020); Sicard et al. (2020)). Stable AWESs would maintain the flight path with the least amount of control activity.

Trevisi et al. (2021a) study the linear stability about the axial-symmetric trajectory obtained by neglecting the gravity. In populating the linearized dynamic model, analytical derivatives of external forces are computed, allowing for a fast formulation of the linearized problem and for a quantitative understanding of how design parameters influence stability. A complete eigenanalysis is carried out, showing that a stable-by-design windplane can be obtained and how. It is shown how conventional airplanes eigenmodes are modified for a windplane. The pendulum eigenmode has the lowest damping ratio. The Loyd mode is found and its physical interpretation given. Trevisi et al. (2022b) performs a global sensitivity analysis of the eigenvalues with respect to a set of independent variables using the uncertainty quantification toolbox in T-GliDe. The pendulum eigenmode is found to be largely influenced by the dihedral angle and the vertical stabilizer area. This study served the design of the dihedral angle and the vertical stabilizer area carried out in this thesis. The pendulum is found to be almost not sensitive to the moments of inertia. This justifies the simple model used to estimate the inertia from a given mass of this thesis (Appendix C). A sensitivity analysis on the eigendynamics of the optimal windplane will be carried out in the future. The precession mode is found while producing this thesis and its feed-back control designed consequently. In future version of T-GliDe, the damping ratios will enter the optimization problem as inequality constraints to design for stability.

CHAPTER 9

Economics

For a successful diffusion of airborne wind energy (AWE) in the energy sector, the development of the technology should be aligned with the needs dictated by the market. Every market has different characteristics which can be suitable for different AWE concepts. For example, soft-wing and fixed-wing systems, depending on the wind and site requirements, replacement costs, operation & maintenance costs, etc., could be suitable for different markets. Such trade-offs could only be evaluated by employing an economic model along with a performance model.

The IEA Wind Task 48 (Airborne Wind Europe (2023a)) aims at building a strong community that works together to accelerate the development and commercialization of AWE technology. Within this IEA Wind Task, Rishikesh Joshi, PhD student at TU Delft, and I have initiated the development of a reference open-source economic model, which researchers and companies can use to assess the performances of their AWE concepts for different market scenarios. This work falls under Work Package 1, which focuses on identifying economic drivers and the potential of deploying AWE in different markets.

The primary aspect of the economic model is the cost modeling of different concepts where we build cost functions parametric to key design parameters such as the kite wing area, span, aspect ratio, tether force, generator characteristics, etc. The process of developing this model is shown in Fig. 9.1. We developed a first version of the economic report (Joshi and Trevisi (2023)), which was provided to participants together with an individual spreadsheets. Participants were asked to fill the report and the spreadsheet with their feedback. At the time of writing this thesis, Rishikesh and I are collecting the participants inputs. We will postprocess the data and update the report accordingly. The report will be finalized in the Spring 2024. The updated report will be provided to collaborators and the individual spreadsheets archived with Airborne Wind Europe

(Airborne Wind Europe (2023b)) to preserve anonymity. Airborne Wind Europe acts as an intermediary to host the data collection, storage and dissemination.

The developed report and the code can be used to perform techno-economic analysis, in system design optimization studies, and to evaluate business cases for specific market scenarios. The model will also provide input to technology development roadmaps and inform policymakers, organizations like the IRENA or the IEA, as well as the industry.

This process needs to be repeated periodically, to align the economic report with the development of airborne wind energy. Therefore, Rishikesh and I call for new researchers to help on the development of the future versions of this report.

For an extensive literature review and to look at the first version of the cost model, please see Joshi and Trevisi (2023).

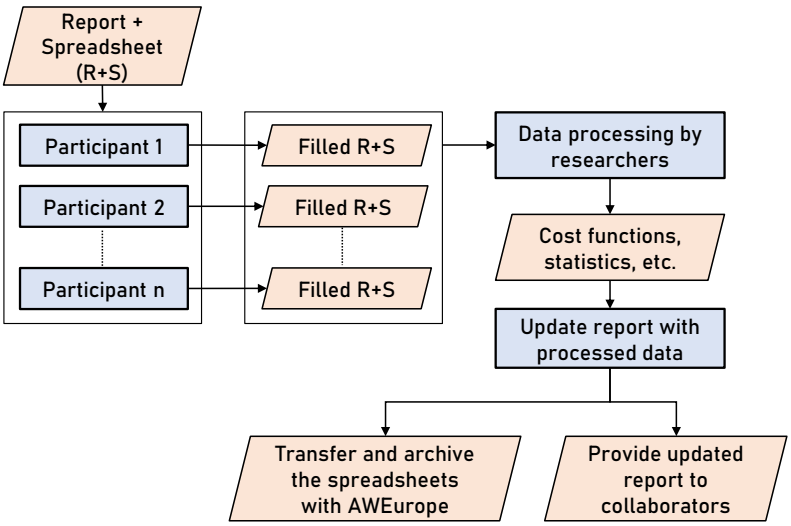

Figure 9.1: *Procedure for the collection of the economic data and update of the economic report.*

CHAPTER 10

Conclusions

In this thesis, the conceptual design problem of windplanes is investigated. The main conclusions are summarized in this chapter.

10.1 Given a wingspan, which design maximizes power?

To study the optimal design problem, the windplane is idealized as a point mass flying circular crosswind trajectories. If gravity is removed from the model, the dynamic problem is axial symmetric and the solution is steady. In this idealized case, the power balance involves only the aerodynamic power and the turbine's thrust power. The power balance can be conveniently expressed in non-dimensional form by normalizing it with the wind power passing through a disk with radius the wingspan. This normalization leads to the definition of the power and the thrust coefficients for windplanes, which is used throughout the thesis. Since the reference area is taken to be a function of just the wingspan, looking for the design which maximizes this power coefficient is equivalent to posing the question "Given a wingspan, which design maximizes power?".

The optimal designs are obtained by operating the wing at the maximum lift-to-drag of the airfoil. Airfoils designed for high lift-to-drag ratio are used for wind turbines and shall also be used for windplanes.

The aspect ratio for windplanes has a similar physical meaning to the solidity for wind turbines. The optimal aspect ratio is finite, as the optimal solidity for wind turbines, and has a low value.

If gravity is included in the model, the gravitational potential energy is being exchanged with the kinetic energy, the aerodynamic energy and the electric energy over one revolution. Since this exchange comes with an associated efficiency, the plane mass and the related trajectory are designed to reduce the potential energy fluctuating

over the loop. Reducing the potential energy means reducing the turning radius and the mass. However, for decreasing turning radii, the available wind power decreases because the windplane sweeps a lower area. For these two conflicting reasons, the optimal mass is finite. Depending on the independent variables, extremely light designs might then be not required.

The windplane makes work on the wind by slowing it down of the induced velocity. It is optimal to have a constant induction over the loop to maximize the raw wind power to be harvested. Therefore, the optimal lift coefficient changes according to the windplane velocity to ensure a constant intensity of the wing circulation, which translates in a constant induction.

10.2 Can windplanes fly stable orbits?

Modeling the flight dynamics of airplanes and the aero-structural dynamics of wind turbines as linear time invariant systems has played a fundamental role in the understanding of the two technologies. The first step on the way to modeling the windplane as a linear time invariant system is to understand about which point to linearize the dynamics. To understand this, the optimal trajectories should be studied first.

To properly model the rigid-body dynamics, a nonlinear aerodynamic model and the nonlinear equations of motion are needed because the exchange of potential energy is a nonlinear process. Analytical aerodynamic derivatives are taken to formulate a linear aerodynamic model about non-linear operating points. The nonlinear equations of motion are solved with a harmonic balance method to look for periodic solutions.

If the gravity is removed from the model, the problem has a steady solution. The windplane is trimmed in the circular crosswind trajectory which maximizes the swept area. The vertical stabilizer pushes outwards, to compensate the yaw moment induced by the centrifugal force.

If the gravity is included in the model, the simplest control strategy is to trim the horizontal stabilizer, the vertical stabilizer and the turbine thrust coefficient to constant values, to actuate the ailerons cyclically and to control the vertical stabilizer in closed loop. The cyclic control of the ailerons rolls the plane and redirects the lift to compensate gravity and to stay airborne. The vertical stabilizer is controlled in closed loop to increase directional stability and damp the precession mode. A moderate reduction in power coefficient between the steady case and the dynamic case with this simple control is found at low wind speed.

The windplane dynamics is then modeled as a linear time invariant system about the trimmed steady solution obtained without gravity. Ten non-null eigenmodes characterizes the dynamics. The roll subsidence, the short period and the dutch-roll are typical modes of airplanes modified by the presence of the tether and the turning maneuver. The Loyd mode is an exponentially stable mode. The pendulum mode is a lightly damped slow oscillating mode. A large wing dihedral angle is beneficial for increasing its damping. The precession mode is a slow oscillating mode which in open-loop has basically no damping. A yaw stability augmentation system is designed to increase the damping of this mode. This stability analysis however does not guarantee stability for nonlinear periodic systems and more rigorous methods should be used in the future. Even if the aerodynamic model has been preliminary validated, the analyses of this second part need to be thoroughly validated.

For a successful diffusion of airborne wind energy systems in the energy sector, modeling the economics in a realistic way is a crucial step. The development of a reference economic model has been initiated with the collaboration of the companies operating in the airborne wind energy field and will be finalized in the near future. However, this effort needs to be repeated periodically with the technology developing further.

CHAPTER 11

Nomenclature

11.1 Main latin symbols

a Aerodynamic induction
a_f Aerodynamic induction due to the far wake
a_n Aerodynamic induction due to the near wake
a_t Onboard turbines aerodynamic induction
A Wing area
AR Wing aspect ratio
b Wing span
C_a Aerodynamic power coefficient
C_d Wing profile drag coefficient
$C_{d,0}$ Parameter describing the wing profile drag coefficient at zero lift
$C_{d,te}$ Tether section drag coefficient
C_D Windplane drag coefficient including the near wake induced drag coefficient
C_{Di}^n Induced drag coefficient due to the near wake
$C_{D,p}$ Parasite drag coefficient
$C_{D,te}$ Equivalent tether drag coefficient
C_g Gravitational power coefficient
C_L Lift coefficient
C_P Power coefficient
C_T Thrust coefficient
C_τ Aerodynamic dissipative power coefficient
D Drag force
D_{te} Tether diameter
d_{te} $D_{te}/(b/2)$ Nondimensional tether diameter
e Oswald factor

E_k Kinetic energy
e_k Nondimensional kinetic energy
$\mathcal{F}_B$ Body coordinate system
$\mathcal{F}_G$ Ground coordinate system
$\mathcal{F}_R$ Rotating coordinate system
$\mathcal{F}_S$ Stability coordinate system
$\mathcal{F}_{Te}$ Tether coordinate system
k_d Parameter of the quadratic wing profile drag coefficient part
L Lift force
L_{te} Tether length
l_{te} $L_{te}/(b/2)$ Nondimensional tether length
m Windplane mass
P Electric generated power
R_0 Trajectory radius (In Chap. 6 it is the instantaneous turning radius)
T_t Turbines thrust force
u_0 Longitudinal reference velocity
v_a Apparent wind speed
v_w Wind speed

11.2 Main greek symbols

ξ_t $R_t/(b/2)$ Nondimensional onboard wind turbine radius
Γ Dihedral angle of the main wing, or bound circulation in Chapt. 3
μ $m/(\rho b^3)$ Nondimensional mass
Λ Sweep angle
λ u/v_r: wing speed ratio
Φ Opening angle of the cone swept by the tether during one loop
Ψ Azimuth angle
κ_0 $b/(2R_0)$: inverse turning ratio
ρ Air density
$\mathcal{T}$ Main period

Bibliography

Ahrens, U., Diehl, M., and Schmehl, R.: Airborne Wind Energy, Green Energy and Technology, Springer Berlin, Heidelberg, https://doi.org/10.1007/978-3-642-39965-7, 2013.

Airborne Wind Europe: IEA Wind Task 48, https://iea-wind.org/task48/, (accessed on December 1, 2023), 2023a.

Airborne Wind Europe: The association of the Airborne Wind Energy Sector, https://airbornewindeurope.org/, (accessed on December 1, 2023), 2023b.

Anderson, J.: Fundamentals of Aerodynamics, McGraw-Hill Education, sixth edn., http://lccn.loc.gov/2015040997, 2017.

Andersson, J. A. E., Gillis, J., Horn, G., Rawlings, J. B., and Diehl, M.: CasADi – A software framework for nonlinear optimization and optimal control, Mathematical Programming Computation, 11, 1–36, doi: 10.1007/s12532-018-0139-4, 2019.

Archer, C. L.: An Introduction to Meteorology for Airborne Wind Energy, in: Airborne Wind Energy, edited by Ahrens, U., Diehl, M., and Schmehl, R., pp. 81–94, Springer Berlin Heidelberg, doi: 10.1007/978-3-642-39965-7_5, 2013.

Argatov, I. and Silvennoinen, R.: Efficiency of Traction Power Conversion Based on Crosswind Motion, in: Airborne Wind Energy, edited by Ahrens, U., Diehl, M., and Schmehl, R., pp. 65–79, Springer Berlin Heidelberg, Berlin, Heidelberg, doi: 10.1007/978-3-642-39965-7_4, 2013.

Argatov, I., Rautakorpi, P., and Silvennoinen, R.: Estimation of the mechanical energy output of the kite wind generator, Renewable Energy, 34, 1525–1532, doi: 10.1016/j.renene.2008.11.001, 2009.

Bauer, F., Kennel, R. M., Hackl, C. M., Campagnolo, F., Patt, M., and Schmehl, R.: Drag power kite with very high lift coefficient, Renewable Energy, 118, 290–305, doi: 10.1016/j.renene.2017.10.073, 2018.

Bosman, R., Reid, V., Vlasblom, M., and Smeets, P.: Airborne Wind Energy Tethers with High-Modulus Polyethylene Fibers, pp. 563–585, Springer Berlin Heidelberg, Berlin, Heidelberg, doi: 10.1007/978-3-642-39965-7_33, 2013.

Branlard, E., Brownstein, I., Strom, B., Jonkman, J., Dana, S., and Baring-Gould, E. I.: A multipurpose lifting-line flow solver for arbitrary wind energy concepts, Wind Energy Science, 7, 455–467, doi: 10.5194/wes-7-455-2022, 2022.

Candade, A. A., Ranneberg, M., and Schmehl, R.: Structural analysis and optimization of a tethered swept wing for airborne wind energy generation, Wind Energy, 23, 1006–1025, doi: 10.1002/we.2469, 2020.

Cobb, M. K., Barton, K., Fathy, H., and Vermillion, C.: Iterative Learning-Based Path Optimization for Repetitive Path Planning, With Application to 3-D Crosswind Flight of Airborne Wind Energy Systems, IEEE Transactions on Control Systems Technology, 28, 1447–1459, doi: 10.1109/TCST.2019.2912345, 2020.

Costello, S., Costello, C., François, G., and Bonvin, D.: Analysis of the maximum efficiency of kite-power systems, Journal of renewable and sustainable energy, 7, 053 108, doi: 10.1063/1.4931111, 2015.

De Fezza, G. and Barber, S.: Parameter analysis of a multi-element airfoil for application to airborne wind energy, Wind Energy Science, 7, 1627–1640, doi: 10.5194/wes-7-1627-2022, 2022.

De Lellis, M., Reginatto, R., Saraiva, R., and Trofino, A.: The Betz limit applied to Airborne Wind Energy, Renewable Energy, 127, 32–40, doi: 10.1016/j.renene.2018.04.034, 2018.

De Schutter, J., Leuthold, R., Bronnenmeyer, T., Paelinck, R., and Diehl, M.: Optimal control of stacked multi-kite systems for utility-scale airborne wind energy, in: 2019 IEEE 58th Conference on Decision and Control (CDC), pp. 4865–4870, doi: 10.1109/CDC40024.2019.9030026, 2019.

De Schutter, J., Leuthold, R., Bronnenmeyer, T., Malz, E., Gros, S., and Diehl, M.: AWEbox: An Optimal Control Framework for Single- and Multi-Aircraft Airborne Wind Energy Systems, Energies, 16, doi: 10.3390/en16041900, 2023.

Diehl, M.: Airborne Wind Energy: Basic Concepts and Physical Foundations, in: Airborne Wind Energy, edited by Ahrens, U., Diehl, M., and Schmehl, R., pp. 3–22, Springer Berlin Heidelberg, Berlin, Heidelberg, doi: 10.1007/978-3-642-39965-7_1, 2013.

Dimitriadis, G.: Time Integration, in: Introduction to Nonlinear Aeroelasticity, chap. 3, pp. 63–111, John Wiley & Sons, Ltd, doi: 10.1002/9781118756478.ch3, 2017.

Eijkelhof, D. and Schmehl, R.: Six-Degrees-Of-Freedom Simulation Model for Future Multi-Megawatt Airborne Wind Energy Systems, SSRN Electronic Journal, doi: 10.2139/ssrn.4003237, 2022.

Fagiano, L., Zgraggen, A. U., Morari, M., and Khammash, M.: Automatic Crosswind Flight of Tethered Wings for Airborne Wind Energy: Modeling, Control Design,

and Experimental Results, IEEE Transactions on Control Systems Technology, 22, 1433–1447, doi: 10.1109/TCST.2013.2279592, 2014.

Fagiano, L. M.: Control of Tethered Airfoils for High Altitude Wind Energy Generation, Ph.D. thesis, Politecnico di Torino, `https://hdl.handle.net/11311/1006424`, 2009.

Fasel, U., Keidel, D., Molinari, G., and Ermanni, P.: Aerostructural optimization of a morphing wing for airborne wind energy applications, Smart Materials and Structures, 26, 095 043, doi: 10.1088/1361-665X/aa7c87, 2017.

Fechner, U. and Schmehl, R.: Flight path control of kite power systems in a turbulent wind environment, in: 2016 American Control Conference (ACC), pp. 4083–4088, doi: 10.1109/ACC.2016.7525563, 2016.

Fechner, U., van der Vlugt, R., Schreuder, E., and Schmehl, R.: Dynamic model of a pumping kite power system, Renewable Energy, 83, 705–716, doi: 10.1016/j.renene.2015.04.028, 2015.

Fernandes, M. C. R. M., Paiva, L. T., and Fontes, F. A. C. C.: Optimal Path and Path-Following Control in Airborne Wind Energy Systems, in: Advances in Evolutionary and Deterministic Methods for Design, Optimization and Control in Engineering and Sciences, edited by Gaspar-Cunha, A., Periaux, J., Giannakoglou, K. C., Gauger, N. R., Quagliarella, D., and Greiner, D., pp. 409–421, Springer International Publishing, Cham, doi: 10.1007/978-3-030-57422-2_26, 2021.

Gaunaa, M., Forsting, A. M., and Trevisi, F.: An engineering model for the induction of crosswind kite power systems, Journal of Physics: Conference Series, 1618, 032 010, doi: 10.1088/1742-6596/1618/3/032010, 2020.

Gros, S. and Diehl, M.: Modeling of Airborne Wind Energy Systems in Natural Coordinates, in: Airborne Wind Energy, edited by Ahrens, U., Diehl, M., and Schmehl, R., pp. 181–203, Green Energy and Technology. Springer, Singapore, doi: 10.1007/978-3-642-39965-7_10, 2013.

Gros, S., Zanon, M., and Diehl, M.: A relaxation strategy for the optimization of Airborne Wind Energy systems, in: 2013 European Control Conference (ECC), pp. 1011–1016, doi: 10.23919/ECC.2013.6669670, 2013.

Haas, T. and Meyers, J.: Comparison study between wind turbine and power kite wakes, Journal of Physics: Conference Series, 854, 012 019, doi: 10.1088/1742-6596/854/1/012019, 2017.

Haas, T., De Schutter, J., Diehl, M., and Meyers, J.: Wake characteristics of pumping mode airborne wind energy systems, in: Journal of Physics: Conference Series, vol. 1256, p. 012016, IOP Publishing, doi: 10.1088/1742-6596/1256/1/012016, 2019a.

Haas, T., Schutter, J. D., Diehl, M., and Meyers, J.: Wake characteristics of pumping mode airborne wind energy systems, Journal of Physics: Conference Series, 1256, 012 016, doi: 10.1088/1742-6596/1256/1/012016, 2019b.

Hackl, C. M. and Schmehl, R.: Airborne Wind Energy Systems. Special issue of Energies (ISSN 1996-1073), MDPI, 2023.

Homsy, G.: Oktoberkite and the MX2., in: The Energy Kite Part I., edited by Echeverri, P., Fricke, T., Homsy, G., and Tucker, N., pp. 7–89, 2020.

Horn, G., Gros, S., and Diehl, M.: Numerical trajectory optimization for airborne wind energy systems described by high fidelity aircraft models, in: Airborne Wind Energy, edited by Ahrens, U., Diehl, M., and Schmehl, R., pp. 205–218, Springer, doi: 10.1007/978-3-642-39965-7_11, 2013.

Houska, B. and Diehl, M.: Optimal Control of Towing Kites, in: Proceedings of the 45th IEEE Conference on Decision and Control, pp. 2693–2697, doi: 10.1109/CDC.2006.377210, 2006.

Houska, B. and Diehl, M.: Robustness and stability optimization of power generating kite systems in a periodic pumping mode, in: 2010 IEEE International Conference on Control Applications, pp. 2172–2177, doi: 10.1109/CCA.2010.5611288, 2010.

IEA: Net Zero by 2050, `https://www.iea.org/reports/net-zero-by-2050`, 2021.

IRENA and GRA: Tripling renewable power and doubling energy efficiency by 2030: Crucial steps towards 1.5C, International Renewable Energy Agency, 2023.

Jonkman, J., Hayman, G., Mudafort, R., Damiani, R., Wendt, F., Google Incorporated, and USDOE: KiteFAST, `https://www.osti.gov//servlets/purl/1786962`, 2018.

Joshi, R. and Trevisi, F.: Reference economic model for airborne wind energy systems, doi: 10.5281/zenodo.8114628, 2023.

Kheiri, M., Bourgault, F., Saberi Nasrabad, V., and Victor, S.: On the aerodynamic performance of crosswind kite power systems, Journal of Wind Engineering and Industrial Aerodynamics, 181, 1–13, doi: 10.1016/j.jweia.2018.08.006, 2018.

Kheiri, M., Saberi Nasrabad, V., and Bourgault, F.: A new perspective on the aerodynamic performance and power limit of crosswind kite systems, Journal of Wind Engineering and Industrial Aerodynamics, 190, 190–199, doi: 10.1016/j.jweia.2019.04.010, 2019.

Lambe, A. B. and Martins, J. R. R. A.: Extensions to the Design Structure Matrix for the Description of Multidisciplinary Design, Analysis, and Optimization Processes, Structural and Multidisciplinary Optimization, 46, 273–284, doi: 10.1007/s00158-012-0763-y, 2012.

Leuthold, R., De Schutter, J., Malz, E. C., Licitra, G., Gros, S., and Diehl, M.: Operational Regions of a Multi-Kite AWE System, in: 2018 European Control Conference (ECC), pp. 52–57, doi: 10.23919/ECC.2018.8550199, 2018.

Leuthold, R., Crawford, C., Gros, S., and Diehl, M.: Engineering Wake Induction Model For Axisymmetric Multi-Kite Systems, Journal of Physics: Conference Series, doi: https://doi.org/10.1088/1742-6596/1256/1/012009, 2019.

Licitra, G., Koenemann, J., Burger, A., Williams, P., Ruiterkamp, R., and Diehl, M.: Performance assessment of a rigid wing Airborne Wind Energy pumping system, Energy, 173, 569–585, doi: 10.1016/j.energy.2019.02.064, 2019.

Loyd, M.: Crossswind Kite Power, Journal of Energy, 4, 106–111, 1980.

Luchsinger, R. H.: Pumping Cycle Kite Power, in: Airborne Wind Energy, edited by Ahrens, U., Diehl, M., and Schmehl, R., pp. 47–64, doi: 10.1007/978-3-642-39965-7_3, 2013.

Malz, E., Koenemann, J., Sieberling, S., and Gros, S.: A reference model for airborne wind energy systems for optimization and control, Renewable Energy, 140, 1004–1011, doi: 10.1016/j.renene.2019.03.111, 2019.

Malz, E., Hedenus, F., Goransson, L., Verendel, V., and Gros, S.: Drag-mode airborne wind energy vs. wind turbines: An analysis of power production, variability and geography, Energy, 193, 116 765, doi: 10.1016/j.energy.2019.116765, 2020a.

Malz, E., Verendel, V., and Gros, S.: Computing the power profiles for an Airborne Wind Energy system based on large-scale wind data, Renewable Energy, 162, 766–778, doi: 10.1016/j.renene.2020.06.056, 2020b.

Marelli, S. and Sudret, B.: UQLAB: a framework for Uncertainty Quantification in MATLAB, The 2nd International Conference on Vulnerability and Risk Analysis and Management (ICVRAM 2014), pp. 2554–2563, doi: 10.1061/9780784413609.257, 2014.

Marten, D., Lennie, M., Pechlivanoglou, G., Nayeri, C. N., and Paschereit, C. O.: Implementation, Optimization and Validation of a Nonlinear Lifting Line Free Vortex Wake Module Within the Wind Turbine Simulation Code QBlade, Volume 9: Oil and Gas Applications; Supercritical CO2 Power Cycles; Wind Energy, doi: 10.1115/GT2015-43265, 2015.

Martins, J. R. R. A. and Lambe, A. B.: Multidisciplinary Design Optimization: A Survey of Architectures, AIAA Journal, 51, 2049–2075, doi: 10.2514/1.J051895, 2013.

Mehr, J. A., Alvarez, E. J., and Ning, A.: Unsteady Aerodynamic Analysis of Wind Harvesting Aircraft, in: AIAA AVIATION 2020 FORUM, doi: 10.2514/6.2020-2761, 2020.

Naik, K. and Vermillion, C.: Integrated physical design, control design, and site selection for an underwater energy-harvesting kite system, Renewable Energy, 220, 119 687, doi: https://doi.org/10.1016/j.renene.2023.119687, 2024.

Naik, K., Beknalkar, S., Mazzoleni, A., and Vermillion, C.: Fused Geometric, Structural, and Control Co-Design Framework for an Energy-Harvesting Ocean Kite, in: 2021 American Control Conference (ACC), pp. 3525–3531, doi: 10.23919/ACC50511.2021.9483434, 2021.

Naik, K., Beknalkar, S., Reed, J., Mazzoleni, A., Fathy, H., and Vermillion, C.: Pareto Optimal and Dual-Objective Geometric and Structural Design of an Underwater Kite

for Closed-Loop Flight Performance, Journal of Dynamic Systems, Measurement, and Control, 145, 011 005, doi: 10.1115/1.4055978, 2022.

Nelson, R.: Flight Stability and Automatic Control, Aerospace Science & Technology, WCB/McGraw Hill, https://books.google.it/books?id=Uzs8PgAACAAJ, 1998.

Pasquinelli, G.: An Engineering Model for Power Generation Estimation of Crosswind Airborne Wind Energy Systems, Master's thesis, Politecnico di Milano, https://hdl.handle.net/10589/183848, 2021.

Pastor-Rodríguez, A., Sánchez-Arriaga, G., and Sanjurjo-Rivo, M.: Modeling and Stability Analysis of Tethered Kites at High Altitudes, Journal of Guidance, Control, and Dynamics, 40, 1892–1901, doi: 10.2514/1.G002550, 2017.

Phillips, W. F., Anderson, E. A., Jenkins, J. C., and Sunouchi, S.: Estimating the Low-Speed Downwash Angle on an Aft Tail, Journal of Aircraft, 39, 600–608, doi: 10.2514/2.2998, 2002.

Porta Ko, A., Smidt, S., Schmehl, R., and Mandru, M.: Optimisation of a Multi-Element Airfoil for a Fixed-Wing Airborne Wind Energy System, Energies, 16, doi: 10.3390/en16083521, 2023.

Rangriz, S. and Kheiri, M.: Design of optimal airfoils for airborne wind energy applications, doi: 10.2514/6.2023-1155, 2023.

Rapp, S., Schmehl, R., Oland, E., and Haas, T.: Cascaded Pumping Cycle Control for Rigid Wing Airborne Wind Energy Systems, Journal of Guidance, Control, and Dynamics, 42, 2456–2473, doi: 10.2514/1.G004246, 2019.

Saleem, A. and Kim, M.-H.: Aerodynamic performance optimization of an airfoil-based airborne wind turbine using genetic algorithm, Energy, 203, 117 841, doi: 10.1016/j.energy.2020.117841, 2020.

Salord Losantos, L. and Sánchez-Arriaga, G.: Flight Dynamics and Stability of Kites in Steady and Unsteady Wind Conditions, Journal of Aircraft, 52, 660–666, doi: 10.2514/1.C032825, 2015.

Sánchez-Arriaga, G. and Serrano-Iglesias, J.: Modeling and Natural Mode Analysis of Tethered Multi-Aircraft Systems, Journal of Guidance, Control, and Dynamics, 44, 1199–1210, doi: 10.2514/1.G005075, 2021.

Sánchez-Arriaga, G., García-Villalba, M., and Schmehl, R.: Modeling and dynamics of a two-line kite, Applied Mathematical Modelling, 47, 473–486, doi: 10.1016/j.apm.2017.03.030, 2017.

Sánchez-Arriaga, G., Pastor-Rodríguez, A., Sanjurjo-Rivo, M., and Schmehl, R.: A lagrangian flight simulator for airborne wind energy systems, Applied Mathematical Modelling, 69, 665–684, doi: 10.1016/j.apm.2018.12.016, 2019.

Schelbergen, M. and Schmehl, R.: Validation of the quasi-steady performance model for pumping airborne wind energy systems., Journal of Physics: Conference Series, 1618, doi: 10.1088/1742-6596/1618/3/032003, 2020.

Schmehl, R.: Airborne Wind Energy, Green Energy and Technology, Springer Singapore, https://doi.org/10.1007/978-981-10-1947-0, 2018.

Schmehl, R., Noom, M., and van der Vlugt, R.: Traction Power Generation with Tethered Wings, in: Airborne Wind Energy, edited by Ahrens, U., Diehl, M., and Schmehl, R., pp. 23–45, Springer Berlin Heidelberg, Berlin, Heidelberg, doi: 10.1007/978-3-642-39965-7_2, 2013.

Sicard, J., Homsy, G., and Abraham, M.: Kite Stability in Crosswind Flight., in: The Energy Kite Part II., edited by Echeverri, P., Fricke, T., Homsy, G., and Tucker, N., pp. 223–232, 2020.

Sternberg, J., Goit, J., Gros, S., Meyers, J., and Diehl, M.: Robust and Stable Periodic Flight of Power Generating Kite Systems in a Turbulent Wind Flow Field, IFAC Proceedings Volumes, 45, 140–145, doi: 10.3182/20120913-4-IT-4027.00009, 15th IFAC Workshop on Control Applications of Optimization, 2012.

Stuyts, J., Horn, G., Vandermeulen, W., Driesen, J., and Diehl, M.: Effect of the Electrical Energy Conversion on Optimal Cycles for Pumping Airborne Wind Energy, IEEE Transactions on Sustainable Energy, 6, 2–10, doi: 10.1109/TSTE.2014.2349071, 2015.

Terink, E. J., Breukels, J., Schmehl, R., and Ockels, W. J.: Flight Dynamics and Stability of a Tethered Inflatable Kiteplane, Journal of Aircraft, 48, 503–513, doi: 10.2514/1.C031108, 2011.

Thedens, P., de Oliveira, G., and Schmehl, R.: Ram-air kite airfoil and reinforcements optimization for airborne wind energy applications, Wind Energy, 22, 653–665, doi: 10.1002/we.2313, 2019.

Todeschini, D., Fagiano, L., Micheli, C., and Cattano, A.: Control of a rigid wing pumping Airborne Wind Energy system in all operational phases, Control Engineering Practice, 111, 104 794, doi: 10.1016/j.conengprac.2021.104794, 2021.

Trevisi, F. and Croce, A.: A simplified approach to the Fly-Gen AWES design, Abstract submitted to TORQUE 2024 Conference, 2024.

Trevisi, F., Gaunaa, M., and Mcwilliam, M.: The Influence of Tether Sag on Airborne Wind Energy Generation., Journal of Physics: Conference Series, 1618, doi: 10.1088/1742-6596/1618/3/032006, 2020a.

Trevisi, F., Gaunaa, M., and Mcwilliam, M.: Unified engineering models for the performance and cost of Ground-Gen and Fly-Gen crosswind Airborne Wind Energy Systems, Renewable Energy, 162, 893–907, doi: 10.1016/j.renene.2020.07.129, 2020b.

Trevisi, F., Croce, A., and Riboldi, C. E. D.: Flight Stability of Rigid Wing Airborne Wind Energy Systems, Energies, 14, doi: 10.3390/en14227704, 2021a.

Trevisi, F., McWilliam, M., and Gaunaa, M.: Configuration optimization and global sensitivity analysis of Ground-Gen and Fly-Gen Airborne Wind Energy Systems, Renewable Energy, 178, 385–402, doi: 10.1016/j.renene.2021.06.011, 2021b.

Trevisi, F., Castro-Fernández, I., Pasquinelli, G., Riboldi, C. E. D., and Croce, A.: Flight trajectory optimization of Fly-Gen airborne wind energy systems through a harmonic balance method, Wind Energy Science, 7, 2039–2058, doi: 10.5194/wes-7-2039-2022, 2022a.

Trevisi, F., Riboldi, C. E. D., and Croce, A.: Sensitivity analysis of a Ground-Gen Airborne Wind Energy System design., Journal of Physics: Conference Series, 2265, 042 067, doi: 10.1088/1742-6596/2265/4/042067, 2022b.

Trevisi, F., Riboldi, C. E. D., and Croce, A.: Vortex model of the aerodynamic wake of airborne wind energy systems, Wind Energy Science, 8, 999–1016, doi: 10.5194/wes-8-999-2023, 2023a.

Trevisi, F., Riboldi, C. E. D., and Croce, A.: Refining the airborne wind energy systems power equations with a vortex wake model, Wind Energy Science, 8, 1639–1650, doi: 10.5194/wes-8-1639-2023, 2023b.

Tucker, N.: Airborne Wind Turbine Performance: Key Lessons From More Than a Decade of Flying Kites., in: The Energy Kite Part I., edited by Echeverri, P., Fricke, T., Homsy, G., and Tucker, N., pp. 93–224, Makani Technologies LLC, `https://x.company/projects/makani/#`, 2020.

van der Vlugt, R., Bley, A., Noom, M., and Schmehl, R.: Quasi-steady model of a pumping kite power system, Renewable Energy, 131, 83–99, doi: 10.1016/j.renene.2018.07.023, 2019.

Vander Lind, D.: Analysis and Flight Test Validation of High Performance AirborneWind Turbines, pp. 473–490, Springer Berlin Heidelberg, Berlin, Heidelberg, doi: 10.1007/978-3-642-39965-7_28, 2013.

Veers, P., Dykes, K., Basu, S., Bianchini, A., Clifton, A., Green, P., Holttinen, H., Kitzing, L., Kosovic, B., Lundquist, J. K., Meyers, J., O'Malley, M., Shaw, W. J., and Straw, B.: Grand Challenges: wind energy research needs for a global energy transition, Wind Energy Science, 7, 2491–2496, doi: 10.5194/wes-7-2491-2022, 2022.

Vermillion, C., Cobb, M., Fagiano, L., Leuthold, R., Diehl, M., Smith, R. S., Wood, T. A., Rapp, S., Schmehl, R., Olinger, D., and Demetriou, M.: Electricity in the air: Insights from two decades of advanced control research and experimental flight testing of airborne wind energy systems, Annual Reviews in Control, 52, 330–357, doi: 10.1016/j.arcontrol.2021.03.002, 2021.

Vimalakanthan, K., Caboni, M., Schepers, J., Pechenik, E., and Williams, P.: Aerodynamic analysis of Ampyx's airborne wind energy system, Journal of Physics: Conference Series, 1037, 062 008, doi: 10.1088/1742-6596/1037/6/062008, 2018.

APPENDIX $\mathcal{A}$

Rotational matrices notation

The rotational matrix, expressed in $\mathcal{F}_A$, which rotates from $\mathcal{F}_A$ to $\mathcal{F}_B$ is denoted with $\mathbf{R}^A_{A\to B} = \mathbf{R}^A_{AB}$. Note that $\mathbf{R}^A_{AB} = \mathbf{R}^B_{AB}$. The rotational matrix $\mathbf{R}^A_{AB}$ can be used to rotate a vector a^A, expressed in $\mathcal{F}_A$ into a vector b^A, expressed in the same coordinate system

$$\mathbf{b}^A = \mathbf{R}^A_{AB}\mathbf{a}^A. \tag{A.1}$$

Since this operation is a rotation: $\mathbf{b}^B = \mathbf{a}^A$. It follows that

$$\mathbf{b}^A = \mathbf{R}^A_{AB}\mathbf{b}^B, \tag{A.2}$$

and

$$\mathbf{b}^B = \mathbf{R}^{AT}_{AB}\mathbf{b}^A = \mathbf{R}^A_{BA}\mathbf{b}^A. \tag{A.3}$$

To change the basis of a rotation tensor $\mathbf{T}$, rotational matrices are to be applied

$$\mathbf{T}^A = \mathbf{R}^A_{AB}\mathbf{T}^B\mathbf{R}^{AT}_{AB}. \tag{A.4}$$

To compose rotations, rotational matrices expressed in the same basis need to be applied in a sequential order

$$\mathbf{R}^A_{A\to C} = \mathbf{R}^A_{B\to C}\mathbf{R}^A_{A\to B}. \tag{A.5}$$

To express rotations as a composition of planar rotations, the basis of the rotation matrix need to be expressed in the basis where the rotation happens. The rotation matrix $\mathbf{R}^A_{A\to C}$ can be therefore be written as

$$\mathbf{R}^A_{A\to C} = \mathbf{R}^A_{B\to C}\mathbf{R}^A_{A\to B} = (\mathbf{R}^A_{A\to B}\mathbf{R}^B_{B\to C}\mathbf{R}^{AT}_{A\to B})\mathbf{R}^A_{A\to B} = \mathbf{R}^A_{A\to B}\mathbf{R}^B_{B\to C}. \tag{A.6}$$

The following planar rotational matrices are defined

$$\begin{aligned}
\mathbf{R}_x(\alpha) &= \begin{bmatrix} 1 & 0 & 0 \\ 0 & \cos\alpha & -\sin\alpha \\ 0 & \sin\alpha & \cos\alpha \end{bmatrix}, \quad \mathbf{R}_y(\alpha) = \begin{bmatrix} \cos\alpha & 0 & \sin\alpha \\ 0 & 1 & 0 \\ -\sin\alpha & 0 & \cos\alpha \end{bmatrix}, \\
\mathbf{R}_z(\alpha) &= \begin{bmatrix} \cos\alpha & -\sin\alpha & 0 \\ \sin\alpha & \cos\alpha & 0 \\ 0 & 0 & 1 \end{bmatrix}.
\end{aligned} \tag{A.7}$$

APPENDIX B

Aerodynamics of the main wing

B.1 Arm matrices derivations

The following integrals are defined to have the dimensions of areas

$$
\begin{aligned}
I_\eta &= \frac{I_y}{R_0} = \frac{1}{R_0}\int_{-b/2}^{b/2} c(y) y \frac{y}{|y|} dy = \frac{2}{R_0}\int_0^{b/2} c(y) y dy = \frac{2}{3\pi} A \frac{b}{R_0}, \\
I_{\eta\eta} &= \frac{I_{yy}}{R_0^2} = \frac{1}{R_0^2}\int_{-b/2}^{b/2} c(y) y^2 dy = \frac{1}{16} A \frac{b^2}{R_0^2}, \\
I_{\eta\eta\eta} &= \frac{I_{yyy}}{R_0^3} = \frac{1}{R_0^3}\int_{-b/2}^{b/2} c(y) y^3 \frac{y}{|y|} dy = \frac{2}{R_0^3}\int_0^{b/2} c(y) y^3 dy = \frac{1}{15\pi} A \frac{b^3}{R_0^3}.
\end{aligned}
\tag{B.1}
$$

The aerodynamic forces are applied at $1/4$ chord, but the velocity is evaluated at $3/4$ chord (collocation points), to be consistent with vortex lattice methods. So that the following integrals are also derived

$$
\begin{aligned}
I_{c2} &= \int_{-b/2}^{b/2} c(y)^2 dy = \frac{32}{3}\frac{A^2}{\pi^2}\frac{1}{b}, \\
I_{\eta c2} &= \frac{1}{R_0}\int_{-b/2}^{b/2} c(y)^2 y \frac{y}{|y|} dy = 2\frac{A^2}{\pi^2}\frac{1}{R_0}, \\
I_{\eta\eta c2} &= \frac{1}{R_0^2}\int_{-b/2}^{b/2} c(y)^2 y^2 dy = \frac{8}{15}\frac{A^2}{\pi^2}\frac{b}{R_0^2}.
\end{aligned}
\tag{B.2}
$$

B.1.1 Even arm matrices

The even arm matrix $\mathbf{P}$ is defined as function of $\mathbf{P}_1$ and $\mathbf{P}_2$

$$\mathbf{P} = \mathbf{S}^{-1}\left(\begin{bmatrix} \mathbf{1} \\ [tw_x, 0, tw_z]^\times \end{bmatrix} + \eta\frac{\eta}{|\eta|}\begin{bmatrix} \mathbf{0} \\ (\boldsymbol{ds}^\times[0, R_0, 0]^T)^\times \end{bmatrix}\right) = \mathbf{P}_1 + \eta\frac{\eta}{|\eta|}\mathbf{P}_2. \tag{B.3}$$

The even arm integral matrices are derived as follows

$$\mathbf{P}_A = \frac{1}{A}\int_{-b/2}^{b/2} c(y)\mathbf{P}dy = \frac{1}{A}\int_{-b/2}^{b/2} c(y)\left(\mathbf{P}_1 + \eta\frac{\eta}{|\eta|}\mathbf{P}_2\right)dy = \mathbf{P}_1 + \frac{I_\eta}{A}\mathbf{P}_2, \tag{B.4}$$

$$\mathbf{P}_{c2} = \frac{1}{A}\int_{-b/2}^{b/2} c(y)^2\mathbf{P}dy = \frac{1}{A}\int_{-b/2}^{b/2} c(y)^2\left(\mathbf{P}_1 + \eta\frac{\eta}{|\eta|}\mathbf{P}_2\right)dy = \frac{I_{c2}}{A}\mathbf{P}_1 + \frac{I_{\eta c2}}{A}\mathbf{P}_2, \tag{B.5}$$

$$\mathbf{P}_\eta = \frac{1}{A}\int_{-b/2}^{b/2} c(y)\frac{\eta^2}{|\eta|}\mathbf{P}dy = \frac{I_\eta}{A}\mathbf{P}_1 + \frac{I_{\eta\eta}}{A}\mathbf{P}_2, \tag{B.6}$$

$$\mathbf{P}_{\eta c2} = \frac{1}{A}\int_{-b/2}^{b/2} c(y)\frac{\eta^2}{|\eta|}\mathbf{P}dy = \frac{I_{\eta c2}}{A}\mathbf{P}_1 + \frac{I_{\eta\eta c2}}{A}\mathbf{P}_2, \tag{B.7}$$

$$\mathbf{P}_{\eta\eta} = \frac{1}{A}\int_{-b/2}^{b/2} c(y)\eta^2\mathbf{P}dy = \frac{I_{\eta\eta}}{A}\mathbf{P}_1 + \frac{I_{\eta\eta\eta}}{A}\mathbf{P}_2. \tag{B.8}$$

Considering x and z as the collocation points position at $3/4$ chord ($\boldsymbol{tw}^S(y) - c(y)/2$, where $\boldsymbol{tw}^S$ is given in Eq. (6.20)), the even arm matrices needed for the estimation of the derivatives with respect to angular rates are

$$\begin{aligned}\mathbf{P}_{A,x} &= \frac{1}{A}\int_{-b/2}^{b/2} c(y)\mathbf{P}x\ dy = \frac{1}{A}\int_{-b/2}^{b/2} c(y)\mathbf{P}\left(tw_x - \frac{y}{R_0}R_0\frac{\eta}{|\eta|}\Lambda - \frac{c(y)}{2}\right)dy \\ &= tw_x\mathbf{P}_A - R_0\Lambda\mathbf{P}_\eta - \frac{\mathbf{P}_{c2}}{2},\end{aligned} \tag{B.9}$$

and

$$\begin{aligned}\mathbf{P}_{A,z} &= \frac{1}{A}\int_{-b/2}^{b/2} c(y)\mathbf{P}z\ dy = \frac{1}{A}\int_{-b/2}^{b/2} c(y)\mathbf{P}\left(tw_z + \frac{y}{R_0}R_0\frac{\eta}{|\eta|}\Gamma\right)dy \\ &= tw_z\mathbf{P}_A + R_0\Gamma\mathbf{P}_\eta.\end{aligned} \tag{B.10}$$

Similarly, $\mathbf{P}_{\eta,x}$ is

$$\begin{aligned}\mathbf{P}_{\eta,x} &= \frac{1}{A}\int_{-b/2}^{b/2} c(y)\frac{\eta}{|\eta|}\eta\mathbf{P}xdy = \frac{1}{A}\int_{-b/2}^{b/2} c(y)\mathbf{P}\frac{\eta}{|\eta|}\eta\left(tw_x - \frac{y}{R_0}R_0\frac{\eta}{|\eta|}\Gamma - \frac{c(y)}{2}\right)dy \\ &= tw_x\mathbf{P}_\eta - R_0\Lambda\mathbf{P}_{\eta\eta} - \frac{\mathbf{P}_{\eta c2}}{2},\end{aligned} \tag{B.11}$$

and $\mathbf{P}_{\eta,z}$

$$\begin{aligned}\mathbf{P}_{\eta,z} &= \frac{1}{A}\int_{-b/2}^{b/2} c(y)\frac{\eta}{|\eta|}\eta\mathbf{P}\ z\ dy = \frac{1}{A}\int_{-b/2}^{b/2} c(y)\mathbf{P}\frac{\eta}{|\eta|}\eta\left(tw_z + \frac{y}{R_0}R_0\frac{\eta}{|\eta|}\Gamma\right)dy \\ &= tw_z\mathbf{P}_\eta + R_0\Gamma\mathbf{P}_{\eta\eta}.\end{aligned} \tag{B.12}$$

B.1.2 Odd arm matrices

The odd arm matrix $\mathbf{D}$ is defined as function of $\mathbf{D_1}$ and $\mathbf{D_2}$

$$\mathbf{D} = \mathbf{S}^{-1}\begin{bmatrix}\mathbf{0}\\ [0,R_0,0]^\times\end{bmatrix} + \frac{1}{|\eta|}\mathbf{S}^{-1}\begin{bmatrix}\boldsymbol{ds}^\times\\ [tw_x,0,tw_z]^\times\boldsymbol{ds}^\times\end{bmatrix} = \mathbf{D}_1 + \frac{1}{|\eta|}\mathbf{D}_2. \tag{B.13}$$

The odd arm integral matrices for the derivatives computations are derived as follows

$$\mathbf{D}_\eta = \frac{1}{A}\int_{-b/2}^{b/2} c(y)\eta\frac{\eta}{|\eta|}\mathbf{D}dy = \frac{1}{A}\int_{-b/2}^{b/2} c(y)\left(\eta\frac{\eta}{|\eta|}\mathbf{D}_1 + \mathbf{D}_2\right)dy = \frac{I_\eta}{A}\mathbf{D}_1 + \mathbf{D}_2, \tag{B.14}$$

$$\mathbf{D}_{\eta c2} = \frac{1}{A}\int_{-b/2}^{b/2} c(y)^2\eta\frac{\eta}{|\eta|}\mathbf{D}dy = \frac{1}{A}\int_{-b/2}^{b/2} c(y)^2\left(\eta\frac{\eta}{|\eta|}\mathbf{D}_1 + \mathbf{D}_2\right)dy = \frac{I_{\eta c2}}{A}\mathbf{D}_1 + \frac{I_{c2}}{A}\mathbf{D}_2, \tag{B.15}$$

$$\mathbf{D}_{\eta\eta} = \frac{1}{A}\int_{-b/2}^{b/2} c(y)\eta^2\mathbf{D}dy = \left(\frac{I_{\eta\eta}}{A}\mathbf{D}_1 + \frac{I_\eta}{A}\mathbf{D}_2\right). \tag{B.16}$$

Considering x and z as the collocation points position at $3/4$ chord, the odd arm matrices needed for the estimation of the derivatives with respect to angular rates are

$$\begin{aligned}\mathbf{D}_{\eta,x} &= \frac{1}{A}\int_{-b/2}^{b/2} c(y)\eta\frac{\eta}{|\eta|}x\mathbf{D}dy = \frac{1}{A}\int_{-b/2}^{b/2} c(y)\mathbf{D}\frac{\eta}{|\eta|}\eta\left(tw_x - \frac{y}{R_0}R_0\frac{\eta}{|\eta|}\Gamma - \frac{c(y)}{2}\right)dy \\ &= tw_x\mathbf{D}_\eta - R_0\Lambda\mathbf{D}_{\eta\eta} - \frac{\mathbf{D}_{\eta c2}}{2},\end{aligned} \tag{B.17}$$

$$\begin{aligned}\mathbf{D}_{\eta,z} &= \frac{1}{A}\int_{-b/2}^{b/2} c(y)\eta\frac{\eta}{|\eta|}z\mathbf{D}dy = \frac{1}{A}\int_{-b/2}^{b/2} c(y)\mathbf{D}\frac{\eta}{|\eta|}\eta\left(tw_z + \frac{y}{R_0}R_0\frac{\eta}{|\eta|}\Gamma\right)dy \\ &= tw_z\mathbf{D}_\eta + R_0\Gamma\mathbf{D}_{\eta\eta}.\end{aligned} \tag{B.18}$$

Similarly, $\mathbf{D}_{\eta\eta,x}$ and $\mathbf{D}_{\eta\eta,z}$ can be derived

$$\begin{aligned}\mathbf{D}_{\eta\eta,x} &= \frac{1}{A}\int_{-b/2}^{b/2} c(y)\eta^2x\mathbf{D}dy = \frac{1}{A}\int_{-b/2}^{b/2} c(y)\mathbf{D}\eta^2\left(tw_x - \frac{y}{R_0}R_0\frac{\eta}{|\eta|}\Lambda - \frac{c(y)}{2}\right)dy \\ &= tw_x\mathbf{D}_{\eta\eta} - R_0\Lambda\mathbf{D}_{\eta\eta\eta} - \frac{\mathbf{D}_{\eta\eta c2}}{2},\end{aligned} \tag{B.19}$$

$$\begin{aligned}\mathbf{D}_{\eta\eta,z} &= \frac{1}{A}\int_{-b/2}^{b/2} c(y)\eta^2 z\mathbf{D}dy = \frac{1}{A}\int_{-b/2}^{b/2} c(y)\mathbf{D}\eta^2\left(tw_z + \frac{y}{R_0}R_0\frac{\eta}{|\eta|}\Gamma\right)dy \\ &= tw_z\mathbf{D}_{\eta\eta} + R_0\Gamma\mathbf{D}_{\eta\eta\eta}.\end{aligned} \tag{B.20}$$

B.2 Procedure for the evaluation of derivatives

The derivative of forces and moments with respect to a generic variable $\tilde{y}_j$, using Eq. (6.26), (6.36) and (6.37), can be formalized as follows

$$\begin{aligned}\frac{\partial \boldsymbol{f}}{\partial \tilde{y}_j} &= \frac{1}{Au_0^2}\int_{-b/2}^{b/2} c(y)(\mathbf{P}+\eta\mathbf{D})\left(\frac{\partial \mathbf{C}}{\partial \tilde{y}_j}v_{a,0}^2 + \mathbf{C}_0\frac{\partial v_a^2}{\partial \tilde{y}_j}\right)dy \\ &= \frac{1}{Au_0^2}\int_{-b/2}^{b/2} c(y)(\mathbf{P}+\eta\mathbf{D})\left((\mathbf{C}_\eta - 2\eta\mathbf{C}_{L\alpha})\frac{\partial \gamma_n}{\partial \tilde{y}_j}u_0^2(1+\eta)^2 + \left(\mathbf{C}_{R_0} - \eta\frac{\mathbf{C}_\eta}{\lambda_n}\right)\frac{\partial v_a^2}{\partial \tilde{y}_j}\right)dy,\end{aligned} \tag{B.21}$$

where $\frac{\partial \gamma_n}{\partial \tilde{y}_j}$ and $\frac{\partial v_a^2}{\partial \tilde{y}_j}$ in the latter expression can be found by applying recursively the chain rule.

Equations (6.22) and (6.23) express the apparent velocity squared and the inflow angle for a wing profile. The contributions of the straight wing, dihedral angle and sweep can be analyzed individually as they appear in different terms. Consequently, the derivatives of γ_n and v_a^2 with respect to $\mathcal{U}$, $\mathcal{V}$ and $\mathcal{W}$ for the straight wing can be provided separately, and are given in Table B.1.

	γ_n	v_a^2
$\mathcal{U}$	$-\frac{1}{\lambda_n u_0(1+\eta)^2}$	$2u_0(1+\eta)$
$\mathcal{V}$	0	0
$\mathcal{W}$	$\frac{1}{u_0(1+\eta)}$	$\frac{2u_0}{\lambda_n}$

Table B.1: *Derivatives of γ_n and v_a^2 with respect to $\mathcal{U}$, $\mathcal{V}$ and $\mathcal{W}$ for the straight wing.*

The derivatives of γ_n and v_a^2 with respect to $\mathcal{U}$, $\mathcal{V}$ and $\mathcal{W}$ for the terms depending on sweep and dihedral are instead given in Table B.2.

	γ_n	v_a^2
$\mathcal{U}$	≈ 0	≈ 0
$\mathcal{V}$	$-\Gamma\frac{\eta}{\lvert\eta\rvert}\frac{1}{u_0(1+\eta)} - \Lambda\frac{\eta}{\lvert\eta\rvert}\frac{1}{\lambda_n u_0(1+\eta)^2}$	$-2\Gamma\frac{\eta}{\lvert\eta\rvert}\frac{u_0}{\lambda_n} + 2\Lambda\frac{\eta}{\lvert\eta\rvert}u_0(1+\eta)$
$\mathcal{W}$	≈ 0	≈ 0

Table B.2: *Derivatives of γ_n and v_a^2 with respect to $\mathcal{U}$, $\mathcal{V}$ and $\mathcal{W}$ due to dihedral and sweep angle.*

The chain rule, using the results in Table B.3, can be finally applied to find the analytic expression of the derivatives.

The derivatives of the aerodynamic inflow quantities γ_n or v_a^2, which we will indicate

	$\mathcal{U}$	$\mathcal{V}$	$\mathcal{W}$
u	1	0	0
v	0	1	0
w	0	0	1
p	0	$-z$	y
q	z	0	$-x$
r	$-y$	x	0
ϕ	0	$\frac{u_0}{\lambda_n}$	0
θ	$-\frac{u_0}{\lambda_n}$	0	0
ψ	0	0	0

Table B.3: *Derivatives of $\mathcal{U}, \mathcal{V}, \mathcal{W}$ (Eq.* (6.14)*) with respect to dimensional state variables.*

as $q_{a,j}$, with respect to $\tilde{p}$ can be written as

$$\frac{\partial q_{a,j}}{\partial \tilde{p}} = \frac{\partial q_{a,j}}{\partial \left(p\frac{b}{2u_0}\right)} = \frac{2u_0}{b}\left(\frac{\partial q_{a,j}}{\partial \mathcal{W}}\frac{\partial \mathcal{W}}{\partial p} + \frac{\partial q_{a,j}}{\partial \mathcal{V}}\frac{\partial \mathcal{V}}{\partial p}\right) = \frac{2u}{b}\left(y\frac{\partial q_{a,j}}{\partial \mathcal{W}} - z\frac{\partial q_{a,j}}{\partial \mathcal{V}}\right) = \frac{2y}{b}\frac{\partial q_{a,j}}{\partial \tilde{w}} - \frac{2z}{b}\frac{\partial q_{a,j}}{\partial \tilde{v}}. \tag{B.22}$$

The derivatives with respect to $\tilde{q}$ can be written as

$$\frac{\partial q_{a,j}}{\partial \tilde{q}} = \frac{\partial q_{a,j}}{\partial \left(q\frac{c}{2u_0}\right)} = \frac{2u_0}{c}\left(\frac{\partial q_{a,j}}{\partial \mathcal{U}}\frac{\partial \mathcal{U}}{\partial q} + \frac{\partial q_{a,j}}{\partial \mathcal{W}}\frac{\partial \mathcal{W}}{\partial q}\right) = \frac{2z}{c}\frac{\partial q_{a,j}}{\partial \tilde{u}} - \frac{2x}{c}\frac{\partial q_{a,j}}{\partial \tilde{w}}. \tag{B.23}$$

The derivatives with respect to $\tilde{r}$ can be written as

$$\frac{\partial q_{a,j}}{\partial \tilde{r}} = \frac{\partial q_{a,j}}{\partial \left(r\frac{b}{2u_0}\right)} = \frac{2u_0}{b}\left(\frac{\partial q_{a,j}}{\partial \mathcal{U}}\frac{\partial \mathcal{U}}{\partial r} + \frac{\partial q_{a,j}}{\partial \mathcal{V}}\frac{\partial \mathcal{V}}{\partial r}\right) = -\frac{2y}{b}\frac{\partial q_{a,j}}{\partial \tilde{u}} + \frac{2x}{b}\frac{\partial q_{a,j}}{\partial \tilde{v}}. \tag{B.24}$$

The derivative with respect to the roll angle ϕ is

$$\frac{\partial q_{a,j}}{\partial \phi} = \frac{\partial q_{a,j}}{\partial \mathcal{V}}\frac{\partial \mathcal{V}}{\partial \phi} = \frac{1}{\lambda_n}\frac{\partial q_{a,j}}{\partial \tilde{v}} = \frac{1}{\lambda_n}\frac{\partial q_{a,j}}{\partial \tilde{v}}, \tag{B.25}$$

The derivative with respect to the pitch angle θ

$$\frac{\partial q_{a,j}}{\partial \theta} = \frac{\partial q_{a,j}}{\partial \mathcal{U}}\frac{\partial \mathcal{U}}{\partial \theta} = -\frac{1}{\lambda_n}\frac{\partial q_{a,j}}{\partial \tilde{u}}. \tag{B.26}$$

The derivative with respect to the yaw angle ψ of the aerodynamic force generated by the main wing is always null.

B.3 Straight wing derivatives

Table 6.1 summarizes all the non-null derivatives for the case of a straight wing.

B.3.1 Derivatives with respect to $\tilde{u}$

To find the derivative of the aerodynamic force with respect to the non-dimensional longitudinal velocity $\frac{\partial \boldsymbol{f}}{\partial \tilde{u}}$, the two terms, necessary for the evaluating the derivatives

(Eq. (B.21)), are

$$\frac{\partial \mathbf{C}}{\partial \tilde{u}} v_{a,0}^2 = (\mathbf{C}_\eta - 2\eta \mathbf{C}_{L\alpha}) \left(-\frac{1}{\lambda_n u_0 (1+\eta)^2} \right) \left(u_0^2 (1+\eta)^2 \right) u_0 = \left(-\frac{\mathbf{C}_\eta}{\lambda_n} + 2\eta \frac{\mathbf{C}_{L\alpha}}{\lambda_n} \right) u_0^2,$$
$$\mathbf{C}_0 \frac{\partial v_a^2}{\partial \tilde{u}} = \left(\mathbf{C}_{R_0} - \eta \frac{\mathbf{C}_\eta}{\lambda_n} \right) (2u_0(1+\eta)) u_0 = 2 \left(\mathbf{C}_{R_0} + \eta \mathbf{C}_{R_0} - \eta \frac{\mathbf{C}_\eta}{\lambda_n} \right) u_0^2, \tag{B.27}$$

where $\frac{\partial \gamma_n}{\partial \mathcal{U}}$ and $\frac{\partial v_a^2}{\partial \mathcal{U}}$ are found in Table B.1 and $\frac{\partial \mathcal{U}}{\partial \tilde{u}} = 1$ is given in Table B.3.

Performing an integral along the wingspan in order to find the aerodynamic derivative with respect to $\tilde{u}$, Eq. (B.21), considering Eq. (B.27), takes the form

$$\begin{aligned} \frac{\partial \boldsymbol{f}}{\partial \tilde{u}} &= \frac{1}{A} \int_{-b/2}^{b/2} c(y)(\mathbf{P} + \eta \mathbf{D}) \Big[-\frac{\mathbf{C}_\eta}{\lambda_n} + 2\eta \frac{\mathbf{C}_{L\alpha}}{\lambda_n} + 2\mathbf{C}_{R_0} + 2\eta \left(\mathbf{C}_{R_0} - \frac{\mathbf{C}_\eta}{\lambda_n} \right) \Big] dy \\ &= \mathbf{P}_A \left(2\mathbf{C}_{R_0} - \frac{\mathbf{C}_\eta}{\lambda_n} \right) + 2\mathbf{D}_{\eta\eta} \left(\mathbf{C}_{R_0} - \frac{\mathbf{C}_\eta}{\lambda_n} + \frac{\mathbf{C}_{L\alpha}}{\lambda_n} \right). \end{aligned} \tag{B.28}$$

B.3.2 Derivatives with respect to $\tilde{w}$

We follow here the same procedure as in Sect. B.3.1 to find the derivative with respect to $\tilde{w}$.

$$\frac{\partial \mathbf{C}}{\partial \tilde{w}} v_{a,0}^2 = (\mathbf{C}_\eta - 2\eta \mathbf{C}_{L\alpha}) \left(\frac{1}{u_0 (1+\eta)} \right) \left(u_0^2 (1+\eta)^2 \right) u_0 \approx (\mathbf{C}_\eta + \eta(\mathbf{C}_\eta - 2\mathbf{C}_{L\alpha})) u_0^2,$$
$$\mathbf{C}_0 \frac{\partial v_a^2}{\partial \tilde{w}} = \mathbf{C}_0 \left(2\frac{u_0}{\lambda_n} \right) \approx \left(2\frac{\mathbf{C}_{R_0}}{\lambda_n} - 2\eta \frac{\mathbf{C}_\eta}{\lambda_n^2} \right) u_0^2. \tag{B.29}$$

$$\frac{\partial \boldsymbol{f}}{\partial \tilde{w}} = \frac{1}{A} \int_{-b/2}^{b/2} c(y)(\mathbf{P} + \eta \mathbf{D}) \Big[\mathbf{C}_\eta + \eta(\mathbf{C}_\eta - 2\mathbf{C}_{L\alpha}) + 2\frac{\mathbf{C}_{R_0}}{\lambda_n} - 2\eta \frac{\mathbf{C}_\eta}{\lambda_n^2} \Big] dy. \tag{B.30}$$

B.3.3 Derivatives with respect to $\tilde{p}$

Making use of the partial derivatives in Sect. B.3.1, the derivative with respect to $\tilde{p}$ is

$$\frac{\partial \boldsymbol{f}}{\partial \tilde{p}} = \frac{1}{A} \frac{2R_0}{b} \int_{-b/2}^{b/2} c(y)\eta(\mathbf{P} + \eta \mathbf{D}) \Big[\mathbf{C}_\eta + \eta \mathbf{C}_\eta - 2\eta \mathbf{C}_{L\alpha} + 2\frac{\mathbf{C}_{R_0}}{\lambda_n} - 2\eta \frac{\mathbf{C}_\eta}{\lambda_n^2} \Big] dy. \tag{B.31}$$

B.3.4 Derivatives with respect to $\tilde{q}$

Making use of the partial derivatives in Sect. B.3.1, the derivative with respect to $\tilde{q}$ is

$$\begin{aligned} \frac{\partial \boldsymbol{f}}{\partial \tilde{q}} = &\frac{1}{A} \int_{-b/2}^{b/2} c(y)(\mathbf{P} + \eta \mathbf{D}) \frac{2z}{c} \Big[-\frac{\mathbf{C}_\eta}{\lambda_n} + 2\eta \frac{\mathbf{C}_{L\alpha}}{\lambda_n} + 2\mathbf{C}_{R_0} + 2\eta \left(\mathbf{C}_{R_0} - \frac{\mathbf{C}_\eta}{\lambda_n} \right) \Big] dy \\ &- \frac{1}{A} \int_{-b/2}^{b/2} c(y)(\mathbf{P} + \eta \mathbf{D}) \frac{2x}{c} \Big[\mathbf{C}_\eta + \eta(\mathbf{C}_\eta - 2\mathbf{C}_{L\alpha}) + 2\frac{\mathbf{C}_{R_0}}{\lambda_n} - 2\eta \frac{\mathbf{C}_\eta}{\lambda_n^2} \Big] dy. \end{aligned} \tag{B.32}$$

B.3.5 Derivatives with respect to $\tilde{r}$

Making use of the partial derivatives in Sect. B.3.1, the derivative with respect to $\tilde{r}$ is

$$\frac{\partial \boldsymbol{f}}{\partial \tilde{r}} = -\frac{1}{A}\frac{2R_0}{b}\int_{-b/2}^{b/2} c(y)\eta(\mathbf{P}+\eta\mathbf{D})\Big[-\frac{\mathbf{C}_\eta}{\lambda_n}+2\eta\frac{\mathbf{C}_{L\alpha}}{\lambda_n}+2\mathbf{C}_{R_0}+2\eta\mathbf{C}_{R_0}-2\eta\frac{\mathbf{C}_\eta}{\lambda_n}\Big]dy. \tag{B.33}$$

B.3.6 Derivatives with respect to θ

Making use of the partial derivatives in Sect. B.3.1, the derivative with respect to θ is

$$\frac{\partial \boldsymbol{f}}{\partial \theta} = \frac{1}{A}\int_{-b/2}^{b/2} c(y)(\mathbf{P}+\eta\mathbf{D})\left(\mathbf{C}_\eta+2\eta\left(\mathbf{C}_\eta-\mathbf{C}_{L\alpha}\right)\right)dy. \tag{B.34}$$

B.4 Derivatives due to dihedral and sweep angles

Table 6.2 summarizes the non-null derivatives due to dihedral and sweep.

Derivatives due to dihedral

To find the derivative of the aerodynamic force with respect to the non-dimensional lateral velocity $\frac{\partial \boldsymbol{f}}{\partial \tilde{v}}$ due to the dihedral angle, the two terms, necessary for the evaluating the derivatives (Eq. (B.21)), are

$$\begin{aligned}\frac{\partial \mathbf{C}}{\partial \tilde{v}}v_{a,0}^2 &= \left(\mathbf{C}_\eta-2\eta\mathbf{C}_{L\alpha}\right)\left(-\Gamma\frac{\eta}{|\eta|}\frac{1}{u_0(1+\eta)}\right)\left(u_0^2(1+\eta)^2\right)u_0\\ &= -\Gamma\frac{\eta}{|\eta|}\left(\mathbf{C}_\eta+\eta\mathbf{C}_\eta-2\eta\mathbf{C}_{L\alpha}\right)u_0^2,\\ \mathbf{C}_0\frac{\partial v_a^2}{\partial \tilde{v}} &= -\Gamma\frac{\eta}{|\eta|}\left(2\frac{\mathbf{C}_{R_0}}{\lambda_n}-2\eta\frac{\mathbf{C}_\eta}{\lambda_n^2}\right)u_0^2.\end{aligned} \tag{B.35}$$

where $\frac{\partial \gamma_n}{\partial \mathcal{V}}$ and $\frac{\partial v_a^2}{\partial \mathcal{V}}$ are found in Table B.2 and $\frac{\partial \mathcal{V}}{\partial \tilde{v}}=1$ is given in Table B.3.

Performing an integral along the wingspan in order to find the aerodynamic derivative with respect to $\tilde{v}$, Eq. (B.21) takes the form

$$\begin{aligned}\frac{\partial \boldsymbol{f}}{\partial \tilde{v}} &= -\frac{1}{A}\Gamma\int_{-b/2}^{b/2} c(y)\frac{\eta}{|\eta|}\left(\mathbf{P}+\eta\mathbf{D}\right)\left(\mathbf{C}_\eta+\eta\mathbf{C}_\eta-2\eta\mathbf{C}_{L\alpha}+2\frac{\mathbf{C}_{R_0}}{\lambda_n}-2\eta\frac{\mathbf{C}_\eta}{\lambda_n^2}\right)dy\\ &= -\Gamma\left[\mathbf{P}_\eta\left(\mathbf{C}_\eta-2\mathbf{C}_{L\alpha}\right)+\mathbf{D}_\eta\left(\mathbf{C}_\eta+2\frac{\mathbf{C}_{R_0}}{\lambda_n}\right)\right].\end{aligned} \tag{B.36}$$

Derivatives due to sweep

To find the derivative of the aerodynamic force with respect to the non-dimensional lateral velocity $\frac{\partial \boldsymbol{f}}{\partial \tilde{v}}$ due to the sweep angle, the two terms, necessary for the evaluating

the derivatives (Eq. (B.21)), are

$$\begin{aligned}\frac{\partial \mathbf{C}}{\partial \tilde{v}} v_{a,0}^2 &= (\mathbf{C}_\eta - 2\eta \mathbf{C}_{L\alpha}) \left(-\Lambda \frac{\eta}{|\eta|} \frac{1}{\lambda_n u_0 (1+\eta)^2} \right) \left(u_0^2 (1+\eta)^2 \right) u_0 \\ &= -\Lambda \frac{\eta}{|\eta|} \left(\frac{\mathbf{C}_\eta}{\lambda_n} - 2\eta \frac{\mathbf{C}_{L\alpha}}{\lambda_n} \right) u_0^2, \\ \mathbf{C}_0 \frac{\partial v_a^2}{\partial \tilde{v}} &= \mathbf{C}_0 \left(2\Lambda \frac{\eta}{|\eta|} u_0 (1+\eta) \right) u_0 = 2\Lambda \frac{\eta}{|\eta|} \left(\mathbf{C}_{R_0} + \eta \left(\mathbf{C}_{R_0} - \frac{\mathbf{C}_\eta}{\lambda_n} \right) \right) u_0^2. \end{aligned} \tag{B.37}$$

where $\frac{\partial \gamma_n}{\partial \mathcal{V}}$ and $\frac{\partial v_a^2}{\partial \mathcal{V}}$ are found in Table B.2 and $\frac{\partial \mathcal{V}}{\partial \tilde{v}} = 1$ is given in Table B.3.

Performing an integral along the wingspan in order to find the aerodynamic derivative with respect to $\tilde{v}$, Eq. (B.21) takes the form

$$\begin{aligned}\frac{\partial \boldsymbol{f}}{\partial \tilde{v}} &= \frac{1}{A} \Lambda \int_{-b/2}^{b/2} c(y) \frac{\eta}{|\eta|} (\mathbf{P} + \eta \mathbf{D}) \left(-\frac{\mathbf{C}_\eta}{\lambda_n} + 2\eta \frac{\mathbf{C}_{L\alpha}}{\lambda_n} + 2\mathbf{C}_{R_0} + 2\eta \left(\mathbf{C}_{R_0} - \frac{\mathbf{C}_\eta}{\lambda_n} \right) \right) dy \\ &= \Lambda \left[2\mathbf{P}_\eta \left(\mathbf{C}_{R_0} - \frac{\mathbf{C}_\eta}{\lambda_n} + \frac{\mathbf{C}_{L\alpha}}{\lambda_n} \right) + \mathbf{D}_\eta \left(2\mathbf{C}_{R_0} - \frac{\mathbf{C}_\eta}{\lambda_n} \right) \right] \end{aligned} \tag{B.38}$$

APPENDIX C

Inertia estimation

C.1 Lifting body structural design

All the lifting surfaces (main wing, horizontal and vertical tail) are assumed to be designed with the procedure presented here.

A generic elliptic lift distribution is

$$l(\eta) = \frac{4}{\pi}\frac{\overline{L}}{b}\sqrt{1-\eta^2} \tag{C.1}$$

where $\overline{L} = \frac{1}{2}\rho\frac{b^2}{\mathcal{AR}}C_L\overline{u}^2$ and $\eta = \frac{y}{b/2}$. C_L is taken as the design lift coefficient and $\overline{u}$ is a fixed value.

The aerodynamic bending moment at a generic wing section $\eta > 0$ is

$$M = \frac{b^2}{4}\int_{\eta}^{1}(\eta^* - \eta)l(\eta^*)\,d\eta^* = \frac{\overline{L}b}{\pi}\left[\frac{\eta}{4}(2\arcsin\eta - \pi) + \frac{(\eta^2+2)\sqrt{(1-\eta^2)}}{6}\right] \tag{C.2}$$

The wing mass is assumed to be proportional to the spar caps mass, which are designed according to the aerodynamic bending moment M. The sparcaps flap-wise distance w_f is assumed proportional to the airfoil thickness and consequently to the chord

$$w_f(\eta) = f_{wf}c(\eta) = f_{wf}\frac{4}{\pi}b\mathcal{AR}\sqrt{1-\eta^2}, \tag{C.3}$$

where an elliptic planform is assumed. The sparcap thickness t_{sc} is to be designed. The sparcap area $w_e t_{sc}$, with w_e being the sparcaps edge-wise width is assumed to be concentrated at $\frac{w_f}{2}$. The section inertia I can be approximated with

$$I \approx \frac{1}{2}w_e t_{sc} w_f^2. \tag{C.4}$$

Being the stress in the sparcap equal to $\sigma = \frac{M\frac{w_f}{2}}{I}$, the section thickness can be designed based on a given material strength $\overline{\sigma}$

$$t_{sc}(\eta) = \frac{M(\eta)}{\overline{\sigma} w_e(\eta) w_f(\eta)}. \tag{C.5}$$

The wing mass is the integral of the sparcaps liner density $2\overline{\rho} w_e t_{sc}$ over the span

$$m \approx 2\int_0^{b/2} 2\overline{\rho} w_e t_{sc} dy \approx b\int_0^1 2\overline{\rho} w_e t_{sc} d\eta = 2b\frac{\overline{\rho}}{\overline{\sigma}}\int_0^1 \frac{M(\eta)}{w_f(\eta)} d\eta \tag{C.6}$$

where $\overline{\rho}$ is the material density.

The total mass of the lifting body m_{lb} can then be written as

$$m_{lb} \approx 2b\frac{\overline{\rho}}{\overline{\sigma}}\frac{\overline{L}b}{\pi}\frac{\pi}{f_{wf} 4b\mathcal{AR}} \underbrace{\int_0^1 \frac{\eta(2\arcsin\eta - \pi)}{4\sqrt{1-\eta^2}} + \frac{\eta^2+2}{6} d\eta}_{\int_0^1 s_m(\eta)d\eta \approx 0.1} = 0.1\rho \underbrace{\frac{\overline{\rho}}{\overline{\sigma}}\frac{\overline{u}^2}{4f_{wf}}}_{f_m} \frac{C_L}{\mathcal{AR}^2} b^3, \tag{C.7}$$

where f_m is a constant value dependent of the design methodology.

C.2 Windplane mass and inertia

The non dimensional mass parameter μ is an input to the model and can be expressed as function of a structural design constant f_m and geometrical and aerodynamic characteristics of the wing, horizontal and vertical stabilizer.

$$\mu = \frac{m}{\rho b^3} \approx 0.1 f_m \left(\frac{C_L}{\mathcal{AR}^2} + \frac{b_h^3}{b^3}\frac{\tilde{C}_{L,h}}{\mathcal{AR}_h^2} + \frac{b_v^3}{b^3}\frac{\tilde{C}_{L,v}}{\mathcal{AR}_v^2} \right), \tag{C.8}$$

where in this thesis, to estimate the inertia, it is assumed $C_L = C_{L,h} = C_{L,v} = 1$. Since μ and the quantities inside the bracket are inputs to the model, the factor f_m can be found and used to find the center of mass and the moments of inertia.

The moment of inertia of the main wing with respect to an axis perpendicular to the wing axis ($\boldsymbol{e}_{1,b}$ and $\boldsymbol{e}_{3,b}$) is

$$I_{\perp,w} \approx \rho f_m \frac{C_L}{\mathcal{AR}^2}\frac{b^5}{4} \underbrace{\int_0^1 \eta^2 s_m(\eta) d\eta}_{\approx 0.01} \approx 0.025 m b^2 \tag{C.9}$$

Modeling the horizontal and vertical stabilizer as concentrated masses in the same location (ts) and in the symmetry plane of the plane ($ts_2 = 0$), the windplane moments of inertia are

$$\begin{aligned} I_{xx} &= I_{\perp,w} \\ I_{yy} &= t w_1^2 m_w + t s_1^2 (m_h + m_v) \\ I_{zz} &= t w_1^2 m_w + t s_1^2 (m_h + m_v) + I_{\perp,w}. \end{aligned} \tag{C.10}$$